AN ABSTRACT OF THE THESIS OF

Ravindranath T. Kollipara for the degree of Doctor of Philosophy in Electrical and Computer Engineering presented on April 12, 1991. Title: Modeling and Testing of Semi-Insulating Gallium Arsenide Interdigitated Photodetectors.

Abstract approved: Redacted for Privacy

Thomas K. Plant

High speed photodetectors are a necessary element in broad band digital and analog optical communication systems. In this thesis easily integrable planar high speed photodetectors made on undoped semi-insulating (SI) GaAs substrates are modeled and tested. The fabrication process of the detectors is fully compatible with GaAs metal-semiconductor field effect transistor (MESFET) processing technology. Interdigitated fingers are used as the contacts to achieve both high sensitivity and large bandwidth. Detectors made with both ohmic and Schottky contacts are fabricated and tested.

The equivalent circuit elements of the interdigitated structure are modeled using accurate lumped element circuit models associated with the various discontinuities of the structure. The results of the model agree well with the experimental results as well as with other published results. Numerical simulation of the SI-GaAs metal-semiconductor-metal (MSM) photodetector is performed. The carriers are tracked after an ideal optical pulse is applied and the intrinsic current as a function of time is computed. Then the influence of all the external circuit elements is included and the output current across the load resistor is

computed. The simulated response is compared with other published models.

The electrical and optical characteristics of the detectors are measured. For ohmic contact detectors, the dark current increases linearly with bias until some critical field is reached beyond which the dark current increases nonlinearly with bias. The time response of the detectors is measured with a 10 ps pulsed laser operating at ~ 600 nm and also with a pulsed GaAs/AlGaAs semiconductor laser operating at 850 nm. The ohmic and Schottky contact detectors have approximately the same rise time. The fall time of the Schottky contact detector is much smaller than the fall time of ohmic contact detector. The long fall time of the ohmic detector does not depend on the spacing between contacts. This long fall time is due to the large barrier that exists near the ohmic metal/SI-GaAs cathode contact. No such barrier exists for SI-GaAs MSM photodetector. The simulated impulse response of the SI-GaAs MSM photodetector is compared with the measured impulse response.

Modeling and Testing of Semi-Insulating Gallium Arsenide Interdigitated Photodetectors

by

Ravindranath Tagore Kollipara

A THESIS

submitted to

Oregon State University

in partial fulfillment of
the requirements for the
degree of

Doctor of Philosophy

Completed: April 12, 1991

Commencement: June 1991

APPROVED:

Redacted for Privacy

Associate Professor of Electrical and Computer Engineering
in charge of major

Redacted for Privacy

Head of the Electrical and Computer Engineering Department

Redacted for Privacy

Dean of Graduate School

Date thesis is presented April 12, 1991

Presented by Ravindranath Tagore Kollipara

ACKNOWLEDGEMENTS

The author wishes to express his appreciation to Dr. Thomas K. Plant, his major professor, for his encouragement, guidance and support during the course of this research.

The author expresses his special thanks to Prof. Vijai K. Tripathi for his encouragement and guidance during his coursework and the preparation of this research. The author wants to extend his thanks to Professors John W. Wager, John R. Arthur, Joseph Nibler and Dwight Bushnell for serving on his graduate committee and reviewing the manuscript.

The author also expresses his thanks to his colleagues Hosung Chang, Hyung Mo Yoo, John T. Ebner, Seungbae Kim, Yong Thye and Leon Ungier for their helpful discussions and interest in the development of this research.

The author is deeply grateful to his wife, Sumathi and sons, Deep and Naveen, for their love, patience and understanding during the course of this work.

Finally, the author wishes to thank his mother for her encouragement, courage, dedication and inspiration throughout his life.

TABLE OF CONTENTS

LIST OF FIGURES

LIST OF TABLES

MODELING AND TESTING OF SEMI-INSULATING GALLIUM ARSENIDE INTERDIGITATED PHOTODETECTORS

1. INTRODUCTION

The high speed and large dynamic range of pho todetectors have resulted in a number of novel applications in electronics and optoelectronics. These include [1] optical detection, characterization of high speed optical components such as modulators, lasers, and multiplexers, transmission of microwave signals via optical fibers, electronic gating and switching, etc..

Until the mid 1970's, most of the high speed semiconductor photodetectors were made of silicon (Si) and germanium (Ge) p-i-n and avalanche photodiodes (APDs). Si is primarily used for wavelengths below 1 μm and Ge is used in the wavelength range of 1.0 to 1.6 μm. Since the mid 1970's, interest has grown in photodetectors made of GaAs (GaAs, AlGaAs) and InP (InP, InGaAs, InGaAsP) compounds. These III-V compounds have a direct bandgap and therefore higher absorption coefficients than the indirect bandgap materials Si or Ge. This makes the light absorption layer shorter for III-V compounds than for Si or Ge to achieve the same quantum efficiency. III-V compounds also have higher mobilities and higher peak drift velocities. III-V detectors could be integrated with GaAs or InP integrated circuits and the integrated receiver would perform better because GaAs metal-semiconductor field effect transistors (MESFETs) and InP metal-insulator-semiconductor field effect transistors (MISFETs) have superior performance over Si metal-oxide-semiconductor field effect transistors (MOSFETs). Since GaAs

is also an electro-optic material, modulators, switches and amplifiers could be integrated on the same chip. GaAs has a higher bandgap than Si which results in smaller leakage current since the dark current is exponentially dependent on the energy bandgap. Finally, the smaller junction capacitance in GaAs due to the larger depletion width makes higher bandwidths possible.

1.1 Motivation

GaAs material is excellent for high speed analog and digital integrated circuits, monolithic microwave integrated circuits (MMIC) and optoelectronic integrated circuits (OEICs). High speed photodetectors made of GaAs material are used in many applications that include high speed sampling and instrumentation.

Until the early 1980's the p-i-n photodiode and the APD were the work horses of the GaAs photodetector applications. However, p-i-n and APD structures are not planar and the processing steps are not readily compatible with the standard MESFET processing technology. GaAs p-i-n and APD detectors also require large biasing voltages. Since the early 1980's, interest has grown in developing easily integrable, planar photodetectors capable of operating at low biasing voltages.

The choice of a photoconductive material for a fast photodetector requires a material with a short photoconductive lifetime [2]. A short lifetime, however, means a lower conductivity when illuminated, which in turn results in low responsivity unless the material has a high mobility. Good detectivity on the other hand requires a high dark resistance. So a photoconductive material should have a high dark resistance, high mobility and short lifetime.

Undoped SI-GaAs has all of these properties. Gain is possible in photoconductors at the expense of bandwidth and the gain is relatively insensitive to temperature variation because neither carrier lifetime nor transit time is a strong function of temperature [3]. This is in contrast to APDs where avalanche gains are highly temperature sensitive. Because of all these reasons the photoconductor has become a viable option [4].

The candidates for easily integrable planar detectors are photoconductors, back-to-back Schottky barriers and p-i-n structures which are all used in planar configuration. The capacitance of an APD or a vertical p-i-n structure is higher than that of a photoconductor. An interdigitated structure (IDS) has an enhanced sensitivity with a time response similar to a simple gap of the same active area [5]. In the simple gap case even though capacitance is small, transit time is large and so the bandwidth is small. In an IDS capacitance and transit time could be adjusted such that bandwidth is optimized. For large area devices, vertical p-i-n and APD detectors are not suitable whereas a photoconductor, back-to-back Schottky barrier or lateral p-i-n in IDS configuration would be ideal.

The objective of this work is to study, through modeling and testing, the time response of planar detectors made on undoped SI-GaAs. Detectors are made directly on SI-GaAs substrates instead of implanted epi-layers. (The absorption length for GaAs material at 0.8 μm is ~ 1 μm where as the Si-implant depth in GaAs is only ~ 0.3 μm, so the sensitivity of the detectors made on SI-GaAs is greater than those made on Si-implanted layers). Interdigitated detectors with n-ohmic and Schottky contacts are studied. The fabrication process and the contact metals used are

fully compatible with MESFET processing technology. The lateral p-i-n is excluded from this study because present commercial GaAs MESFET technology does not include a p-implant or a p-ohmic step.

1.2 Synopsis of chapters

In chapter 2, the theory of photodetectors and some of the previous work on GaAs photodetectors is reviewed with emphasis on planar integrable photodetectors. The characteristic parameters describing a photodetector are defined and expressions for gain and bandwidth are given. Some common transitions taking place in photodetectors are described. Distinction is made between primary and secondary photocurrents and between intrinsic and extrinsic photocurrents. The influence of contacts and traps on the photodetection process is discussed. Various types of photodetectors are described briefly.

In chapter 3, the circuit modeling work on the interdigitated structure (IDS) is presented. The parasitics associated with the IDS are modeled using accurate lumped element circuit models associated with the various discontinuities of the IDS. The model results are compared with experiment as well as other published results in the literature. The capacitance of the IDS is analyzed with and without a ground plane.

In chapter 4, the impulse response simulation of the SI-GaAs MSM photodetector is presented. The differential equations are descretized using the finite difference method and Gummel's algorithm is used to solve the resulting algebraic equations. The bulk carrier transport equations and material parameters are given. The model considers full bipolar transport, effects of field dependent mobilities,

carrier diffusion and recombination. Dynamic simulation is carried out after applying an ideal optical impulse. The output current is plotted with and without the influence of the external circuit.

In chapter 5, experimental results are presented and discussed. Both ohmic and Schottky contact photodetectors are fabricated on undoped SI-GaAs. The processing steps and contact metals used are all compatible with commercial MESFET processing technology. Results from I-V and pulse measurements are presented. The experimental results are compared with expected results.

In chapter 6 the work performed is summarized and conclusions are given. Suggestions for future work are made.

2. THEORY AND BACKGROUND

In this chapter different types of photodetectors are described in brief. Some parameters which are common to all photodetectors are defined. The literature on monolithically integrable photodetectors is reviewed.

2.1 Parameters common to all photodetectors

The one characteristic that is common to all photodetectors is that they are all square law detectors. The detector output is proportional to the square of the optical electric field. Some common parameters of all photodetectors are described below.

Responsivity, R_λ(A/W or V/W), is the amount of electrical signal per unit of optical power. R_λ is a function of optical signal wavelength, λ. R_λ might vary with detector bias and load resistance also.

Spectral coverage specifies over what wavelength range the detector will operate and at what responsivity.

Quantum efficiency specifies the efficiency of converting photons to electrical carriers and is defined as the number of electron-hole pairs (EHPs) or electrons or holes generated for each incident photon.

Noise equivalent power (NEP) and specific detectivity (D^*) specify the noise properties of the total detection system. NEP is the optical power that must be incident on the detector so that the signal is equal to the noise for a given wavelength, detector temperature and bandwidth. D^* is

the inverse of the NEP normalized to the square root of the detector area and the system bandwidth.

$$D^* = \sqrt{\text{Area}*\text{Bandwidth}}/\text{NEP}, \quad \text{cm}\sqrt{\text{Hz}}/\text{W}. \tag{2.1}$$

Response time is the rise time (t_r) or fall time (t_f) or full width at half maximum (FWHM) for a pulse input and is related to the bandwidth (BW) of the detector. The bandwidth of a photodetector is limited by both the RC time constant and transit time (t_t) effects. The RC limited fall time is

$$t_f(\text{RC limited}) = 2.2RC \tag{2.2}$$

and the RC limited 3-dB bandwidth (the frequency range over which the detector output power is $\geq$ 50% of the peak power) is

$$BW(\text{RC limited}) = 1/(2\pi RC) = 0.35/t_f(\text{RC limited}). \tag{2.3}$$

The transit time limited 3-dB bandwidth is given by [6]

$$BW(t_t \text{ limited}) = 0.38/t_t. \tag{2.4}$$

This expression is valid only if carriers are not trapped and if $t_t \leq$ the minority carrier lifetime. The overall bandwidth of a photodetector due to both RC and transit time effects is

$$[BW]^{-1} = [BW(\text{RC limited})]^{-1} + [BW(t_t \text{ limited})]^{-1} \tag{2.5}$$

$$[BW]^{-1} = t_f(\text{RC limited})/0.35 + t_t/0.38 \tag{2.6}$$

$$BW \approx 0.35/[t_f(\text{RC limited}) + t_t]. \tag{2.7}$$

If the ratio of t_f and t_t is much different from one then the bandwidth is dominated by the larger of the two.

Linearity and saturation: The linear range specifies the optical power range in which the detector output is proportional to the input power. The saturation region specifies the optical power range in which the detector output is no longer proportional to the input optical power.

Gain (Γ) is defined as the number of carriers collected for each electron or hole or EHP generated due to an absorbed photon. If light falling on a photodetector creates G_c EHPs per second per unit volume, then the net increases in free electron and hole densities as a result of absorption of light are

$$\Delta n = G_c \tau_n \tag{2.8}$$

$$\Delta p = G_c \tau_p \tag{2.9}$$

where τ_n (τ_p) is the free lifetime of the electron (hole). The free lifetime is defined as [7] the time the charge carrier is free to contribute to the conductivity. It is the time that an excited electron (hole) spends in the conduction (valence) band. It can be (a) terminated by recombination, or if the carrier is extracted from the crystal by the electric field without being replenished from the opposite electrode; (b) interrupted if the carrier is trapped, to be resumed when the carrier is freed from the trap; (c) undisturbed if the carrier is extracted from the crystal by the field and at the same time an identical carrier is injected into the crystal from the opposite electrode.

The increase in current due to Δn and Δp is

$$\Delta I = qG_c(\tau_n \mu_n + \tau_p \mu_p) EA \tag{2.9}$$

where μ_n (μ_p) is the mobility of the electron (hole), E is the electric field, q is the charge of an electron and A is the area of the detector. If G_T is the total number of EHPs generated per second (if G_c is uniform then $G_T = G_c$.volume) then the gain of the photodetector for a uniform generation rate is

$$\Gamma = \Delta I/qG_T = (\tau_n\mu_n + \tau_p\mu_p)E/L \tag{2.10}$$

where L is the length of the detector. If the photodetector is operated in the linear region of the drift velocity-field curve then

$$v_n = \mu_n E \tag{2.11}$$

$$v_p = \mu_p E \tag{2.12}$$

where v_n (v_p) is the drift velocity of the electron (hole). The electron and hole transit times are given by

$$t_{tn} = L/v_n \tag{2.13}$$

$$t_{tp} = L/v_p. \tag{2.14}$$

The gain can be expressed in terms of the transit times as

$$\Gamma = (\tau_n v_n + \tau_p v_p)/L = \tau_n/t_{tn} + \tau_p/t_{tp}. \tag{2.15}$$

If the photodetector is operated in the saturation region of the drift velocity-field curve, then v_n and v_p are replaced in equations (2.13)-(2.15) by v_{nsat} and v_{psat}. The expression for gain given by equation (2.10) or (2.15) applies to any photodetector that has no avalanche gain. The lifetime of photoexcited carriers is a key parameter for photodetectors.

Gain-Bandwidth Product (GBP) is the product of the gain and the bandwidth of the detector.

2.2 Different types of photodetectors

In this section photoconductor, photodiode, Schottky photodiode and phototransistor type solid state photodetectors are described. The electronic transitions that might be taking place when light is incident on a semiconductor material are shown schematically in the energy-band diagram of Fig. 2.1 [7]. These transitions can be devided into three groups: (1) absorption and (Fig. 2.1 (a)); (2) trapping and capture (Fig. 2.1(b)); and (3) recombination (Fig. 2.1(c)).

The three types of absorption transitions that produce free carriers resulting in increased conductivity of the semiconductor material are shown in Fig. 2.1(a). Transition 1 corresponds to absorption by the atoms of the crystal, producing a free electron and a free hole for each photon absorbed. These transitions contribute to intrinsic photoconductivity. Transition 2 corresponds to absorption at localized (donor-like) defects in the crystal, producing a free electron and a hole bound in the neighborhood of the defect for each photon absorbed. Transition 3 corresponds to absorption again at localized (acceptor-like) defects in the crystal, raising an electron from the valence band to an unoccupied defect level, producing a free hole and an electron bound in the neighborhood of the defect for each photon absorbed. Transitions 2 and 3 contribute to extrinsic photoconductivity. The GaAs detectors characterized in this thesis involve only intrinsic transitions.

The electrons and holes freed by the absorption of light will remain free until they are captured at a defect

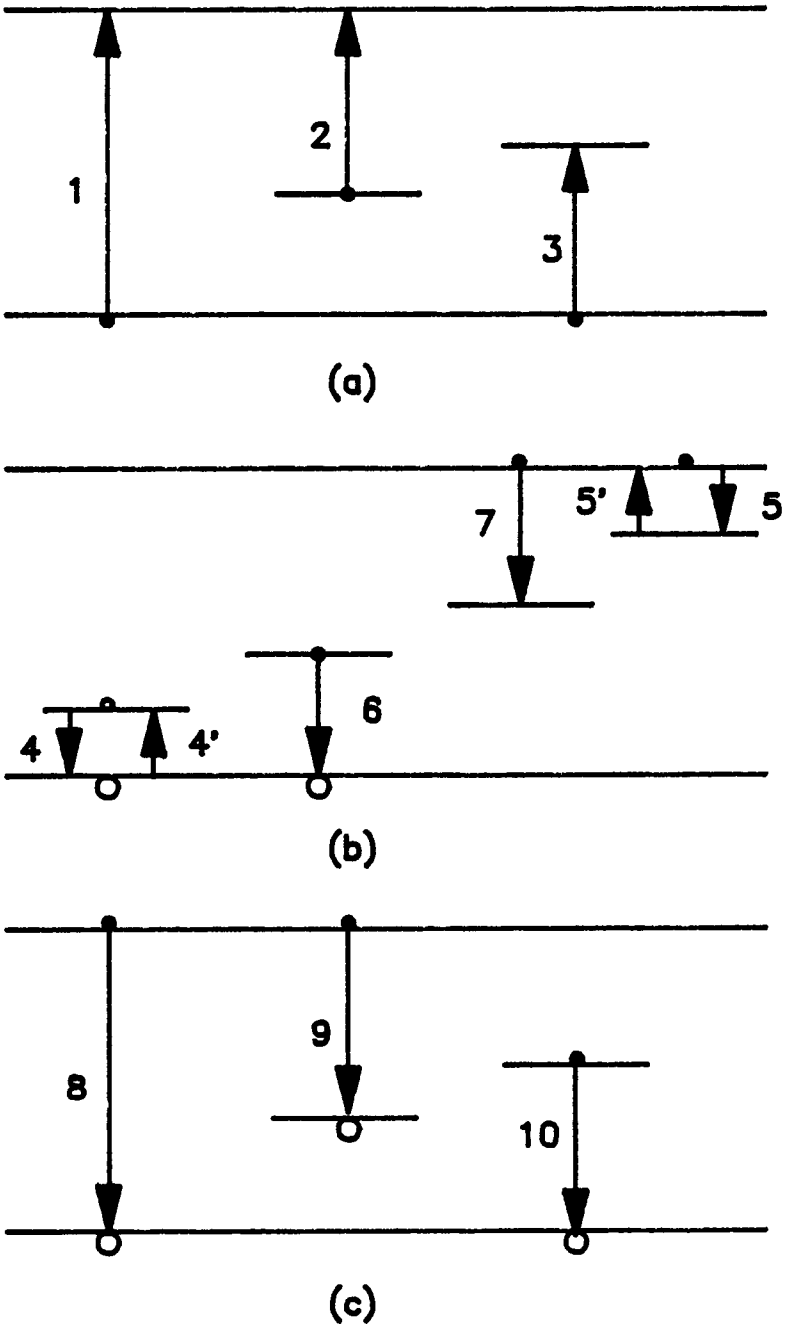

Fig. 2.1 Some common electronic transitions taking place in a photodetector: (a) absorption, (b) trapping and capture, and (c) recombination.

or recombine directly or pass out of the crystal at the electrodes. The capturing centers are classified into two groups: (1) trapping centers-if the captured carrier has a greater probability of being thermally re-excited to the free state than of recombining with a carrier of opposite sign at the defect; or (2) recombination centers-if the captured carrier has a greater probability of recombining with a carrier of opposite sign at the defect than of being reexcited to the free state. Fig. 2.1(b) shows trapping and thermal release of electrons in electron traps (transitions 5 and 5'); trapping and thermal release of holes in hole traps (electron transitions 4 and 4'); and also capture of an electron (transition 7) or of a hole (electron transition 6) in recombination centers.

Three simple types of recombination transitions are shown in Fig. 2.1(c). Transition 8 corresponds to a free electron recombining directly with a free hole and is usually radiative. Recombination also occurs through recombination centers (transitions 9 and 10) and could be either radiative or nonradiative.

When a homogeneous semiconductor material is uniformly illuminated under bias, five possibile situations exist [7] depending on whether or not carriers may be replenished at the electrodes and on the freedom of the carriers as shown in Fig. 2.2. If both carriers are mobile and replenished at the electrodes (Fig. 2.2(a)), then both contribute to the photoconductivity until recombination takes place. The life times of free electrons and free holes are equal in the absence of traps and the gain is given by

$$\Gamma = (\mu_n + \mu_p)\tau E/L \qquad (2.16)$$

where $\tau = \tau_n = \tau_p$.

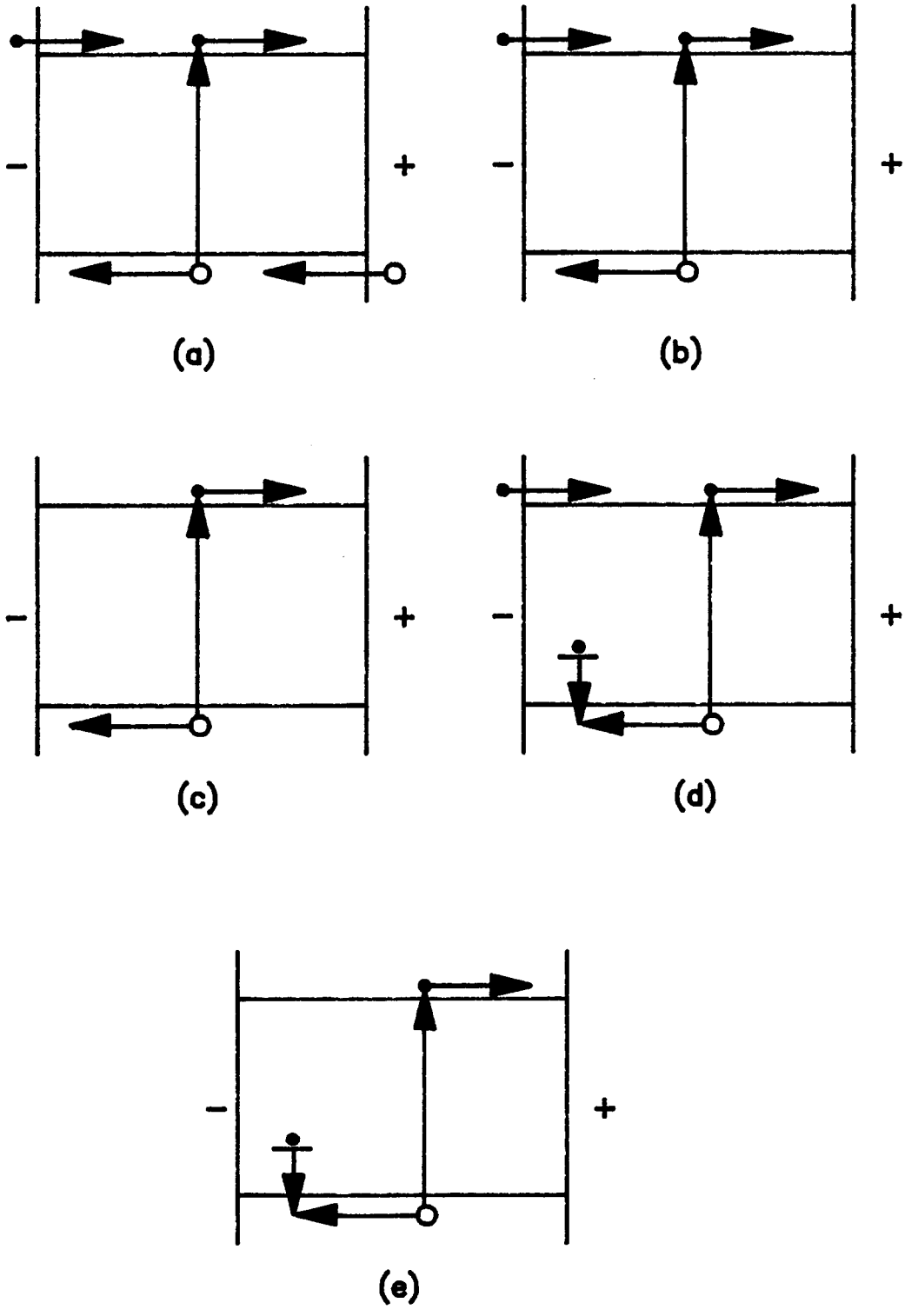

Fig. 2.2 Five types of homogeneous photodetectors.

Fig. 2.2(b) shows the case when both carriers are mobile but only one carrier(electron) is replenished at the electrodes. The photocurrent saturates at a value of the applied electric field sufficient to sweep out the holes before they take part in recombination. In saturation, the holes contribute to the photocurrent until they are drawn off into the cathode and the electrons contribute to the photocurrent for a time equal to the time it takes to draw the holes off into the cathode. So the life time of a hole is equal to the transit time of the hole in the absence of traps and this is also equal to the life time of the electron. The following equations apply for the case shown in Fig. 2.2(b).

$$\tau_p = t_{tp} = \tau_n = L/(\mu_p E) = L/v_p \tag{2.17}$$

$$t_{tn} = L/(\mu_n E) = L/v_n \tag{2.18}$$

$$\Gamma = (\mu_n + \mu_p)/\mu_p = (v_p + v_n)/v_p \tag{2.19}$$

Fig. 2.2(c) shows the case when both carriers are mobile but neither carrier is replenished at the electrodes. The gain for this case is

$$\Gamma = (\tau_n v_n + \tau_p v_p)/L = (X_+ + X_-)/L \tag{2.20}$$

where X_+ is the distance traveled by the freed positive carrier in the direction of the field before it is trapped or recombined and X_- is the distance traveled by the freed negative carrier in the direction opposite to the field before it is trapped or recombined. Since the maximum value of $X_+ + X_-$ is L, the maximum gain is unity and such a photocurrent is called <u>primary photocurrent</u> in contrast to <u>secondary photocurrent</u> where the gain may be greater than

unity. The photocurrent is proportional to the applied electric field for small values of the field and saturates when the field is high enough to draw off both carriers before they recombine with each other. The photocurrent is proportional to the light intensity.

Fig. 2.2(d) shows the case when only one carrier (electron) is mobile and it is replenished at the electrode. The minority carrier freed by light is captured at a crystal defect so that it can be considered effectively immobile. The photocurrent is mainly contributed by the flow of the majority carriers. The life time of the electron is determined by the recombination with the holes captured at the defects which is equal to the hole trap time. Then for the case shown in Fig. 2.2(d) τ_p can be neglected when compared to τ_n and the expression for gain is given by

$$\Gamma = \tau_n v_n / L = \tau_n / t_{tn}. \qquad (2.21)$$

Fig. 2.2(e) shows the situation where only one carrier is mobile and it is not replenished at the electrode. In this case the observed photocurrent decays with time even under excitation, because of the polarization of the material, and a steady photocurrent can not be maintained.

2.2.1 Photoconductors

The theory of basic photoconductive processes is complex and quite involved [7,8]. However, many practical photoconductive photodetectors can be grouped into two categories. The first group corresponds to the case shown in Fig. 2.2(b) and the second group corresponds to the case shown in Fig. 2.2(d). Each of these is furthur discussed below.

For the first group the effects of traps in the

material are negligible and so both carriers contribute to the photocurrent. If the detector is operated in the linear region of the drift velocity-field curve then the maximum obtainable gain for p and n type materials, respectively, is [9]

$$\Gamma_{max} = (\mu_n + \mu_p)/(2\mu_n) \tag{2.22}$$

$$\Gamma_{max} = (\mu_n + \mu_p)/(2\mu_p). \tag{2.23}$$

If the detector is operated in the saturation region of the velocity-field curve then the maximum gains for p and n type materials, respectively, are

$$\Gamma_{max} = (v_{nsat} + v_{psat})/(2v_{nsat}) \tag{2.24}$$

$$\Gamma_{max} = (v_{nsat} + v_{psat})/(2v_{psat}). \tag{2.25}$$

If the free lifetime of the carriers is equal to the minority carrier transit time then the transit time limited bandwidth is given by

$$BW(t_t \text{ limited}) = 0.38/t_t(\text{minority carrier}). \tag{2.26}$$

Since the photoconductor does not have an intrinsic capacitance the RC time constant is usually smaller than the transit time. So the bandwidth of the photoconductor is given by equation (2.26). Then the gain-bandwidth product depends only on the majority carrier transit time.

For the second group of photodetectors the minority carrier is captured by the traps in the material and usually the trapping time is much greater than the majority carrier transit time. So gains much greater than those given by equations (2.22) and (2.23) are possible at low fields. The gain-bandwidth product, however, still depends only on the

majority carrier transit time, so the bandwidth for these detectors is degraded.

2.2.2 Photodiodes

A p-i-n phtodiode is shown in Fig. 2.3. Under large reverse bias the lightly doped intrinsic (i) region is completely depleted and the field in the i region could exceed the saturation field (the field at which the drift velocities of the carriers are saturated). The generated EHPs in the i region and in the depletion regions of the p and the n regions due to the incident light will be swept out by the high fields in those regions. Some of the electrons (holes) generated within a distance L_n (L_p) of the p (n) depletion region will diffuse to the junction and will be swept across by the fields, L_n and L_p being the diffusion lengths. The carriers can not be replenished at the contacts so the maximum gain is one. This corresponds to the case shown in Fig. 2.2(c).

The field in the depletion region is usually greater than the field required for the carriers to travel at saturation velocities. The maximum velocity of electrons (holes) collected along $L+L_n$ ($L+L_p$) is v_{nsat} (v_{psat}). The mean velocity will be smaller because of the combination of both diffusion and drift. A reasonable approximation for transit time is [9]

$$t_t = (L_p + L + L_n)/v_{sat} \qquad (2.27)$$

where v_{sat} is the smaller of v_{nsat} and v_{psat}.

If the low-doped i layer is removed, then a simple p-n photodiode is obtained. This detector would have a large capacitance (because of small L), a small quantum efficiency (because all of the incident light may not be absorbed in

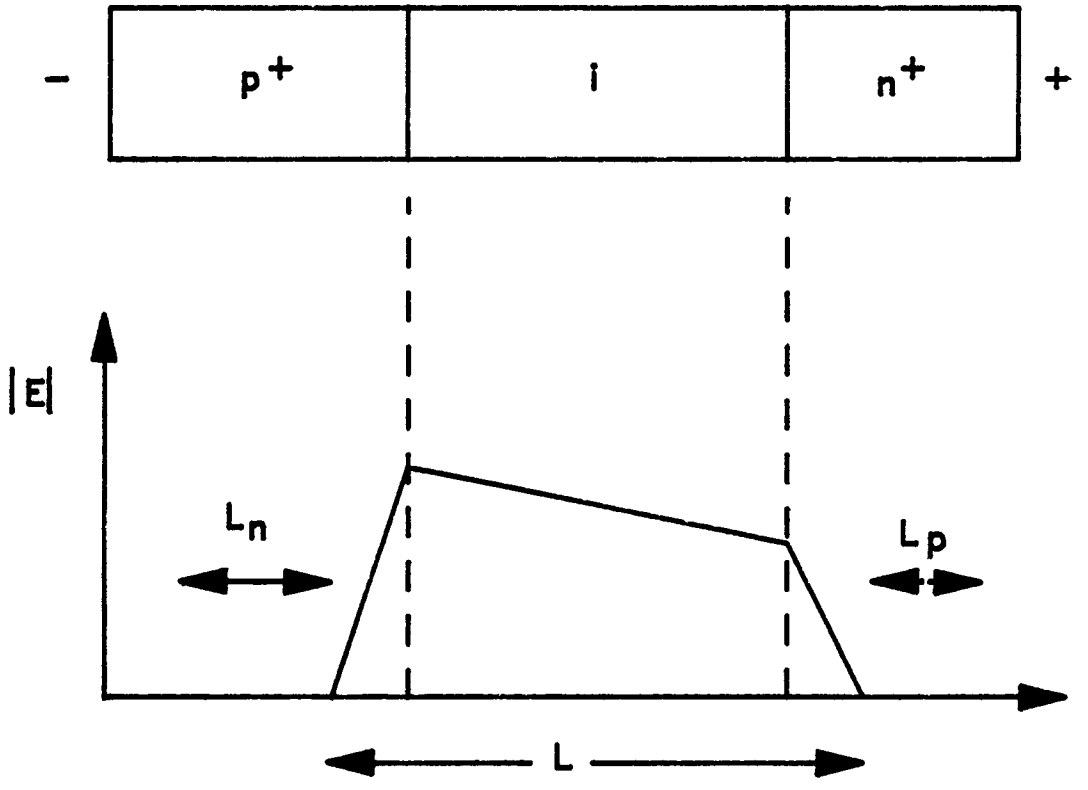

Fig. 2.3 A p–i–n photodiode and its field distribution under reverse bias.

the depletion region L) and a large transit time limited bandwidth. If the p-n photodiode is operated close to the reverse breakdown voltage, then the detector is called an APD. In an APD very high gains are possible because of avalanche multiplication. The transit time limited bandwidth of an APD depends on the ratio of electron and hole ionization rates [6]. Ionization rate of a particular carrier is the number of EHPs generated by that carrier per unit distance traveled.

2.2.3 Schottky photodetectors

Two types of Schottky photodetectors are shown in Fig. 2.4 under typical reverse biased conditions. Fig. 2.4(a) shows a simple Schottky diode. The EHPs generated in the surface depletion region are separated by the action of the internal field as in a p-n junction photodiode. To avoid large reflection and absorption losses when the diode is illuminated through the metal contact, the thickness of the metal film is ~ 100 A and an antireflection coating is also used [6]. Usually the minority carrier has the larger transit time and for the case shown in Fig. 2.4(a) is given by [9]

$$t_t = (L+L_p)/v_{psat}. \tag{2.28}$$

The maximum gain is one since the carriers can not be replenished at the contacts. By using a low-doped i-layer a metal-i-n photodiode similar to a p-i-n photodiode can be made [6]. If the field in the depletion region is close to the breakdown field then avalanche multiplication can be achieved.

Fig. 2.4(b) shows a metal-semiconductor-metal (MSM) photodetector which is a back-to-back Schottky barrier and

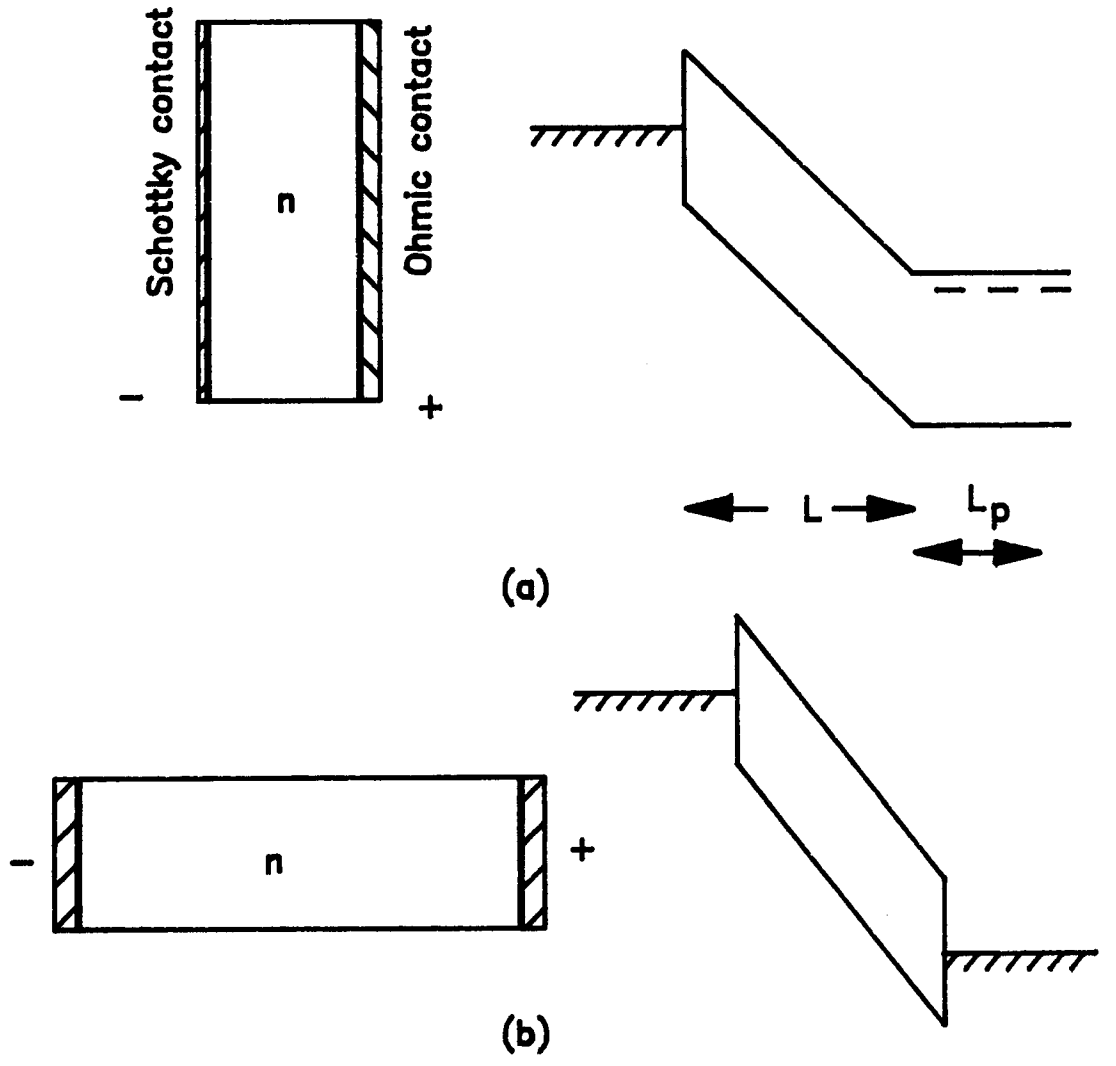

Fig. 2.4 (a) A schottky barrier photodiode under reverse bias. (b) An MSM photodiode under bias

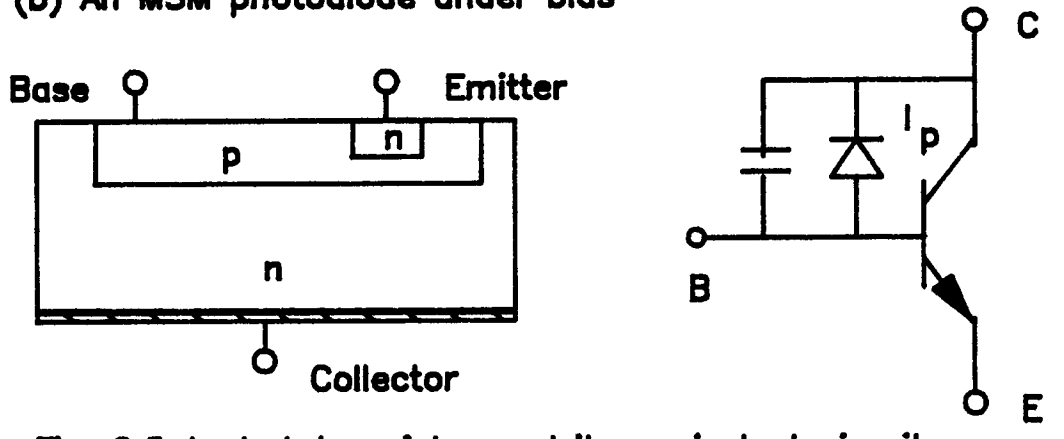

Fig. 2.5 A phototransistor and its equivalent circuit.

is also called a Mott diode [9]. If the applied bias is large enough such that the depletion regions of the two Schottky diodes merge with each other then the carriers generated anywhere between the two contacts would travel at saturation velocities and the bandwidth is given by [9]

$$t_t = 2L/(v_{nsat} + v_{psat}). \tag{2.29}$$

2.2.4 Phototransistors

A phototransistor achieves gain through the transistor action [6]. An npn bipolar phototransistor and its equivalent circuit model are shown in Fig. 2.5. A phototransistor differs from a conventional bipolar transistor by having a large base-collector junction on which the light is incident. When the base lead is floating, the photogenerated carriers contribute a primary photocurrent I_p in the collector. The holes generated in the base and the holes swept into the base from the collector lower the base-emitter built-in potential allowing electrons to be injected across the base to the collector. The total collector current is

$$I_t = I_p + h_{FE}I_p = (1+h_{FE})I_p \tag{2.30}$$

where h_{FE} is the dc common-emitter current gain so the gain for a phototransistor is $(1+h_{FE})$, typically around 100. The fabrication of a phototransistor is more complex than that of a photodiode and the frequency response of a phototransistor is also limited by the large base-collector capacitance and is reduced furthur by the gain of the detector due to feedback effects [6]. Because of these limitations phototransistors are rarely used for high speed applications.

2.3 Literature review

A general comparison of gain and bandwidth of photodetectors in the near-infrared range (0.8 μm to 1.7 μm) was given by Beneking [9]. Wojtcjuk et al. [10] have compared several easily integrable photodetectors made on Cr doped SI-GaAs substrate. The design theory of p-i-n photodiodes was given by Bowers et al. [11]. Both p-i-n [12] and APD [13] detectors were shown to be integrable with GaAs MESFETs. Wang et al. [14],Parker et al. [15] and Rav-Noy et al. [16] have shown that the Schottky barrier photodiodes with thin transparent electrodes could have bandwidths as high as 110 GHz with very small light sensing areas.

Modulation doped photodetectors in GaAs/AlGaAs system were probed by Chen et al. [3,4,17] and Pang et al. [18]. One particular modulation doped detector was shown to be capable of operating without any bias [3]. The long fall times observed in the pulse response of these detectors was shown to be due to the slow moving holes [4]. Several authors [19-23] have studied the GaAs MESFET itself as a potential high speed photodetector with and without the presence of the gate electrode.

Forrest [24,25] has shown that the photoconductive structures can be used for high speed photodetector applications though sometimes they require equalization. A vertical photoconductive structure was studied by Gammel et al. [21] for high speed applications. But most of the work was done on planar photoconductor structures.

Photoconductive detectors made on undoped or lightly doped epi layers were shown by Vilcot et al. [26] and Matsuo et al. [27] to have large gains at low frequencies and at low power levels. The mechanism for gain in these detectors was also suggested by them. The noise characteristics of

these detectors were explored by Vilcot et al. [28] and the detectivity by Constant et al. [29]. The impedance properties of these detectors were probed by Wojtczuk et al. [30] and the space charge domains formed at high fields were investigated by Wei et al. [31]. The microwave properties of epi-layer photoconductors have also been characterized [32]. Darling et al. [33] replaced the ohmic metal contacts by highly doped n^+ contacts and the detector had a better sensitivity. Lam et al. [34] studied the properties of surface depleted photoconductors. Photoconductors made on epi-layers of GaAs have also been integrated with GaAs MESFETs [35,36].

The speed of the photoconductors can be increased by shortening the lifetime of the minority carriers at the expense of responsivity. Approaches used to enhance the speed include radiation damage [37] and amorphization [38]. Roth et al. [39] have shown that detectors fabricated on p-epi layers also have fast response times. More work was done on GaInAs photoconductive detectors [40,41] which can be used in the wavelength range of 1.0 μm to 1.6 μm.

Several authors [42-45] have studied the characteristics of MSM photodetectors made on implanted or epi layers of GaAs. The impulse response curve for some of these detectors is nearly symmetrical. Gain was observed in some detectors even though it is not as high as the gain observed in the photoconductive detectors. Possible mechanisms of gain were also discussed [42,44]. The dark current was shown to be the lowest for Schottky contacts made out of WSi_x metal [44]. Bandwidths as high as 105 GHz have been achieved for a detector size of 10 μm X 15 μm [45]. Analysis and modeling of these fast detectors were carried out by Van Zeghbroeck [46] and Koscielniak et al.

[47,48]. The noise characteristics were studied by Wada et al. [49]. An MSM photodetector fabricated on quasi-ternary (GaAs doped with 1% indium) grown GaAs material was shown [50] to have very low dark current. These MSM photodetectors were also shown to be easily integrable with GaAs MESFETS [51-54].

Work has also been reported on detectors made directly on SI-GaAs substrates [55-60]. The gain measurements, temperature measurements, and spectral response measurements were carried out by Schumm [61] and Yang [62] on detectors made with both ohmic and Schottky contacts. Koscielniak et al. [63] have shown that MSM photodetectors made on SI-GaAs with Au islands between the fingers have higher responsivity but decreased bandwidth. Nakajima et al. [64] have studied the properties and developed a theory of MSM detectors made on SI-GaAs material. Hammond et al. [65] have studied the characteristics of Fe doped InP photoconductive detectors.

3. MODELING AND DESIGN OF INTERDIGITATED STRUCTURE

3.1 Introduction

The interdigitated structure (IDS) has become a useful element in recent years and has been used as contact electrodes in photodetectors [56], as a capacitor and band pass filter in monolithic microwave integrated circuits [66], as modulating electrodes in acousto-optic modulators [67] and as emitter and base contacts in bipolar junction transistors [68]. The analysis and design of the structure has been conducted by using a number of related techniques, leading to an equivalent circuit of the required parameters of the two port network. These circuit elements influence the time response of the interdigitated photodetectors.

The models of Matthaei [69] and Ren [70] consider the IDS in stripline configuration and the model of Williams [71] considers the IDS in coplanar waveguide configuration. All the other models [72-77] consider the IDS in microstrip configuration. The models of Ou [72] and Chin [73] consider the IDS without the pads which connect the interdigitated fingers. The models of Alley [74], Hobdell [75] and Esfandiari et al. [76] were based on coupled microstrip line theory and calculate the even and odd mode admittances of the interdigitated fingers. These admittances were averaged over the terminal strip's length and were added to the shunt admittance of the terminal strip. They neglect all the other distributed effects of the structure, e.g., the open end effect and the effects of gaps and steps in the microstrip lines. The model of Pettenpaul et al. [77] took into account the phase shift along the terminal strip and also all the other distributed effects of the structure and was based on S-parameter network theory.

In this chapter the IDS is modeled starting with the admittance matrix of the coupled microstrip lines and modifying it to include the distributed elements. Even though the model does not consider the phase shift along the terminal strip, it is shown to be valid well into the GHz range. It is easier to implement than the model based on S-parameter network theory [77]. The model is tested against experimental results and the model of Pettenpaul et al. [77]. The IDS is also modeled without the ground plane.

3.2 Theory

For a single microstrip line, shown in Fig. 3.1(a), the capacitance to ground is made up of the parallel plate capacitance, C_p, and the fringing capacitance, $2C_f$. C_p and C_f are capacitances per unit length of the microstrip line. The fringing capacitance is given by [78]

$$2C_f = C - C_p = 1/(v_p Z_0) - C_p \tag{3.1}$$

where v_p is the phase velocity and Z_0 is the characteristic impedance.

For a pair of symmetric coupled microstrip lines, shown in Fig. 3.1(b), the total even and odd mode capacitances are given as

$$C_e = C_p + C_f + C_f' \tag{3.2}$$

$$C_o = C_p + C_f + C_{ga} + C_{gd} \tag{3.3}$$

where C_f' is the fringing capacitance to ground on the coupled side of the microstrip and C_{ga} and C_{gd} are the fringing capacitances across the gap in the air and dielectric regions, respectively. The capacitance to ground,

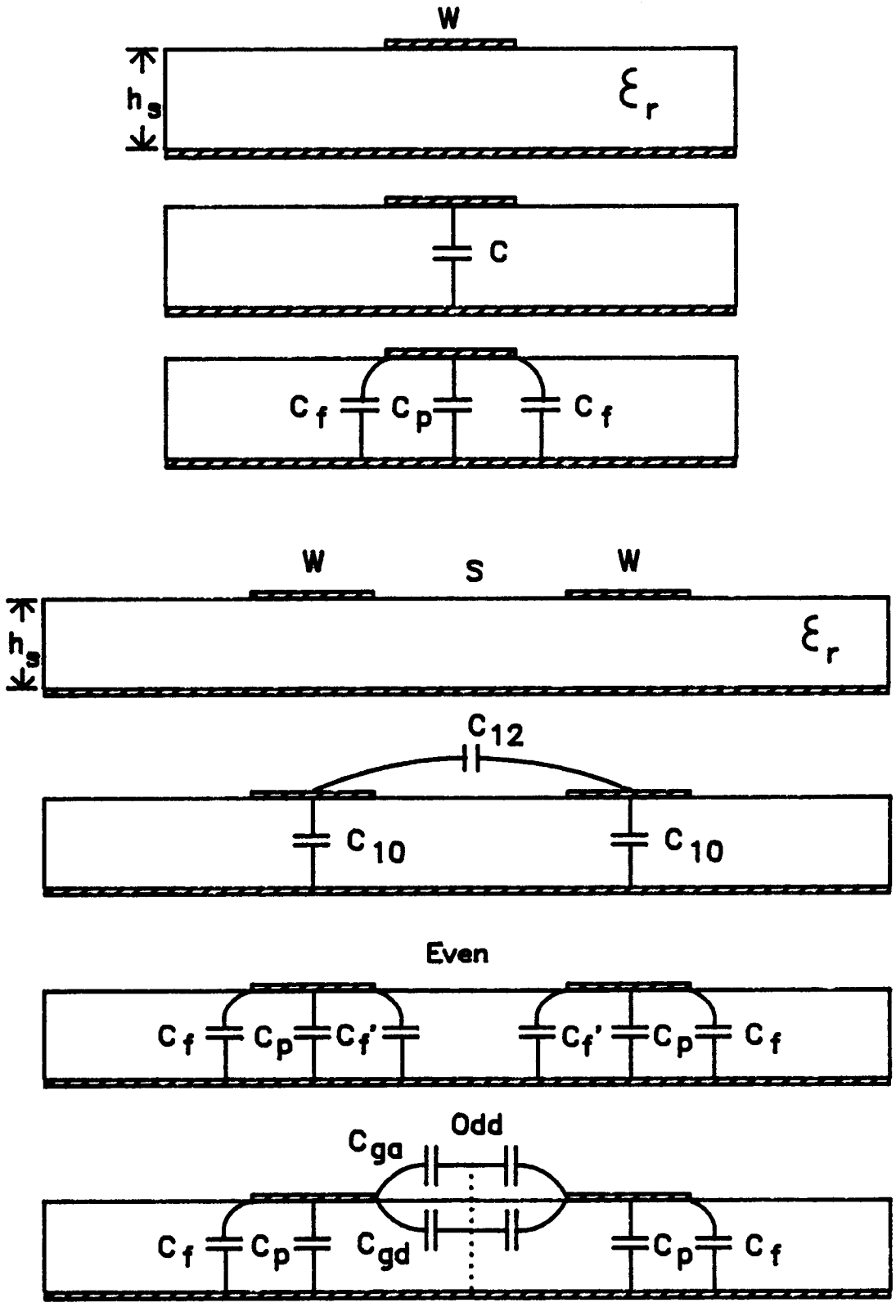

Fig. 3.1 Single and coupled microstrips and their capacitances

C_{10}; the self capacitance, C_{11}, of each line; and the mutual capacitance between the lines, C_{12}, are given in terms of even and odd mode capacitances as

$$C_{10} = C_e = C_p + C_f + C_f' \tag{3.4}$$

$$C_{12} = (C_o - C_e)/2 = (C_{ga} + C_{gd} - C_f')/2 \tag{3.5}$$

$$C_{11} = C_{10} + C_{12} = (C_e + C_o)/2 = C_p + C_f + (C_{ga} + C_{gd} + C_{f'})/2. \tag{3.6}$$

The 4-port admittance matrix for the two coupled lines is [79]

$$Y_{11} = Y_{22} = Y_{33} = Y_{44} = -(j/2)[Y_o\cot(\beta_o l) + Y_e\cot(\beta_e l) \tag{3.7}$$

$$Y_{12} = Y_{21} = Y_{34} = Y_{43} = (j/2)[Y_o\cot(\beta_o l) - Y_e\cot(\beta_e l) \tag{3.8}$$

$$Y_{13} = Y_{31} = Y_{24} = Y_{42} = -(j/2)[Y_o\csc(\beta_o l) - Y_e\csc(\beta_e l) \tag{3.9}$$

$$Y_{14} = Y_{41} = Y_{23} = Y_{32} = (j/2)[Y_o\csc(\beta_o l) + Y_e\csc(\beta_e l) \tag{3.10}$$

$$Y_e = 1/Z_e \tag{3.11}$$

$$Y_o = 1/Z_o \tag{3.12}$$

where $Y_e(Z_e)$ and $Y_o(Z_o)$ are the even and odd mode characteristic admittances(impedances), β_e and β_o are the even and odd mode propagation constants and l is the length of the coupled lines. The even(odd) mode propagation

constant, $\beta_e(\beta_o)$, is related to the even(odd) mode phase velocity, $v_{pe}(v_{po})$, and the even(odd) mode effective dielectric constant, $\varepsilon_{re}(\varepsilon_{ro})$, via

$$\beta_e = \omega/v_{pe} = \omega \sqrt{\varepsilon_{re}}/c \tag{3.13}$$

$$\beta_o = \omega/v_{po} = \omega \sqrt{\varepsilon_{ro}}/c \tag{3.14}$$

where $c = 3 \times 10^8$ m/s is the velocity of light in vacuum and ω is the angular frequency. The impedances and effective dielectric constants of the single and the multiple coupled microstrips are calculated from [79]. The even and odd mode capacitances and inductances are

$$C_e = 1/(v_{pe}Z_e) = \sqrt{\varepsilon_{re}}/(cZ_e) \tag{3.15}$$

$$C_o = 1/(v_{po}Z_o) = \sqrt{\varepsilon_{ro}}/(cZ_o) \tag{3.16}$$

$$L_e = Z_e/v_{pe} = Z_e \sqrt{\varepsilon_{re}}/c \tag{3.17}$$

$$L_o = Z_o/v_{po} = Z_o \sqrt{\varepsilon_{ro}}/c. \tag{3.18}$$

An N_f-coupled interdigitated structure is shown in Fig. 3.2. Assuming a quasi TEM mode of propagation, the equivalent even and odd mode admittances can be estimated by using the capacitance matrix of the two coupled lines as given by [73]

$$Y_{eN} = v_{pe}\{C_{11} - C_{12} + [(N_f/2) - 1](C_{22} - 2C_{12})\} \tag{3.19}$$

$$Y_{oN} = v_{po}\{C_{11} + C_{12} + \{(N_f/2) - 1](C_{22} + 2C_{12})\} \tag{3.20}$$

where C_{11} is the self capacitance of lines 1 and N_f, C_{22} is the self capacitance of lines 2 through N_f-1, and C_{12} is the mutual capacitance between adjacent lines. The coupling between non-adjacent lines is neglected. C_{11} and C_{12} are the

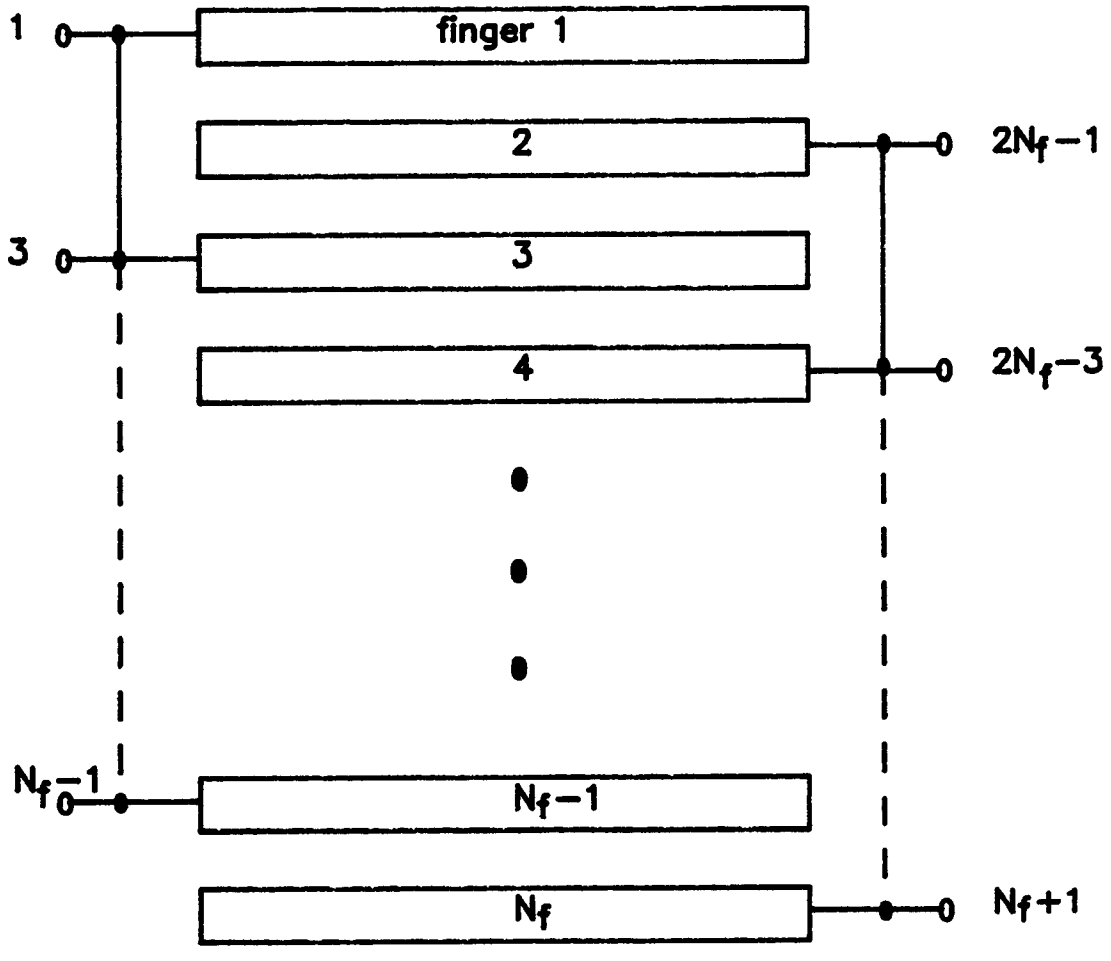

Fig. 3.2 Schematic of an N_f–line, $2N_f$–port interdigitated structure.

same as in equations (3.5) and (3.6). C_{22} is expressed as

$$C_{22} = C_{20} + 2C_{12} = C_p + 2C_f' + 2C_{10}. \quad (3.21)$$

Y_{eN} and Y_{oN} can also be written in terms of parallel plate and fringing capacitances as

$$Y_{eN} = v_{pe}[(N_f/2)C_p + C_f + (N_f-1)C_f'] \quad (3.22)$$

$$Y_{oN} = v_{po}[(N_f/2)C_p + C_f + (N_f-1)(C_{ga} + C_{gd})] \quad (3.23)$$

The IDS and its equivalent circuit are shown in Fig. 3.3. The series resistance, R_s, is made up of contact and spreading resistances and conductor losses of the interdigitated fingers. The various discontinuties in the IDS and their representation as circuit elements are shown in Fig. 3.4. The capacitance of the non-symmetrical gap in the microstrip structure is given by [80]

$$C_g = 5 \times 10^{-10} Q_1 h_s \exp(-1.86G/h_s)\{1 + 4.19\,[1 - \exp(-0.785(h_s/W_1)^{0.5}\, W_2/W_1)]\} \quad (3.24)$$

where

$$Q_1 = 0.04598[0.03 + (W_1/h_s)^{A_c}](0.272 + 0.07\varepsilon_r) \quad (3.25)$$

$$A_c = 1.23/[1 + 0.12(W_2/W_1 - 1)^{0.9}]. \quad (3.26)$$

From Fig. 3-3 W_1 and W_2 are given by

$$W_1 = W \quad (3.27)$$

$$W_2 = W + 2S \quad (3.28)$$

The capacitance and inductance of the microstrip step are given by [80]

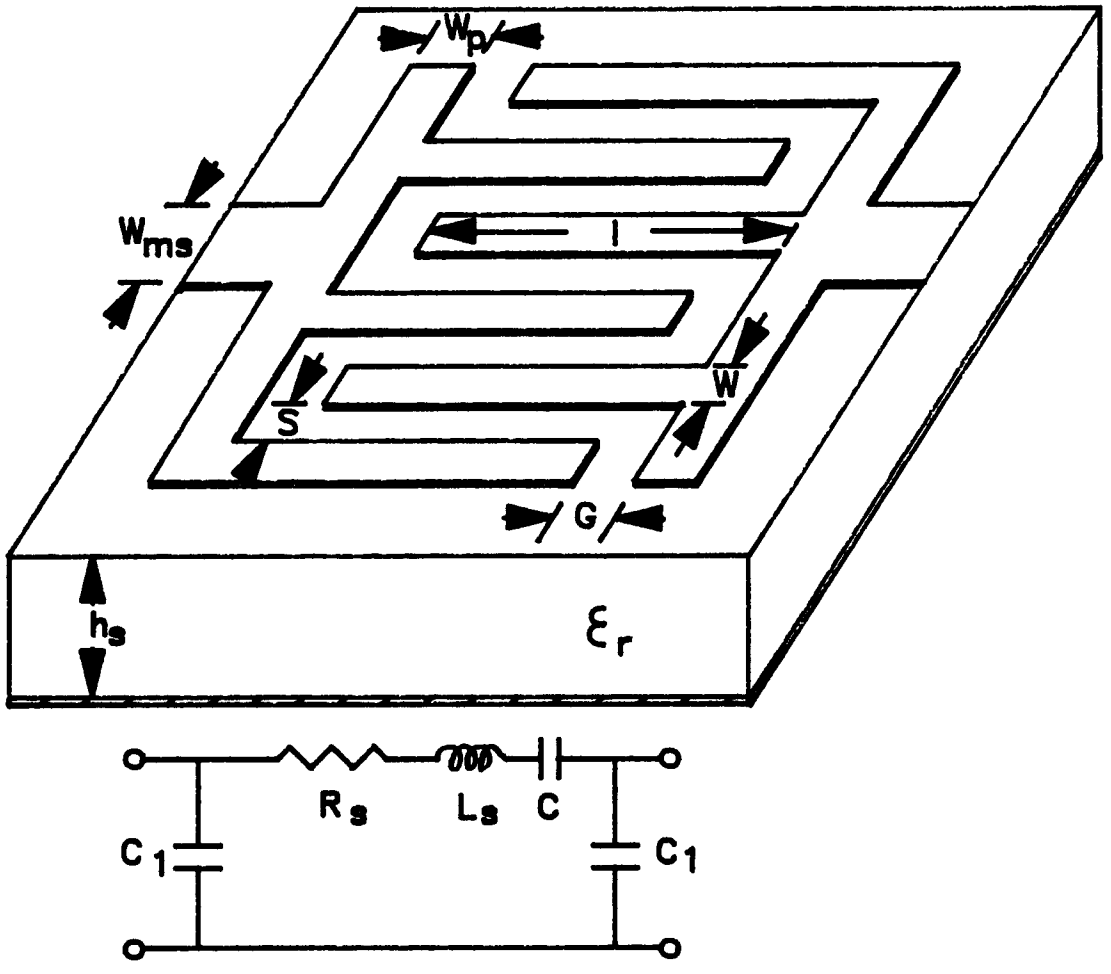

Fig. 3.3 Interdigitated structure and its equivalent circuit.

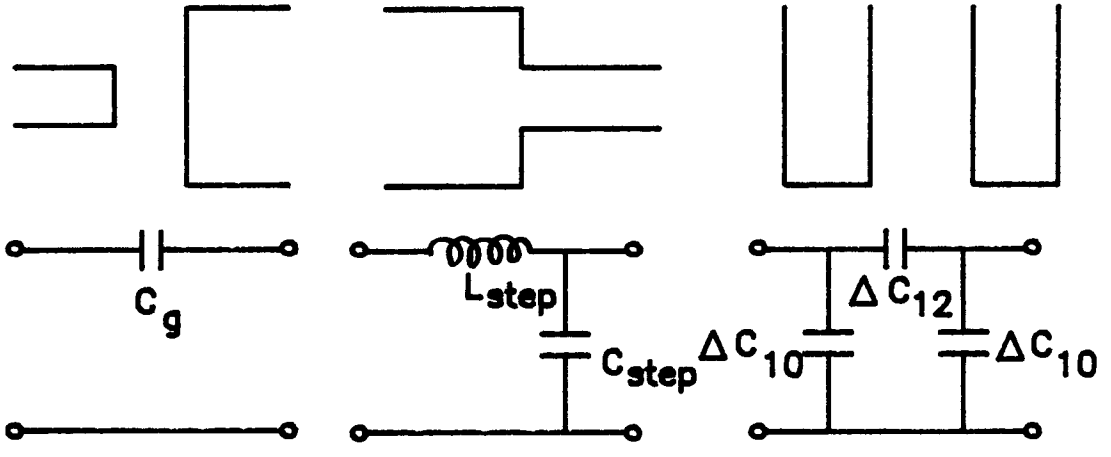

Non-symmetrical gap Step Open end coupled lines

Fig. 3.4 Discontinuties in the interdigitated structure and their representation as circuit elements.

$$C_{step}(pF) = \sqrt{W_1 W_2}\ \{[4.386\ \log(\varepsilon_r) + 2.33]W_2/W_1 - 5.472\ \log(\varepsilon_r) - 3.17\} \quad (3.29)$$

$$L_{step}(nH) = h_s[40.5(W_2/W_1 - 1) - 32.57\ \log(W_2/W_1) + 0.2\ (W_2/W_1 - 1)^2] \quad (3.30)$$

where W_1 and W_2 are given by equations (3.27) and (3.28).

The capacitances of the open end coupled lines are given by [81]

$$\Delta C_{10} = \Delta C_e = \varepsilon_0 \varepsilon_r \Delta L_e W/h_s \quad (3.31)$$

$$\Delta C_{12} = (\Delta C_o - \Delta C_e)/2 = \varepsilon_0(\varepsilon_{reff}\Delta L_o - \varepsilon_r \Delta L_e)W/h_s \quad (3.32)$$

where ΔL_e and ΔL_o are the increments in the line length of the open end coupled microstrips for the even and odd modes, respectively, and are given as

$$\Delta L_e = [(\Delta 2L - \Delta L + 0.0198\ h_s G_1^{R1})\ \exp(-0.328 G_1^{2.244}) + \Delta L] \quad (3.33)$$

$$\Delta L_o = [(\Delta L - h_s R_3)(1 - \exp(-R_4)) + h_s R_2] \quad (3.34)$$

where

$$G_1 = (W + 2S)/h_s \quad (3.35)$$

$$R_1 = 1.187[1 - \exp(-0.069 U^{2.1})] \quad (3.36)$$

$$R_2 = 0.343 U^{0.6187} + [0.45\varepsilon_r/(1 + \varepsilon_r)]\ U^{R5} \quad (3.37)$$

$$R_3 = 0.2974\ [1 - \exp(-R_2)] \quad (3.38)$$

$$R_4 = (0.271 + 0.0281\varepsilon_r) G_1^{[1.167\varepsilon_r/(0.66 + \varepsilon_r)]} + [1.025\varepsilon_r/(0.687 + \varepsilon_r)] G_1^{[0.958\varepsilon_r/(0.706 + \varepsilon_r)]} \quad (3.39)$$

$$R_5 = 1.357 + 1.65/(1 + 0.7\varepsilon_r) \tag{3.40}$$

$$U = W/h_s \tag{3.41}$$

ΔL is the increment in the line length of a single microstrip with an open end and is given as [81]

$$\Delta L = h_s P_1 P_2 P_3 / P_4 \tag{3.42}$$

where

$$P_1 = 0.434907 \frac{(U_1^{0.8544} + 0.236)\ (\varepsilon_{reff}^{0.81} + 0.26)}{(U_1^{0.8544} + 0.87)\ (\varepsilon_{reff}^{0.81} - 0.189)} \tag{3.43}$$

$$P_2 = 1 - 0.218 \exp(-7.5U_1) \tag{3.44}$$

$$P_3 = 1 + \{0.5274 \tan^{-1}[0.084U_1^{(1.9413/B)}]\} / \varepsilon_{reff}^{0.9236} \tag{3.45}$$

$$P_4 = 1 + 0.0377 \tan^{-1}(0.067U_1^{1.456}) \{6 - 5 \exp[0.036\ (1 - \varepsilon_r)]\} \tag{3.46}$$

$$U_1 = W/h_s \tag{3.47}$$

$$B = 1 + U_1^{0.371} / (1 + 2.358\ \varepsilon_r) \tag{3.48}$$

$\Delta 2L$ is calculated in the same way as ΔL except for W in equation (3.47) for U_1 is replaced by 2W.

3.3 Modeling technique

The conductor and dielectric losses are not included here but can be easily incorporated in the model, i.e, R_s is not modeled. Although it is possible to model the

interdigitated structure in terms of the multiport admittance matrix ($2N_f$ port), it is convenient to formulate the analysis in terms of the equivalent four port representation. The equivalent even and odd mode admittances of the N_f-coupled interdigitated fingers, which are given by equations (3.19) and (3.20), are used to reduce the N_f-line, $2N_f$-port admittance matrix to a 2-line, 4-port admittance matrix by replacing Y_e and Y_o by Y_{eN} and Y_{oN}, respectively, in equations (3.7) to (3.10). The discontinuties are modeled by using known reliable equivalent circuit models.

The total capacitance due to the non-symmetrical gaps between the fingers and the pads is

$$C_{gt} = (N_f/2)C_g \tag{3.49}$$

for each side of the pad since they are all in parallel. The total capacitance and inductance due to the microstrip steps at the pads are

$$C_{st} = (N_f/2)C_s \tag{3.50}$$

$$L_{st} = L_s/(N_f/2) \tag{3.51}$$

Finally, the total ground and mutual capacitances due to open end coupled lines are

$$\Delta C_{10t} = (N_f/2)\Delta C_{10} \tag{3.52}$$

$$\Delta C_{12t} = (N_f - 1)\Delta C_{12} \tag{3.53}$$

The modified 2-line, 4-port admittance matrix of the n-interdigitated fingers is now augmented as shown in Fig. 3.5 to include the effects of the discontinuties in the structure. When all the capacitors are taken inside, the 4-port admittance matrix is modified as

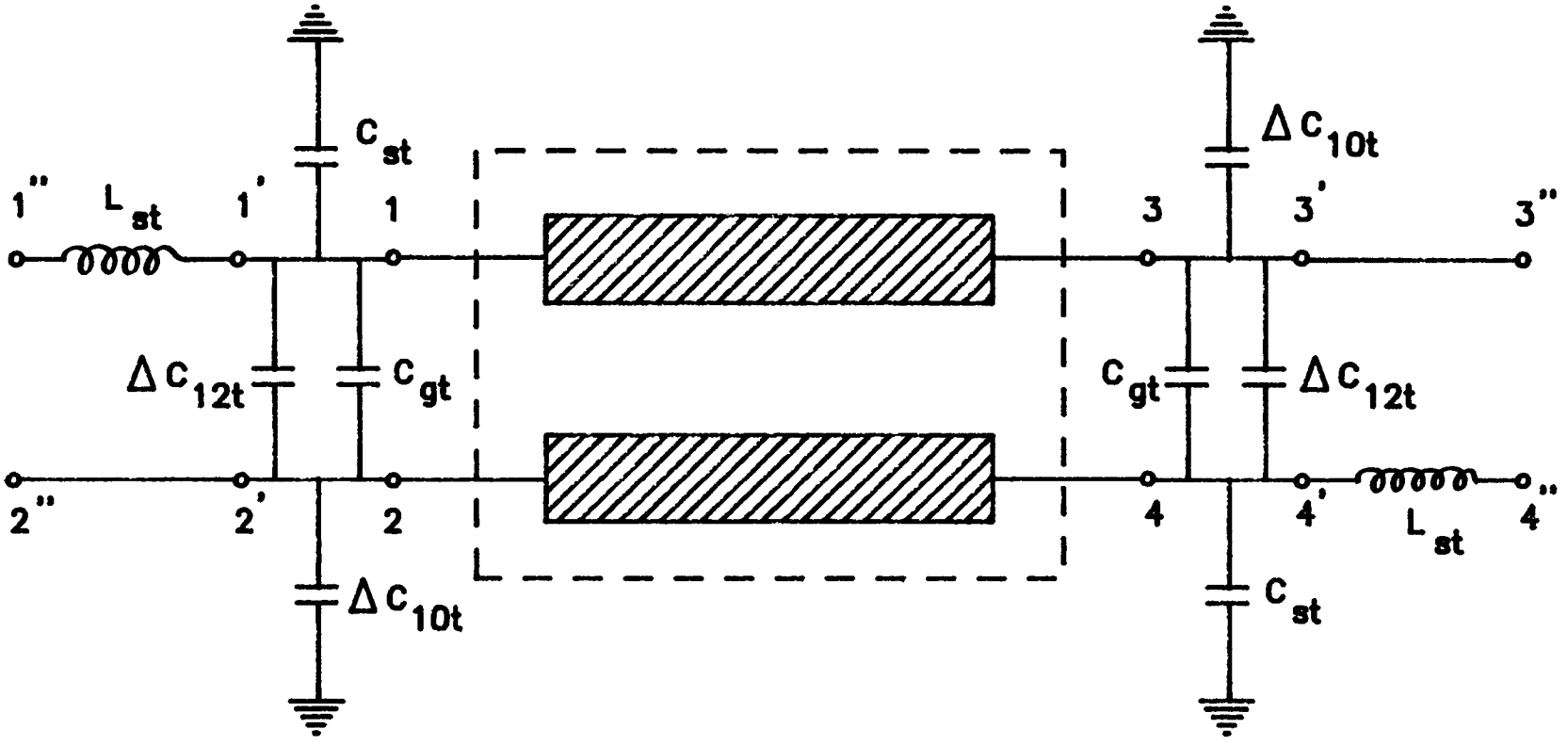

Fig. 3.5 Four-port network of IDS with effects of the discontinuties included.

$$Y_{1'1'} = Y_{3'3'} = Y_{11} + j\omega(C_{gt} + C_{st} - \Delta C_{12t}) \quad (3.54)$$

$$Y_{2'2'} = Y_{4'4'} = Y_{11} + j\omega\,(C_{gt} + \Delta C_{10t} - \Delta C_{12t}) \quad (3.55)$$

$$Y_{1'2'} = Y_{2'1'} = Y_{3'4'} = Y_{4'3'} = Y_{12} - j\omega(C_{gt} - \Delta C_{12t}) \quad (3.56)$$

$$Y_{1'3'} = Y_{3'1'} = Y_{2'4'} = Y_{4'2'} = Y_{13} \quad (3.57)$$

$$Y_{1'4'} = Y_{4'1'} = Y_{2'3'} = Y_{3'2'} = Y_{14} \quad (3.58)$$

and the new ports are 1', 2', 3' and 4'. There is no current flow through ports 2' and 3' since they are open circuited . The modified 4-port admittance matrix is inverted and is reduced to 2-port impedance matrix by applying the boundary conditions of zero current at ports 2' and 3'. The 2-port impedance matrix is augmented to include the inductance as

$$Z_{1"1"} = Z_{4"4"} = Z_{1'1'} + j\omega L_{st} \quad (3.59)$$

$$Z_{1"4"} = Z_{4"1"} = Z_{1'4'} \quad (3.60)$$

The 2-port admittance matrix is obtained by inverting the above impedance matrix.

For the center tapped IDS shown in figure 3.3 where ports 1, 2, 3 and 4 are open circuited the impedance matrix for each half section is given by [76]

$$Z'_{11} = Z'_{22} = (1/2)[Z_{Te}\coth(\beta_{Te}l_T/2) + Z_{To}\coth(\beta_{To}l_T/2)] \quad (3.61)$$

$$Z'_{21} = Z'_{12} = (1/2)[Z_{Te}\coth(\beta_{Te}l_T/2) - Z_{To}\coth(\beta_{To}l_T/2)] \quad (3.62)$$

$$l_T = N_f W + (N_f - 1)S \quad (3.63)$$

where Z_{Te}, Z_{To} and β_{Te}, β_{To} are the characteristic impedances and propagation constants for the terminal strip and l_T is the length of the terminal strip. The total admittance of the terminal strips is

$$Y_{T11} = 2Y'_{11} \tag{3.64}$$

$$Y_{T12} = 2Y'_{12} \tag{3.65}$$

where the admittance matrix $[Y'] = [Z']^{-1}$. When the fingers are connected to the terminal strips, the fingers can be represented by an effective distributed shunt admittance across the terminal strip. Thus at an angular frquency ω the line parameters for the terminal strips with fingers connected are

$$Z_{Te} = \sqrt{L_{Te} / [C_{Te} + (y_{11} + y_{12})/(j2\omega l_T)]} \tag{3.66}$$

$$Z_{To} = \sqrt{L_{To} / [C_{To} + (y_{11} - y_{12})/(j2\omega l_T)]} \tag{3.67}$$

$$\beta_{Te} = j\omega\sqrt{L_{Te}[C_{Te} + (y_{11} + y_{12})/(j2\omega l_T)]} \tag{3.68}$$

$$\beta_{To} = j\omega\sqrt{L_{To}[C_{To} + (y_{11} - y_{12})/(j2\omega l_T)]} \tag{3.69}$$

where $[y] = [Z]^{-1}$ obtained from (3.59) and (3.60) and C_{Te}, C_{To} and L_{Te}, L_{To} can be calculated from Z_{Te}, Z_{To} and β_{Te}, β_{To} using equations (3.15)-(3.18).

The insertion loss of the IDS can be calculated with 50 Ω source and load impedances. If we add the microstrip's step inductance and capacitance resulting from the microstrip connecting the pads to the source and the load, then the overall circuit is as shown in Fig. 3.6. The step

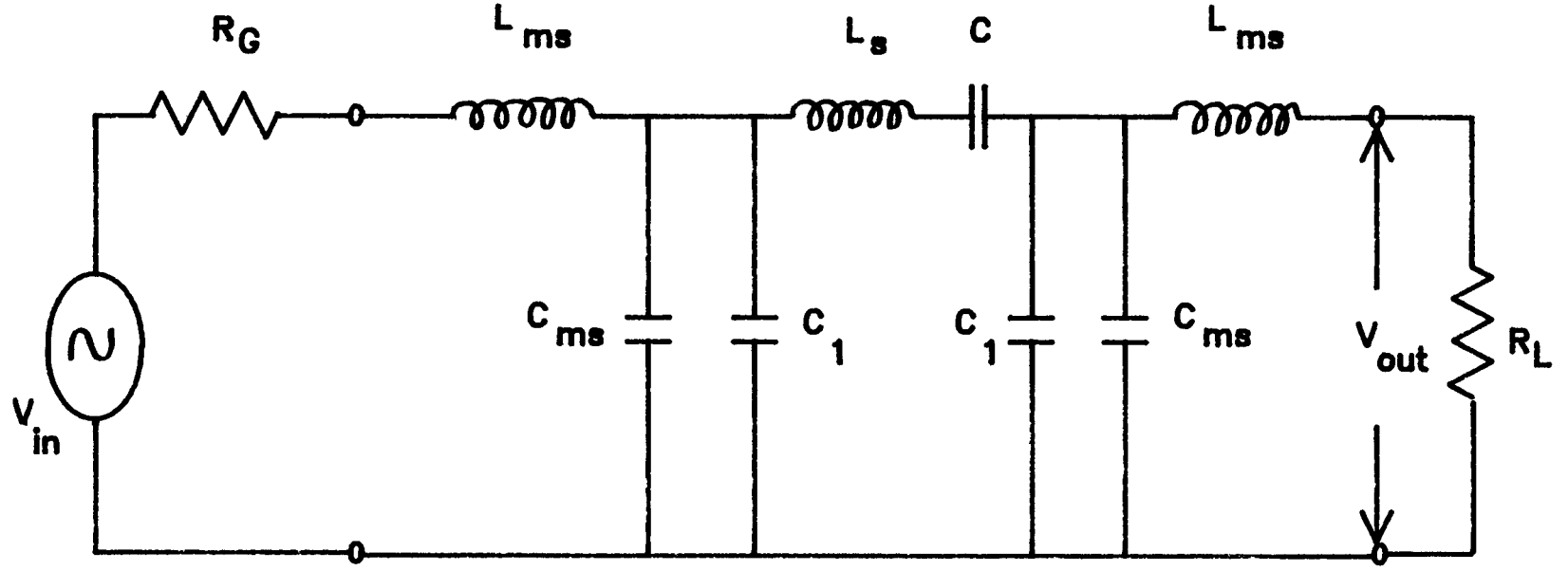

Fig. 3.6 Circuit used to calculate the insertion loss of the IDS.

inductance L_{ms} and capacitance C_{ms} are calculated from equations (3.29) and (3.30). The derived expression for insertion loss is

$$S_{21}(dB) = 20 \log(V_o/V_{in}) = (\omega R_L C)^2/[(A_1^2+A_2^2)(A_3^2+A_4^2)] \quad (3.70)$$

where

$$R_L = R_G = 50\ \Omega \quad (3.71)$$

$$A_1 = \omega R_L C_t \quad (3.72)$$

$$A_2 = \omega^2 L_{ms} C_t - 1 \quad (3.73)$$

$$A_3 = \omega^2 (2L_{ms}C + L_s C + L_{ms}C_t) - \omega^4 L_s C L_{ms} C_t - 1) \quad (3.74)$$

$$A_4 = \omega^3 L_s C R_L C_t - \omega R_L (2C + C_t) \quad (3.75)$$

$$C_t = C_p + C_{ms} \quad (3.76)$$

The experimentally measured insertion loss can be compared with the modeled insertion loss.

3.4 IDS without the ground plane

When there is no ground plane the capacitance to ground C_p in Fig. 3.3 is eliminated. The interdigitated fingers can then be modeled as coupled coplanar strips. For a pair of coplanar strips shown in Fig. 3.7, the line capacitance per unit length is given as [78]

$$C_c = \varepsilon_0 \varepsilon_{reff}\ K(d')/K(d) \quad (3.77)$$

where

$$d = S/(S + 2W) \quad (3.78)$$

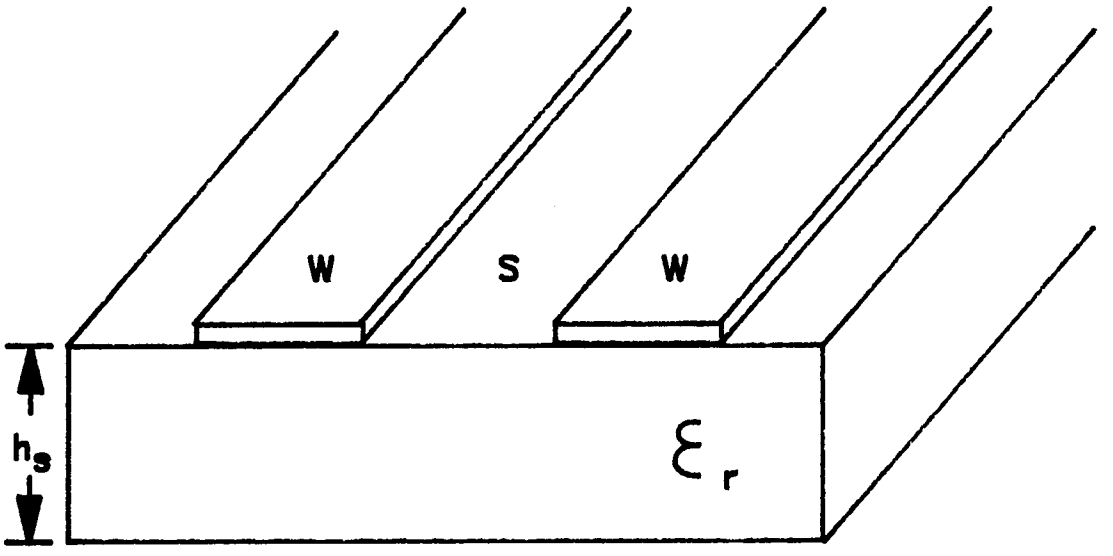

Fig. 3.7 Coplanar strips.

$$d' = \sqrt{1 - d^2} \tag{3.79}$$

$$\varepsilon_{reff} = [(1+\varepsilon_r)/2]\{\tanh[0.785 \ln(h_s/W) + 1.75] + (Wd/h_s)[0.04-0.7d+0.01(1-0.1\varepsilon_r)(0.25+d)]\} \tag{3.80}$$

and K is the complete elliptic function of the first kind. The gap capacitance, C_g, between each finger and the pad is also given by equation (3.77) but the values of W and S are modified as

$$W = W_p \tag{3.81}$$

$$S = G \tag{3.82}$$

When there are n interdigitated fingers of length l, the total capacitance of the fingers considering only nearest neighbor coupling is given by

$$C_T = (N_f-1)Cl + N_f C_g W \tag{3.83}$$

The actual value of C_T would be slightly smaller than the value given by equation (3.83) because of multiple coupled lines. The approximate value of C_c per meter can also be calculated from equation (3.5) by substituting zero for C_f' as follows

$$C_c = (C_{ga} + C_{gd})/2 \tag{3.84}$$

The series resistance, R_s, is given in terms of the metal sheet resistance, R_{sh} as [82]

$$R_s = 4R_{sh}l/3N_f W \tag{3.85}$$

3.5 Results

The reflection coefficient, S11, of the IDS shown in

Fig. 3.8 is measured on two substrate materials, alumina and sapphire. The measurements are taken on a HP8510 network analyzer using Cascade Microtech planar probes. The real and imaginary parts of the measured S11 and the calculated S11 are plotted in Figs. 3.9 and 3.10 for the two substrates. The results are in reasonable agreement considering the fact the that the IDS shown in Fig. 3.8 has some extra bends in it to facilitate the measurement. A figure of accuracy is how close are the measured and predicted resonant frequencies. The resonant frequency occurs when the real part of S11 is equal to 1. As can be seen from Figs. 3.9 and 3.10, the resonant frequency is predicted within 0.5 GHz of the measured one.

In table 3.1 the values of C and C_1 of this model are compared with those of Pettenpaul et al. [77] for three values of N. The C values are in good agreement.The C_1 values of Pettenpaul et al. [77] seem to be incorrect. The value of C_1 is the sum of the parallel plate capacitance and the even mode fringing capacitance to ground. The static capacitance of the fingers to ground, C_{10s}, is

$$C_{10s} = [C_f + (N_f/2)C_p + (N_f-1)\ C_f'] \ l \qquad (3.86)$$

where C_p is the parallel plate capacitance per meter. For a finger width and spacing of 10 um the values of C_p, C_f and C_f' are 8.147 pF/m, 40.7 pF/m and 10.49 pF/m, respectively. The capacitance of the pads, C_{Pad}, connecting the interdigitated fingers is added to C_{10s} to get the total capacitance to ground, C_1. The approximate value of C_{Pad} for a 10 μm width pad is 50 pF per meter. For a finger length of 100 μm, the values of C_1 for various N are: $C_1(N_f=5)$ = 15 fF, $C_1(N_f=10)$ = 27 fF, and $C_1(N_f=20)$ = 52 fF. The values of

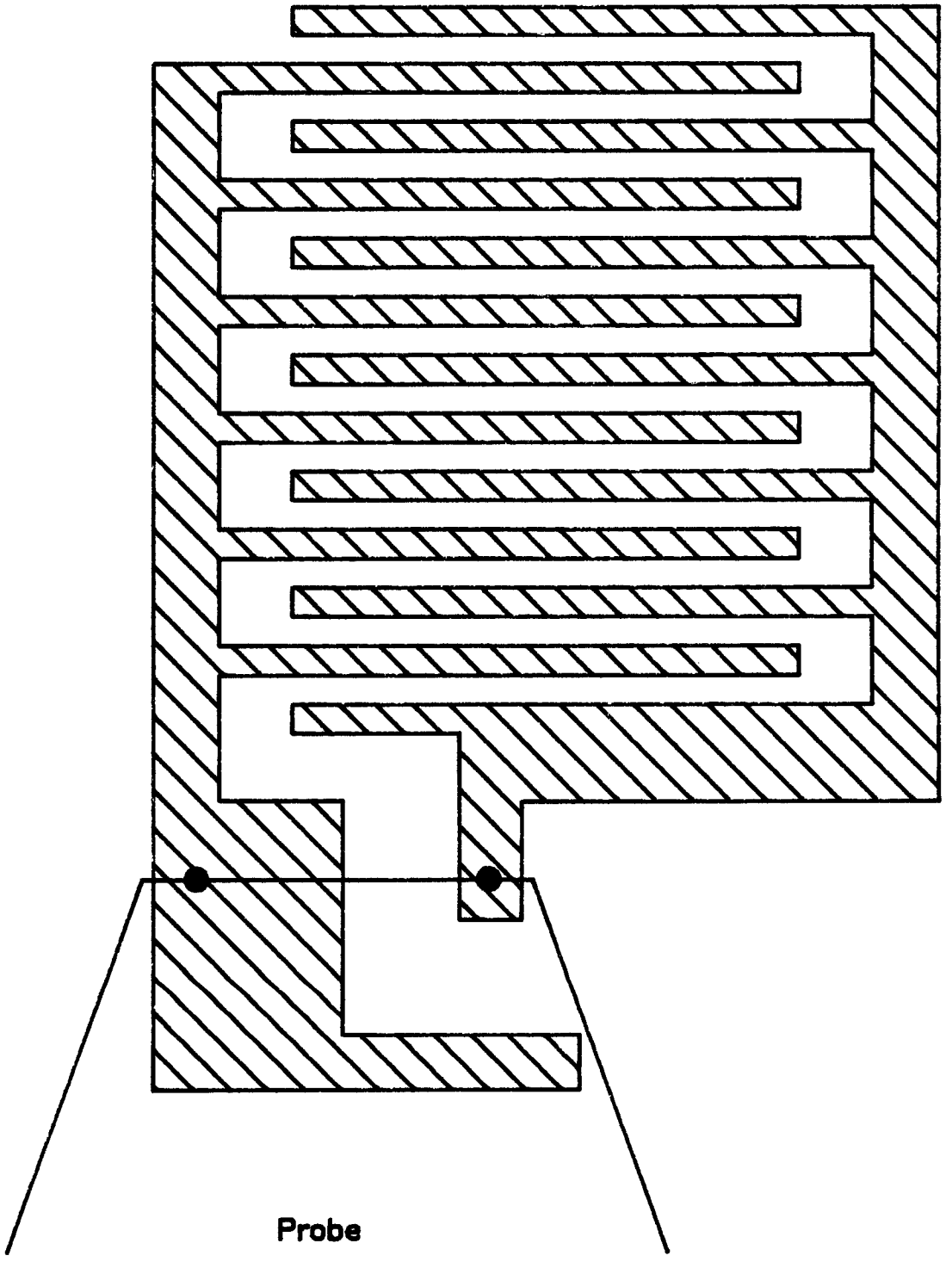

Fig. 3.8 Top view of IDS on alumina and sapphire substrates.

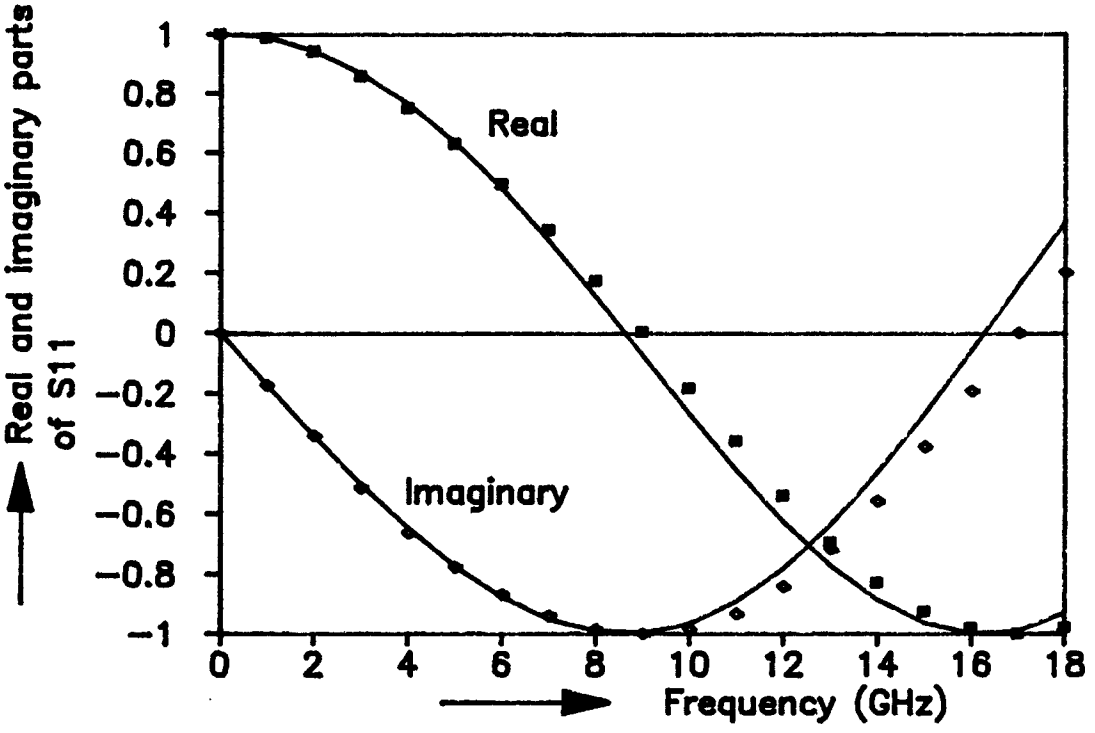

Fig. 3.9 Predicted and measured real and imaginary parts of S11 for the IDS on alumina substrate. (N_f=13, S=W=1 mil, G=2 mil, W_p=4 mil, l=10 mil, h_s =25 mil,ε_r =10.0).

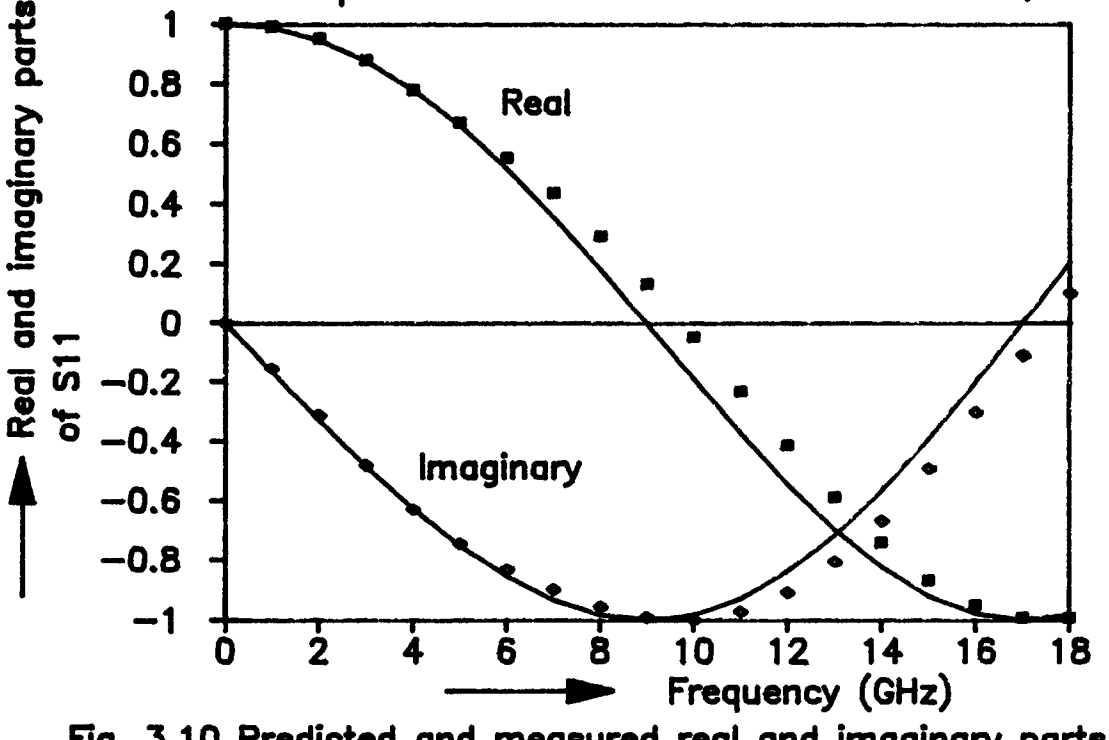

Fig. 3.10 Predicted and measured real and imaginary parts of S11 for the IDS on sapphire substrate. (N_f=13, S=W=1 mil, G=2 mil, W_p=4 mil, l=10 mil, h_s =15 mil,ε_r =9.9).

Table 3.1 Comparison of C and C_1 between the subject model and Pettenpaul model. [Capacitor dimensions: l=100 μ m, W=S=G=10 μ m, h_s=140 μ m, W_p=10 μ m, ε_r =12.9] (1: The subject model and 2: Pettenpaul model [77]).

Frequency (GHz)	N_f=5				N_f=10				N_f=20			
	C (fF)		C_1 (fF)		C (fF)		C_1 (fF)		C (fF)		C_1 (fF)	
	1	2	1	2	1	2	1	2	1	2	1	2
0	36.5	36	19.0	18	80.1	79	35.7	21	166	165	69.3	27
3	36.5	36	19.0	18	80.2	79	35.8	21	168	166	69.5	27
6	36.6	36	19.0	18	80.3	80	35.9	21	170	167	69.7	27
9	36.6	36	19.1	18	80.7	80	36.0	22	173	170	70.1	28
12	36.7	36	19.1	18	81.2	81	36.1	22	179	173	70.7	28
15	36.8	37	19.1	19	82.0	82	36.2	22	186	177	71.3	28
18	36.8	37	19.2	19	82.9	83	36.3	22	196	183	72.2	29

C_1 given in [77] are all smaller except for N_f=5.

In Fig. 3.11, the measured and the calculated insertion losses from the model are plotted as a function of frequency for three interdigitated structures. The measurements were made on a 12" by 12" by 1/2" slab of stycast material which has a relative dielectric constant of 12.5 and is very close to the relative dielectric constant of GaAs which is 12.9. This material was successfully used to test scaled models. If we scale the dimensions down then the frequency would be well into the GHz region. As can be seen form the Fig. 3-11 the general trend is followed in all three cases. The error varies from less than half a dB to 2 dB at higher frequencies. Factors that could account for this error are i) the accuracy to which the IDS pattern could be made by hand with one mil (1 mil = 25.4 μm) thick copper foil, ii) the human error in reading the values off the spectrum analyzer display, iii) the questionable validity of the equivalent circuit models at scaled dimensions and, iv) the error in the model itself.

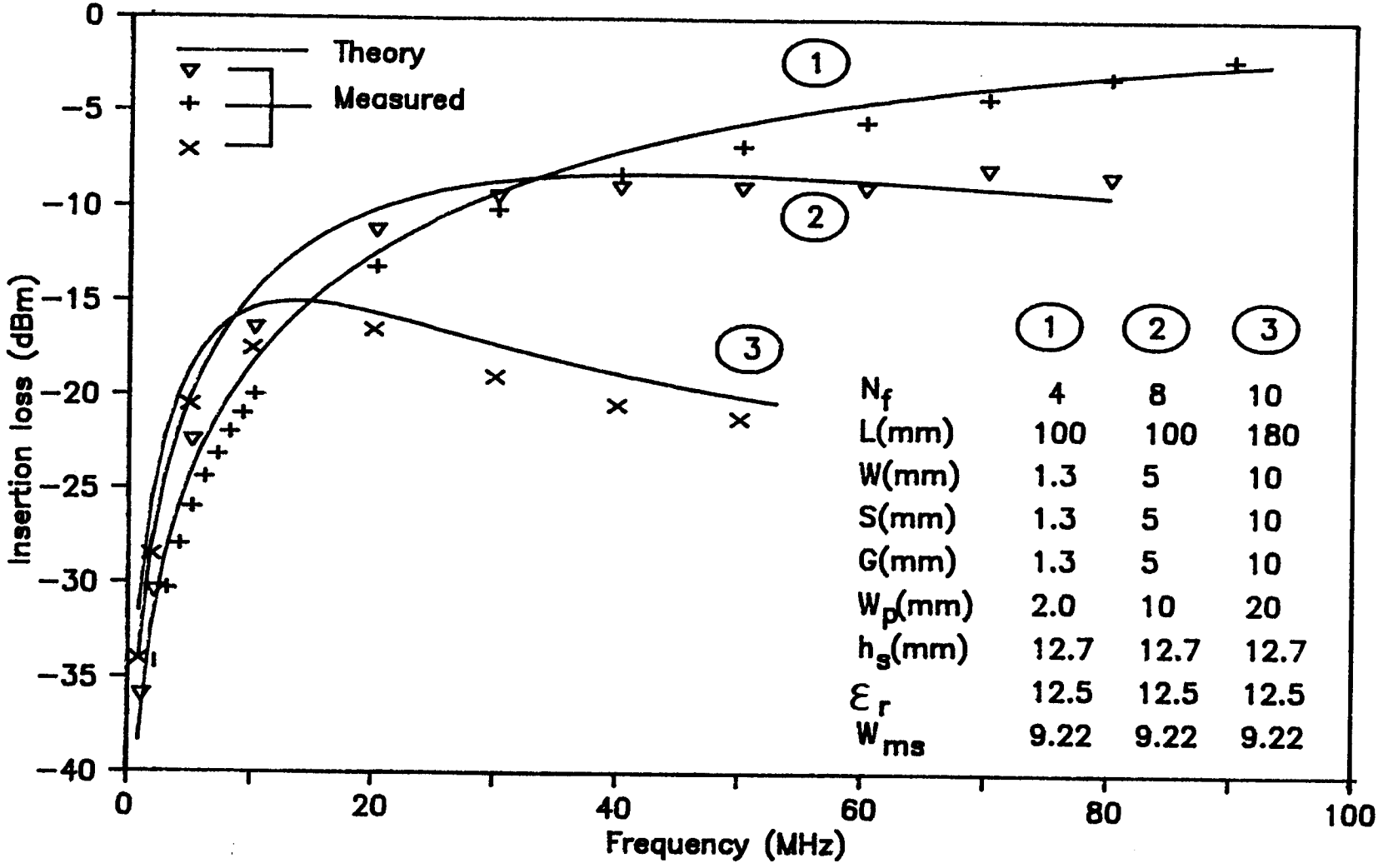

Fig. 3.11 Plot of insertion loss for three interdigitated structures.

4. IMPULSE RESPONSE SIMULATION OF MSM PHOTODETECTORS

4.1 Introduction

Solid state device models can be divided into two categories: physical device models and equivalent circuit models. Equivalent circuit models are based on the electrical performance of the device and are easier to implement. However these models are limited in their range of application because it is often difficult to accurately relate the model elements to the physical parameters of the device (geometry, doping, etc.) and because of the bias, frequency dependence and non-linear dependence of most semiconductor devices [83].

Physical device models are based on the physics of carrier transport and can provide greater insight into the detailed operation of the device. These are not limited by the operating conditions and have been successfully used to analyze dc, transient, large-signal and high frequency operation. These models are used to predict the characteristics of devices within the constraints of the information available with respect to the semiconductor material properties [83-85].

Physical device models are solved using one of either bulk carrier transport equations, Boltzmann transport models, or quantum transport concepts. Boltzmann and quantum transport models are generally restricted to sub-micron devices to provide detailed insight into carrier transport physics. The transport equations based on the first two moments of the Boltzmann transport equation, which assume equilibrium transport conditions, satisfy most modeling requirements [83].

Previous work in this area has mainly concentrated on

modeling photodetectors made on epi-layers. Wei et al. [31] reported a 1-D simulation of a planar photoconductor fabricated on a GaAs epi-layer, neglecting transverse diffusion and trapping effects. Their model successfully predicted the light-triggered Gunn oscillations which were experimentally observed. Van Zeghbroeck et al. [46] and Koscielniak et al. [47,48] modeled the GaAs epi-layer MSM photodetectors with interdigital finger spacings in the sub-micron range. Peterson [86] has modeled the MSM photodetector made on epi layers of silicon.

Iversion and Smith [87] have modeled the response of InP:Fe photoconductors taking electron and hole trapping effects into the deep level Fe impurities into account. Kolodny and Kidron [88] have modeled the intrinsic photoconductive response of HgCdTe infrared detectors. A few analytical models [1,32,64] can also be found in the literature.

In this chapter the physical modeling of the SI-GaAS interdigitated MSM photodetector is described. The model predicts the impulse response using bulk carrier transport equations for the given structure, material parameters, and operating conditions. The model considers both carriers, electrons and holes, and includes the effects of field dependent mobilities, carrier diffusion, and recombination. The influence of the parasitic circuit elements calculated in chapter 3 is also included. Dynamic simulation is performed after applying an ideal light impulse. Carrier distributions and currents, with and without the influence of external circuit, are calculated as a function of time.

4.2 Physical description

The distribution and motion of carriers within a

semiconductor device structure can be obtained by solving three basic equations: 1) Poisson's equation, 2) the continuity equation for electrons, and 3) the continuity equation for holes [2]. Poisson's equation describes the relationship between electric potential and space charge and is given as

$$\nabla^2\psi = - q \ (p - n + N_D^+ - N_A^- + N_{DD}^+)/\varepsilon \qquad (4.1)$$

where ψ is the potential, n and p are free electron and hole densities, respectively, N_D^+ and N_A^- are ionized shallow donor and acceptor densities, respectively, and N_{DD}^+ is the ionized deep donor (EL_2 defect) density. For the case of EL_2 doped SI-GaAs based on a three-level model [89],

$$N_D^+ + N_{DD}^+ \cong N_A^- . \qquad (4.2)$$

The free electron and hole densities, n and p, are close to the intrinsic carrier density, n_i, which is ~ 2×10^6 cm^{-3}. Commercially sold EL_2-doped SI-GaAs substrates are slightly n-type [90]. Through out the simulation, $n = p = n_i$ and $N_D^+ + N_{DD}^+ = N_A^-$ are assumed under thermal equilibrium conditions. Under these assumptions the Fermi level is at the intrinsic level which when referenced to the conduction band energy level, is given by,

$$E_c - E_i = E_g/2 \ + (k_BT/2) \ \log_e(N_c/N_v) \qquad (4.3)$$

where E_g is the bandgap and N_c, N_v are the conduction band and valence band densities of states, respectively. The value of $E_c - E_i$ is $\approx$ 0.68 ev.

The Fermi level at the air-GaAs interface is usually pinned at 0.8 ev below the conduction band minimum [91]. This would cause a depletion depth of < 0.1 μm at the

interface. This width is much smaller than the simulation depth of the structure (2.5 μm). Its effects are negligible on the operation of the device, so it is not included in the simulation. A similar situation arises at the Schottky contacts where the Schottky barrier height for some Schottky metals is even smaller than 0.8 ev (eg., $\Phi_{Bn}(WSi_x)$ = 0.74 ev, [44]). The effects of this depletion width are also neglected in the simulation. In effect SI-GaAs is assumed to be a perfect insulator with $n = p = n_i$ and with no band bending at the interfaces under thermal equilibrium. Under these assumptions the right hand side of equation (4.1) becomes zero and the band diagram is as shown in Fig. 4.1. Equation (4.1) with a zero right hand side is Laplace's equation,

$$\nabla^2\psi = 0. \tag{4.4}$$

The flow of charged particles is governed by the two continuity equations, which are given as

$$\frac{\partial n}{\partial t} = \frac{1}{q} \nabla.J_n + G_n - R_n \tag{4.5}$$

$$\frac{\partial p}{\partial t} = - \frac{1}{q} \nabla.J_p + G_p - R_p \tag{4.6}$$

where G_n, G_p and R_n, R_p are the net generation rates and net recombination rates for electrons and holes, respectively. J_n and J_p are the current densities for electrons and holes, respectively, and are given by, based on the first two moments of the Boltzmann transport equation [83],

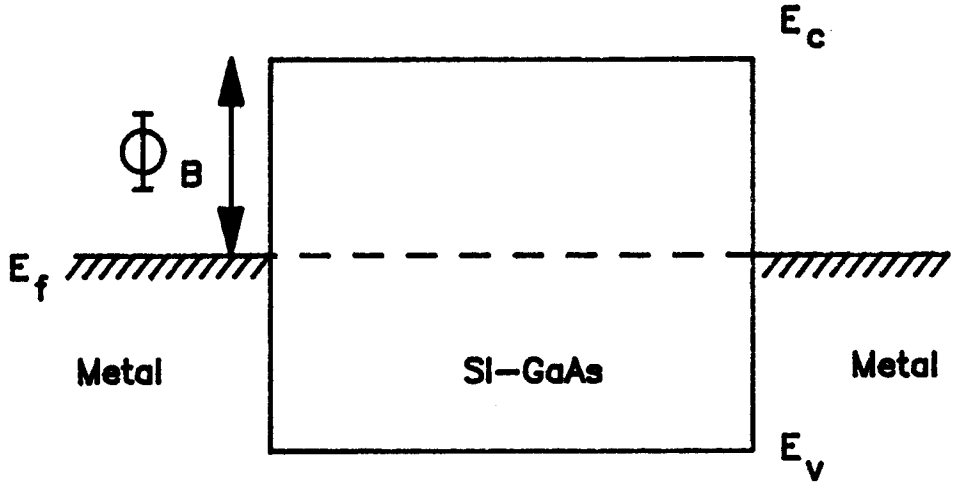

(a)

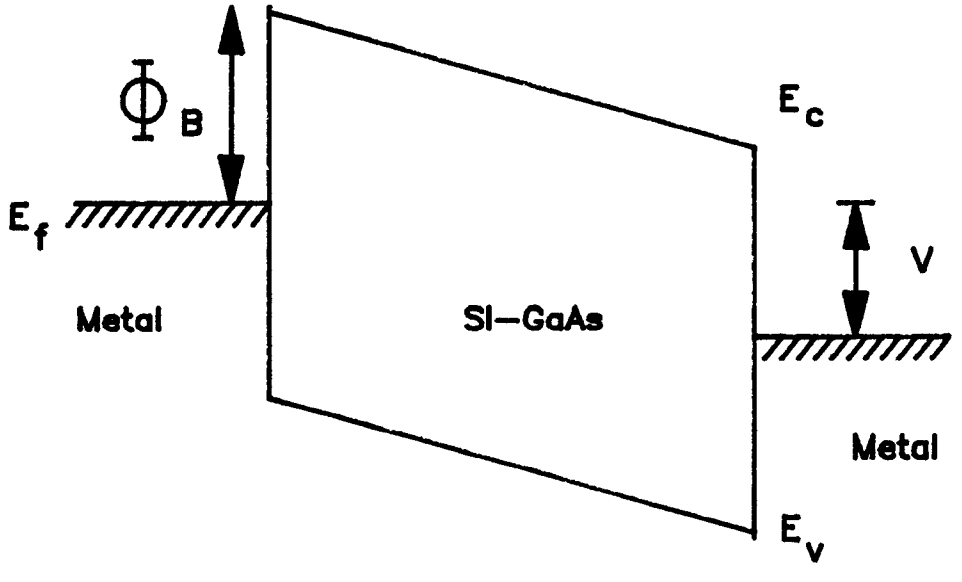

(b)

Fig. 4.1 Band diagram of SI—GaAs MSM structure: (a) with no bias, and (b) with bias.

$$J_n = qn\mu_n E + qD_n \nabla n \tag{4.7}$$

$$J_p = qp\mu_p E - qD_p \nabla p \tag{4.8}$$

where E is the electric field, μ_n, μ_p and D_n, D_p are the moblities and diffusion constants of electrons and holes respectively. The electric field is related to the potential via the relation

$$E = - \nabla\psi. \tag{4.9}$$

The Einstein relationship is assumed to hold between diffusion constants and mobilities. This is

$$D_n = (k_B T/q)\ \mu_n \tag{4.10}$$

$$D_p = (k_B T/q)\ \mu_p \tag{4.11}$$

The optical generation rates G_n and G_p in equations (4.2) and (4.3) will be zero for $t > 0^+$ and the optical impulse establishes initial carrier densities which are given by [1]

$$n(t = 0^+) = p(t = 0^+) = \frac{(1-R_{surf})\alpha\xi(x,y)e^{(-\alpha y)}}{h_p\nu} \tag{4.12}$$

where R_{surf} is the reflectivity of the detector surface, α is the absorption coefficient, ξ is the incident optical pulse energy per unit area and $h_p\nu$ is the energy of one photon. Although n = p initially, their time evolution will differ due to different mobilities and recombination rates.

The most funadamental recombination process is the Shockley-Read-Hall (SRH) type which is written, in the case of a single energy-level recombination center (which characterizes defects with neutral and single charge

states), as [31]

$$R = R_n = R_p = \frac{np - n_i^2}{\tau_p(n+n_t) + \tau_n(p+p_t)} . \quad (4.13)$$

Here n_t, p_t are computable constants given by

$$n_t = n_i \exp\left(\frac{E_t - E_i}{k_B T}\right) \quad (4.14)$$

$$p_t = n_i \exp\left(\frac{E_i - E_t}{k_B T}\right) \quad (4.15)$$

where E_t is the trap energy level, E_i is the intrinsic Fermi level, and τ_p, τ_n are the electron and hole lifetimes. For simplicity $E_t = E_i$ and $\tau_p = \tau_n = \tau$ are assumed. With these assumptions, the recombination rate is given by

$$R = \frac{np - n_i^2}{\tau(n + p + 2n_i)} . \quad (4.16)$$

The existence of τ in equation (4.16) is an assumption consistent with the given thermal equilibrium states. As pointed by Yu et al., [92] it is not clear that, under sufficiently high electric field, recombination should take place at all. They point that the recombination process should be strongly electric field dependent and a certain finite field exists beyond which recombination time should be considered infinite. Lacking the data on $\tau(E)$ in the literature, and assuming that the device is operated in a regime where the effect of recombination is small on the response, τ is taken as the thermal equilibrium value.

Two other recombination terms are Auger recombination

and radiative recombination which become significant only at carrier densities of $\geq 1 \times 10^{17}$ cm^{-3} [93]. In photodetectors, even at high illumination levels, the carrier densities rarely reach these high levels, so only recombination through midgap states is considered.

The capture time for a deep level electron trap is given by

$$\tau_c = \frac{1}{\sigma_c v_{th} n} \tag{4.17}$$

where σ_c is the capture cross section and v_{th} is the thermal velocity of the electron. The capture time of an EL_2 trap is $\approx 1 \times 10^{-8}$ sec for an electron free carrier concentration of 1×10^{14} cm^{-3}, v_{th} of 1×10^{7} $cm.sec^{-1}$ and σ_c of 1×10^{-13} cm^{-2} [94-95]. But all the photoexcited carriers are collected at the contacts in a much shorter time than the deep level capture time. So the effects of trapping are neglected assuming very few carriers are trapped during the response time of the detector. Carrier densities exceed 1×10^{14} cm^{-3} level only at high excitation levels.

The thermal emission time for a deep level electron trap is given by

$$\tau_e = \frac{1}{\sigma_e v_{th} N_c} \exp\left(\frac{E_c - E_t}{k_B T}\right) \tag{4.18}$$

where E_t is the trap energy level. For the EL_2 trap, which is approximately 0.69 ev below the conduction band minimum, the emission time is tens of milliseconds. So whatever few electrons are captured, their emission time at room temperature occurs at a much slower rate and is not

important on the time scales considered in the simulation [87].

4.3 Mobility models

The electron and hole mobilities at low electric fields are constant and independent of the field. But at high electric fields the mobilities are a function of the field. The shape of the drift velocity verses electric field curve is closely related to the value of the low-field mobility [96]. The typical low field mobility of electrons in SI GaAs is 5000 $cm^2.v^{-1}.sec^{-1}$ [90]. The expression for drift velocity verses electric field for electrons is taken from [96] and is given by

$$v_n(\mu_n,E) = v_{nsat} \left\{ 1 + \frac{E\mu_n/v_{nsat} - 1}{1 + B_1(E\mu_n/v_{nsat})^Q} \right\} \qquad (4.19)$$

where

$$B_1 = 0.6\ [e^{10(\mu_n-0.2)} + e^{-35(\mu_n-0.2)}]^{-1} + 0.01, \qquad (4.20)$$

$$Q = 4\ \left[1 + \frac{320}{\sinh\ (40\ \mu_n)}\right], \qquad (4.21)$$

$$v_{nsat} = [0.6\ (1 + \mu_n) - 0.2\ \mu_n^2] \times 10^5\ m.sec^{-1}. \qquad (4.22)$$

In equations (4.19-21) mobility is in $m^2.v^{-1}.sec^{-1}$, electric field is in $v.m^{-1}$, and velocity is in $m.sec^{-1}$.

Darling [32] and Snowden [83] have used the following relationship between low field mobility and electric field for holes.

$$v_p\ (\mu_p, E) = \frac{\mu_p E}{1 + E\mu_p / v_{psat}} \qquad (4.23)$$

Bowers et al. [11] and Hellwege [97] have used a different relation. Ths saturation velocity for the hole was given as: 0.85×10^7 cm.sec^{-1} by Darling [32], 1.5×10^7 cm.sec^{-1} by Snowden [83], 0.6×10^7 cm.sec^{-1} by Bowres et al. [11] and 1.0×10^7 cm.sec^{-1} by Hellwege [97]. A low field mobility of 350 cm^2.v^{-1}.sec^{-1} is assumed for the hole. Fig. 4.2a shows the plot of electron drift velocity as a function of electric field calculated from equation (4.19). Fig. 4.2b shows the plot of hole drift velocity verses electric field.

4.4 Domain and boundary conditions

A finite domain which contains physical and artificial boundaries should be specified for simulation. The domain chosen for the photodetector simulation is shown in Fig. 4.3. The interfaces between the passivating layer-SI- GaAs and the metal contacts-SI-GaAs are the physical boundaries whereas the dashed lines show the artificial boundaries.

The artificial boundaries I and II are chosen through the middle of the fingers so that reflecting (Neumann) boundary conditions (carrier flux and electric field are zero across the interface) can be imposed. The choice of artificial boundary III is somewhat arbitrary. It is chosen at a depth of 2.5 μm from the surface. The absorption length, which is the inverse of the absorption coefficient, is ≈ 1 μm in GaAs at a wavelength of 0.8 μm. About 92 % of the photons are absorbed in the chosen depth of 2.5 μm. Neumann boundary conditions are also imposed at this boundary.

Fixed (Dirichlet) boundary conditions (carrier

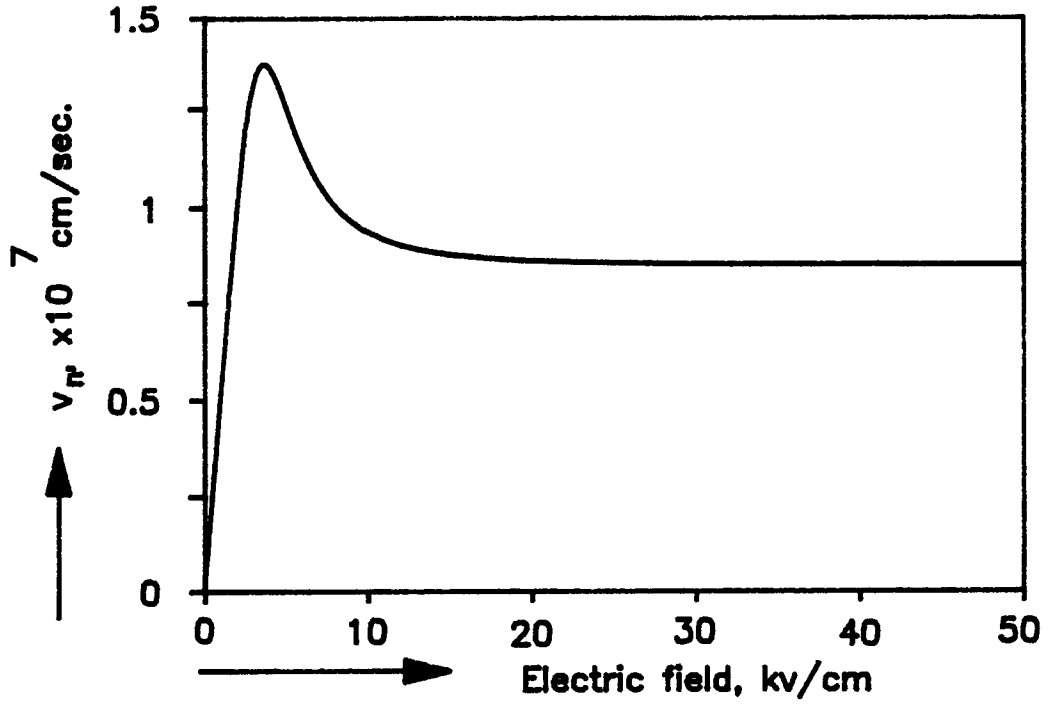

(a)

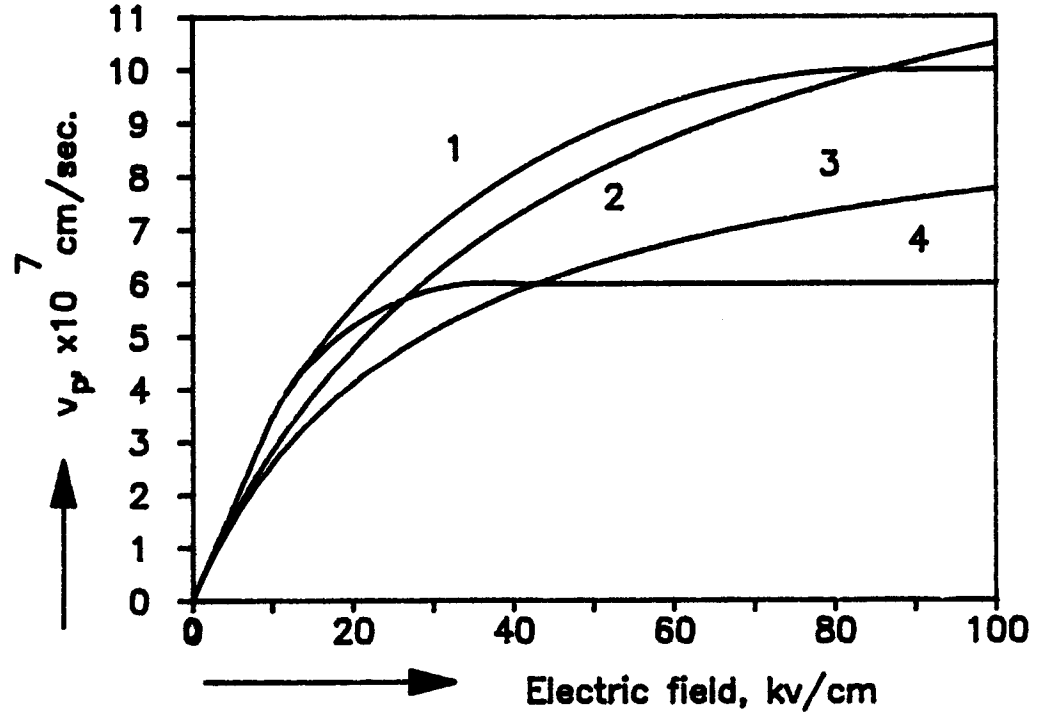

(b)

Fig. 4.2 Plot of drift velocity verses electric field. a) Electron drift velocity. b) Hole drift velocity.

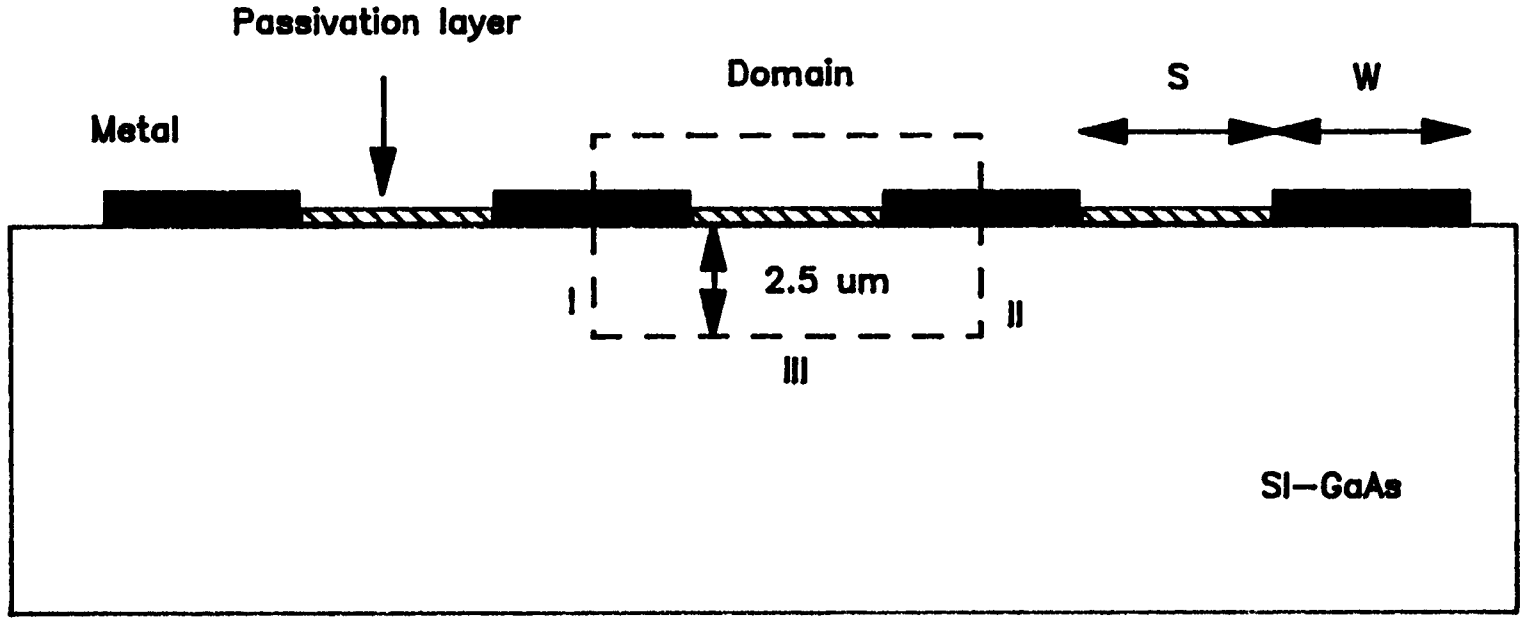

Fig. 4.3 Simulation domain.

concentrations and electric potential are known at the boundary) are imposed at the metal contacts since no space charge is assumed at these contacts. Gauss's law should be applied at the interface between the passivating layer and the SI GaAs. For an air-semiconductor interface, Peterson [86] has shown that the potential distribution, as well as the carrier distributions, are qualitatively unaltered by replacing air with semiconductor. This would be even a better approximation when a passivating layer replaces air. So Neumann boundary conditions are imposed as a result of symmetry. The surface recombination is neglected because of the passivating layer which reduces the surface recombination to insignificant levels.

The Neumann boundary conditions at the artificial boundaries and at the passivating layer-semiconductor interface are expressed as

$$a_n . \nabla \psi = 0 \tag{4.24}$$

$$a_n . \nabla n = 0 \tag{4.25}$$

$$a_n . \nabla p = 0 \tag{4.26}$$

where a_n is a unit normal perpendicular to the interface. The Dirichlet boundary conditions at the contacts are expressed as

$$n = n_i \tag{4.27}$$

$$p = n_i \tag{4.28}$$

$$\psi = \text{constant} \tag{4.29}$$

where $\psi = 0$ on one contact and $\psi = V$, the applied voltage, on the other contact.

4.5 Scaling

The current relations (4.6) and (4.7) are substituted into the continuity equations (4.5) and (4.6). These together with Laplace's equation (4.4), constitute a system of partial differential equations with the dependent variables ψ, n, and p.

$$\nabla^2\psi = 0 \tag{4.30}$$

$$\frac{\partial n}{\partial t} = \nabla.(n\mu_n E + D_n \nabla n) - R \tag{4.31}$$

$$\frac{\partial p}{\partial t} = -\nabla.(p\mu_p E + D_p \nabla p) - R \tag{4.32}$$

The dependent variables ψ, n, and p in the basic equations are scaled so as to reduce their range. The scaling factors employed are taken from [85] with some modifications and are given in table 4.1. After scaling, the basic equations transform into:

$$\nabla^2\psi = 0 \tag{4.33}$$

$$J_n = n\mu_n \nabla\psi - D_n \nabla n \tag{4.34}$$

$$J_p = p\mu_p \nabla\psi + D_p \nabla p \tag{4.35}$$

$$\frac{\partial n}{\partial t} = \nabla.(D_n \nabla n - n\mu_n \nabla\psi) - R \tag{4.36}$$

$$\frac{\partial p}{\partial t} = \nabla.(D_p \nabla p + p\mu_p \nabla\psi) - R \tag{4.37}$$

The scaled current relations are multiplied by $-x_0/qD_0n_i$. Boundary conditions and initial conditions are also scaled according to the scaling factors shown in Table 4.1.

Table 4.1 Scaling factors

Quantity	Symbol	Value
x,y	X_0	min(X,Y)
ψ	ψ_0	V
n,p	n_i	n_i
μ_n, μ_p	μ_0	$\max(\mu_n, \mu_p)$
D_n, D_p	D_0	$\mu_0 \psi_0$
R	R_0	$D_0 n_i / X_0^2$
t	t_0	X_0^2 / D_0

4.6 Numerical method

The two most common methods used to solve the partial differential equations are the finite difference method (FDM) and finite element method (FEM). Both methods rely on the discretization of the equations across the domain of the device. The FDM is well suited for planar rectangular geometry devices and is employed here. It produces solutions for the physical variables ψ, n, and p as discretized values at specific nodes contained within a mesh superimposed on the domain. The continuous derivatives are approximated by discretized finite differences. The discretized physical variables are represented by values obtained from the solution of the discretized equations at each mesh point except where the boundary conditions determine the values of the variables [83].

The classical five point discretization shown in Fig. 4.4 is used. The following notation is employed.

$$a_i = \Delta x = x_{i+1} - x_i \qquad i=0,1,\ldots,M-1 \tag{4.38}$$

$$b_i = \Delta y = y_{j+1} - y_j \qquad j=0,1,\ldots,N-1 \tag{4.39}$$

$$f(x_i,y_j) = f_{i,j} \qquad i=0,1,\ldots,M-1;\ j=0,1,\ldots,N-1 \tag{4.40}$$

$$f(x_i+\Delta x,y_j) = f_{i+1,j} \qquad i=0,1,\ldots M-1 \tag{4.41}$$

$$f\left(\frac{x_i+x_{i+1}}{2},y\right) = f_{i+1/2,j} \qquad i=0,1,\ldots,M-1 \tag{4.42}$$

where $x_i(y_i)$ is the distance from the origin to the i^{th} (j^{th}) mesh line parallel to the x-axis(y-axis) and f is a function of x and y. For simplicity a uniform mesh like the one shown in Fig. 4.5 is used with $\Delta x = \Delta y = h$.

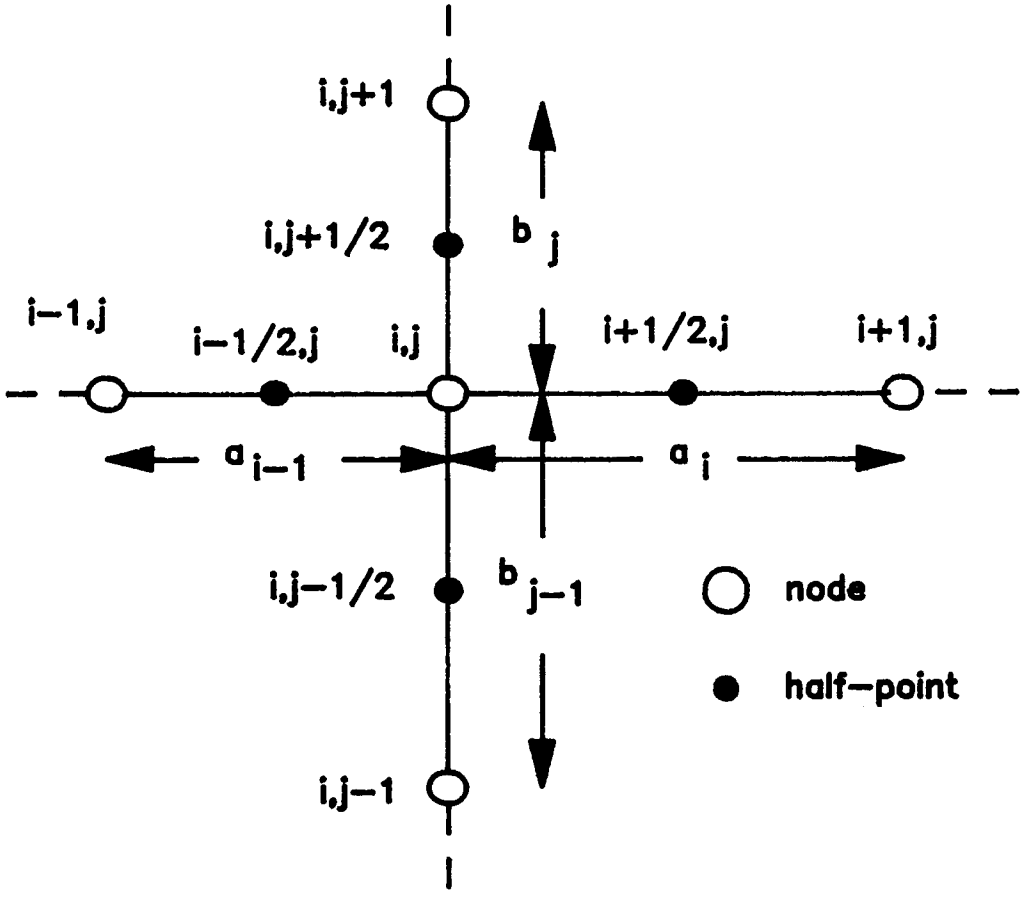

Fig. 4.4 Mesh notation for finite differencing.

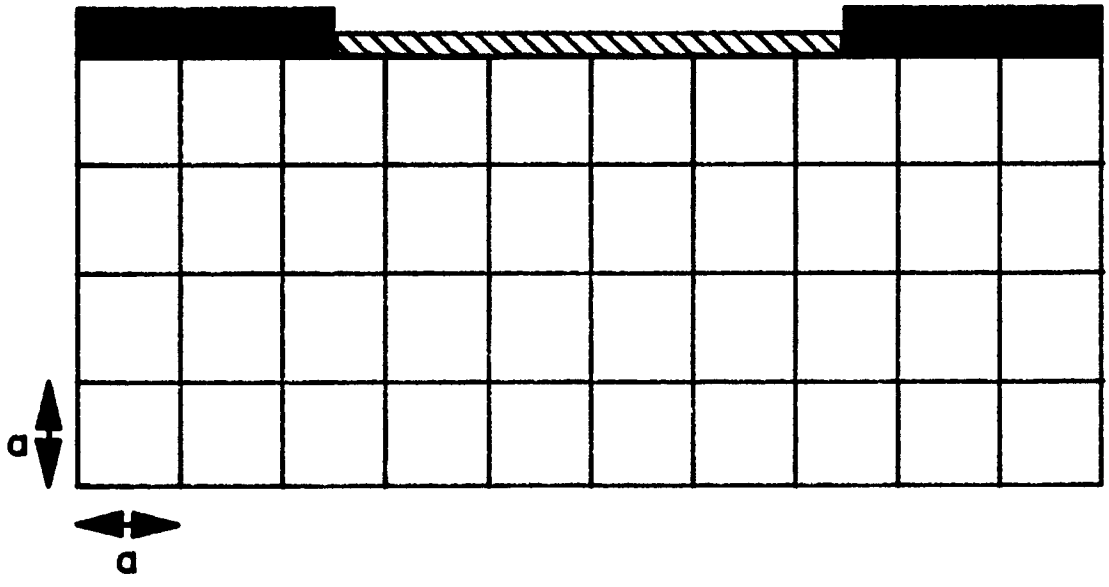

Fig. 4.5 A uniform mesh over the domain.

4.7 Discretization of the semiconductor equations

Central difference approximations are employed for greater accuracy. The discretization of Laplace's equation is simple for a uniform mesh and is given by

$$\frac{\psi_{i-1,j} - 2\psi_{i,j} + \psi_{i+1,j}}{h^2} + \frac{\psi_{i,j-1} - 2\psi_{i,j} + \psi_{i,j+1}}{h^2} = 0 \tag{4.43}$$

which is simplified and is written as

$$\psi_{i-1,j} + \psi_{i,j-1} - 4\psi_{i,j} + \psi_{i,j+1} + \psi_{i+1,j} = 0. \tag{4.44}$$

After applying boundary conditions the discretized Laplace's equation can be expressed in matrix form as

$$[A][\psi] = [B] \tag{4.45}$$

where [A] is the coefficient matrix and matrix [B] contains the Dirichlet boundary potentials. The coefficient matrix has a maximum of five non-zero elements on any row of the matrix and is therefore sparse.

The electric field, E, at any point is computed from the two components E_x and E_y as

$$E = \sqrt{E_x^2 + E_y^2}\ . \tag{4.46}$$

Central difference notation is used to compute E_x and E_y at the half points shown in Fig. 4.4.

$$E_{xi+1/2,j} = -\frac{\partial\psi}{\partial x} = \frac{\psi_{i,j} - \psi_{i+1,j}}{h} \tag{4.47}$$

$$E_{yi,j+1/2} = -\frac{\partial\psi}{\partial y} = \frac{\psi_{i,j} - \psi_{i,j+1}}{h} \tag{4.48}$$

The electric field, E, is used to determine the mobilities and diffusion constants.

The finite difference formulation of the continuity equations is done by a half-point difference expansion based on central difference approximations. The continuity equations for electrons and holes are written as

$$\frac{\partial n}{\partial t} = \nabla.(-J_n) - R = \frac{(-J_{nxi+1/2,j}) - (-J_{nxi-1/2,j})}{h} + \frac{(-J_{nyi,j+1/2}) - (-J_{nyi,j-1/2})}{h} - R(n,p)_{i,j} \quad (4.49)$$

$$\frac{\partial p}{\partial t} = \nabla.J_p - R = \frac{J_{pxi+1/2,j} - J_{pxi-1/2,j}}{h} + \frac{J_{pyi,j+1/2} - J_{pyi,j-1/2}}{h} - R(n,p)_{i,j} . \quad (4.50)$$

Employing the standard difference approximations for the current density expressions leads to numerical instability whenever the voltage change between mesh points exceeds $2k_BT/q$ volts [98]. So J_n and J_p are treated as differential equations in n and p with J_n, J_p, n, p, and E assumed constant between mesh points. The solution of these differential equations then relates J_n and J_p to the other variables [98].

$$J_{nx\ i+1/2,j} = \frac{D_{n\ i+1/2,j}}{h}\left[n_{i,j}B\left(\frac{\psi_{i,j}-\psi_{i+1,j}}{\theta}\right) - n_{i+1,j}B\left(\frac{\psi_{i+1,j}-\psi_{i,j}}{\theta}\right)\right] \quad (4.51)$$

$$J_{nx\ i-1/2,j} = -\frac{D_{n\ i-1/2,j}}{h}\left[n_{i,j}B\left(\frac{\psi_{i,j}-\psi_{i-1,j}}{\theta}\right) - n_{i-1,j}B\left(\frac{\psi_{i-1,j}-\psi_{i,j}}{\theta}\right)\right] \quad (4.52)$$

$$J_{ny\ i,j+1/2} = \frac{D_{n\ i,j+1/2}}{h}\left[n_{i,j}B\left(\frac{\psi_{i,j}-\psi_{i,j+1}}{\theta}\right) - n_{i,j+1}B\left(\frac{\psi_{i,j+1}-\psi_{i,j}}{\theta}\right)\right] \quad (4.53)$$

$$J_{ny\ i,j-1/2} = -\frac{D_{n\ i,j-1/2}}{h}\left[n_{i,j}B\left(\frac{\psi_{i,j}-\psi_{i,j-1}}{\theta}\right) - n_{i,j-1}B\left(\frac{\psi_{i,j-1}-\psi_{i,j}}{\theta}\right)\right] \quad (4.54)$$

$$J_{px\ i+1/2,j} = \frac{D_{p\ i+1/2,j}}{h}\left[p_{i+1,j}B\left(\frac{\psi_{i,j}-\psi_{i+1,j}}{\theta}\right) - p_{i,j}B\left(\frac{\psi_{i+1,j}}{\theta}\right)\right]\psi_{i,j} \quad (4.55)$$

$$J_{px\ i-1/2,j} = -\frac{D_{p\ i-1/2,j}}{h}\left[p_{i-1,j}B\left(\frac{\psi_{i,j}-\psi_{i-1,j}}{\theta}\right) - p_{i,j}B\left(\frac{\psi_{i-1,j}-\psi_{i,j}}{\theta}\right)\right] \quad (4.56)$$

$$J_{py\ i,j+1/2} = \frac{D_{p\ i,j+1/2}}{h}\left[p_{i,j+1}B\left(\frac{\psi_{i,j}-\psi_{i,j+1}}{\theta}\right) - n_{i,j}B\left(\frac{\psi_{i,j+1}-\psi_{i,j}}{\theta}\right)\right] \quad (4.57)$$

$$J_{py\ i,j-1/2} = -\frac{D_{p\ i,j-1/2}}{h}\left[p_{i,j-1}B\left(\frac{\psi_{i,j}-\psi_{i,j+1}}{\theta}\right) - n_{i,j}B\left(\frac{\psi_{i,j-1}-\psi_{i,j}}{\theta}\right)\right] \quad (4.58)$$

where B(z) is the Bernoulli function which is defined as

$$B(z) = \frac{z}{e^z - 1} \tag{4.59}$$

and θ is defined as

$$\theta = k_B T/q \tag{4.60}$$

The Bernoulli function is implemented as [85]

$$B(z) = \begin{cases} -z & z \leq z1 \\ z/[\exp(z)-1] & z1 < z < z2 \\ 1-z/2 & z2 \leq z \leq z3 \\ z\ \exp(-z)/[1-\exp(-z)] & z3 < z < z4 \\ z\ \exp(-z) & z4 \leq z < z5 \\ 0 & z5 \leq z \end{cases} \tag{4.61}$$

The constants z1 to z5 depend on the individual computer hardware and are defined as [85]

$$\exp(z1)-1 = -1 \tag{4.62}$$

$$z2/[\exp(z2)-1] = 1-z2/2 \qquad z2<0 \tag{4.63}$$

$$1-z3/2 = z3\ \exp(-z3)/[1-\exp(z3)] \qquad z3>0 \tag{4.64}$$

$$1-\exp(z4) = 1 \tag{4.65}$$

$$\exp(-z5) = 0 \tag{4.66}$$

These equations provide numerically stable estimates of the current density under all bias conditions. Substituting equations (4.47-4.54)) in equations (4.45) and (4.46), the discrete forms of the continuity equations for electrons and holes are obtained.

The space discretization has been tackled so far. The full backward time differencing (backward Euler method) is unconditionally stable for any time step t and is used in the simulation. The following notation is used.

$$\Delta t = t_{k+1} - t_k \qquad k=0,1,2,\ldots,L_T-1 \tag{4.67}$$

$$f(x_i,y_j,t_k) = f_{i,j,k} \tag{4,68}$$

The discretized equations are given as

$$\nabla^2\psi = 0 \tag{4.69}$$

$$\frac{n_{i,j,k+1} - n_{i,j,k}}{\Delta t} = \nabla.(-J_{ni,j,k+1}) - R_{i,j,k} \tag{4.70}$$

$$\frac{p_{i,j,k+1} - p_{i,j,k}}{\Delta t} = \nabla.J_{pi,j,k+1} - R_{i,j,k} \tag{4.71}$$

The expressions for carrier mobilities and recombination rate at time k can be used when the solution at time (k+1) is sought. This is because the time scales associated with carrier mobilities and recombination are much larger than the time steps required to obtain acceptable truncation error. The completely discretized continuity equations are given below.

$$n_{i,j-1,k+1} D_{n\ i,j-1/2,k} B\left(\frac{\psi_{i,j-1,k+1} - \psi_{i,j,k+1}}{\theta}\right) +$$

$$n_{i-1,j,k+1} D_{n\ i-1/2,j,k} B\left(\frac{\psi_{i-1,j,k+1} - \psi_{i,j,k+1}}{\theta}\right) -$$

$$n_{i,j,k+1} \left[D_{n\ i,j-1/2,k} B\left(\frac{\psi_{i,j,k+1} - \psi_{i,j-1,k+1}}{\theta}\right) + \right.$$

$$\left. D_{n\ i-1/2,j,k} B\left(\frac{\psi_{i,j,k+1} - \psi_{i-1,j,k+1}}{\theta}\right) + \right.$$

$$D_{n\ i+1/2,j,k}B\left(\frac{\psi_{i,j,k+1}-\psi_{i+1,j,k+1}}{\theta}\right) +$$

$$D_{n\ i,j+1/2,k}B\left(\frac{\psi_{i,j,k+1}-\psi_{i,j+1,k+1}}{\theta}\right) + \frac{h^2}{\Delta t}\Big] +$$

$$n_{i+1,j,k+1}D_{n\ i+1/2,j,k}B\left(\frac{\psi_{i+1,j,k+1}-\psi_{i,j,k+1}}{\theta}\right) +$$

$$n_{i,j+1,k+1}D_{n\ i,j+1/2,k}B\left(\frac{\psi_{i,j+1,k+1}-\psi_{i,j,k+1}}{\theta}\right)$$

$$= \left(R_{i,j,k} - \frac{n_{i,j,k}}{\Delta t}\right) h^2 \qquad (4.72)$$

$$p_{i,j-1,k+1}D_{p\ i,j-1/2,k}B\left(\frac{\psi_{i,j,k+1}-\psi_{i,j-1,k+1}}{\theta}\right) +$$

$$p_{i-1,j,k+1}D_{p\ i-1/2,j,k}B\left(\frac{\psi_{i,j,k+1}-\psi_{i-1,j,k+1}}{\theta}\right) -$$

$$p_{i,j,k+1}\Big[D_{p\ i,j-1/2,k}B\left(\frac{\psi_{i,j-1,k+1}-\psi_{i,j,k+1}}{\theta}\right) +$$

$$D_{p\ i-1/2,j,k}B\left(\frac{\psi_{i-1,j,k+1}-\psi_{i,j,k+1}}{\theta}\right) +$$

$$D_{p\ i+1/2,j,k}B\left(\frac{\psi_{i+1,j,k+1}-\psi_{i,j,k+1}}{\theta}\right) +$$

$$D_{p\ i,j+1/2,k}B\left(\frac{\psi_{i,j+1,k+1}-\psi_{i,j,k+1}}{\theta}\right) + \frac{h^2}{\Delta t}\Big]$$

$$p_{i+1,j,k+1}D_{p\ i+1/2,j,k}B\left(\frac{\psi_{i,j,k+1}-\psi_{i+1,j,k+1}}{\theta}\right) +$$

$$p_{i,j+1,k+1}D_{p\ i,j+1/2,k}B\left(\frac{\psi_{i,j,k+1}-\psi_{i,j+1,k+1}}{\theta}\right)$$

$$= \left(R_{i,j,k} - \frac{p_{i,j,k}}{\Delta t}\right) h^2 \qquad (4.73)$$

Finally the discretization of the boundary conditions needs to be carried out. The discretization of the boundary conditions at the contact is straight forward since Dirichlet boundary conditions are enforced. Neumann boundary conditions must be enforced at all the remaining boundaries. This is done using Stirling polynomials which require extra mirror image nodes outside of the domain as shown in Fig. 4.6. The Stirling derivative approximation for a surface parallel to the x-axis is

$$\frac{\partial f_{i,0}}{\partial y} = \frac{f_{i,1} - f_{i,-1}}{2\Delta y} \tag{4.74}$$

This derivative is zero at the interface and the boundary conditions are

$$\frac{\partial \psi}{\partial y}\Big|_{i,j+1/2} = - \frac{\partial \psi}{\partial y}\Big|_{i,j-1/2} \tag{4.75}$$

$$\frac{\partial n}{\partial y}\Big|_{i,j+1/2} = - \frac{\partial n}{\partial y}\Big|_{i,j-1/2} \tag{4.76}$$

$$\frac{\partial p}{\partial y}\Big|_{i,j+1/2} = - \frac{\partial p}{\partial y}\Big|_{i,j-1/2} \tag{4.77}$$

which would give $\psi_{i,j+1} = \psi_{i,j-1}$, $n_{i,j+1} = n_{i,j-1}$ and $p_{i,j+1} = p_{i,j-1}$. The initial conditions are also discretized at the grid points using equation (4.12) by substituting the values of x and y at the grid points.

4.8 Solution methods

The two methods that are widely used are the Gummel method and the Newton method. Newton's method is quadratic, i.e., the error is approximately squared at each iteration

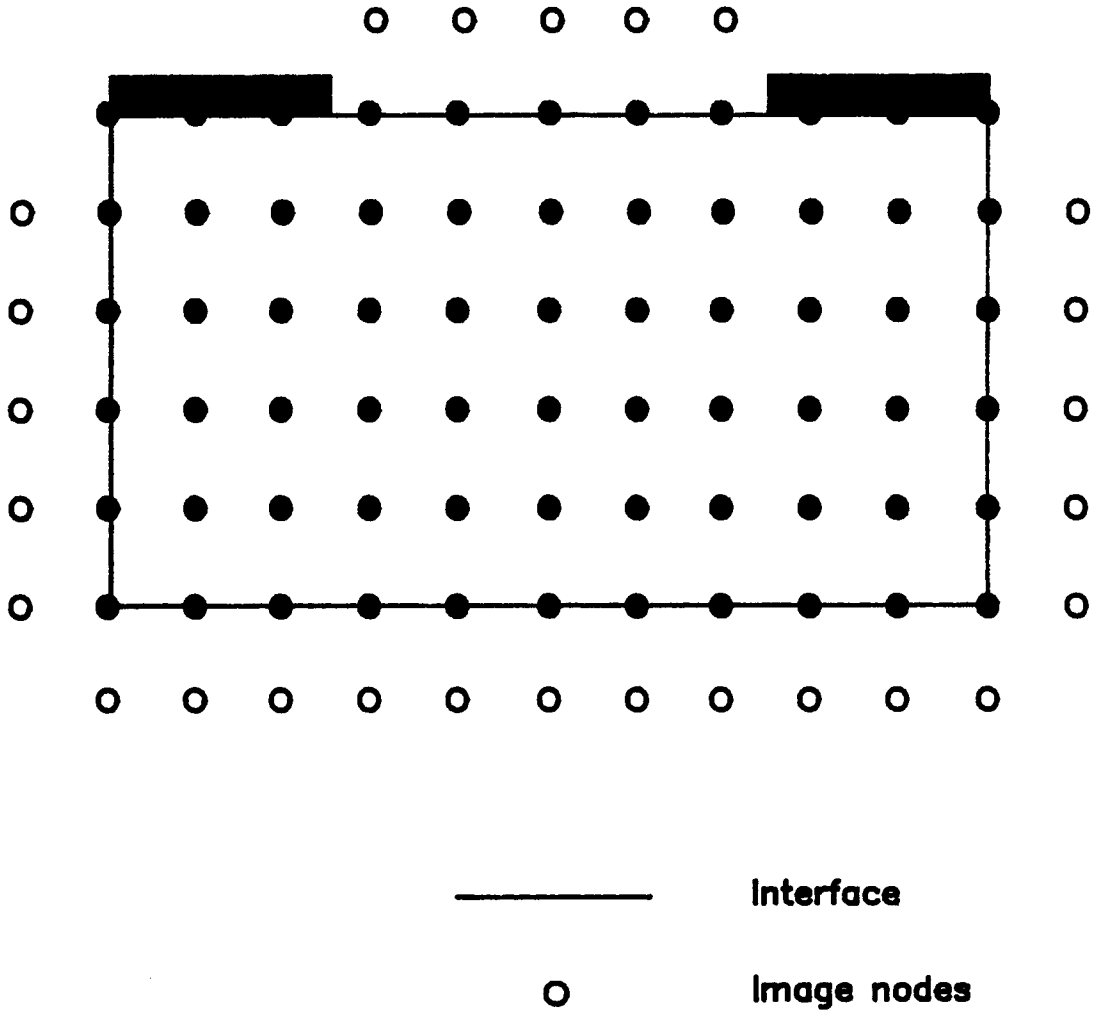

Fig. 4.6 Image nodes utilized in enforcing Neumann boundary conditions.

giving rapid convergence. Gummel's method is linear, i.e., the error decreases by about the same factor at each iteration. In Newton's method all of the equations are solved simultaneously whereas in Gummel's method the equations are solved sequentially.

The potential is assumed to be independent of time since the conductivity of the substrate is small. Hence the dielectric relaxation time is much greater than the response time of the detector. Under this assumption the Laplace equation and the continuity equations are completely decoupled and are linear differential equations. Gummel's method is used to solve these linear differential equations. Laplace's equation is solved just once and the continuity equations are solved L_T number of times where, $T_t = L_T \Delta t$, is the time in which the simulation is carried out.

The linear differential equations can be solved either by a direct method (Gaussian elimination) or an inner (linear) iteration method. The successive over-relaxation (SOR) iteration method is employed since it is economical in CPU time for large grids ($> 100 \times 100$) and round-off errors are negligible. In the SOR method the convergence is aided by over-relaxation, i.e., scaling up the update by a factor between 1 and 2. The method is described below.

According to the SOR method, the solution for the matrix equation,

$$[A][X] = [B],\ [A] = (a_{ij}),\ [B] = (b_i),\ [X] = (x_j),$$
$$(i,j)=1,2,\ldots,N \qquad (4.78)$$

is obtained by the following procedure [84]

$$
\begin{aligned}
x_1^{m+1} &= a_{11}^{-1}\,(b_1 - \sum_{j=2}^{N} a_{1j}x_j^m),\\
x_1^{m+1} &= x_1^m + \omega_{opt}(\bar{x}_1^{m+1} - x_1^m),\\
x_i^{m+1} &= a_{ii}^{-1}\,(b_i - \sum_{j=1}^{i-1} a_{ij}x_j^{m+1} - \sum_{j=i+1}^{N} a_{ij}x_j^m)\\
x_i^{m+1} &= x_i^m + \omega_{opt}(\bar{x}_i^{m+1} - x_i^m),\\
x_N^{m+1} &= a_{NN}^{-1}\,(b_N - \sum_{j=1}^{N-1} a_{Nj}x_j^{m+1}),\\
x_N^{m+1} &= x_N^m + \omega_{opt}(\bar{x}_N^{m+1} - x_N^m),
\end{aligned}
\tag{4.79}
$$

where superscript m is the iteration number and ω_{opt} is the optimum over-relaxation parameter.

The matrix notation introduced above is useful for theoretical analyses. Practical implementation of the SOR algorithm needs explicit formulas [99]. Corresponding to each row of the matrix A is an equation of the form

$$
a_{i,j}x_{i+1,j} + b_{i,j}x_{i-1,j} + c_{i,j}x_{i,j+1} + d_{i,j}x_{i,j-1} + e_{i,j}x_{i,j} = f_{i,j}\,. \tag{4.80}
$$

The iterative procedure is defined by solving equation (4.80) for $x_{i,j}$:

$$
x_{i,j}^{*} = \frac{1}{e_{i,j}}\,(f_{i,j} - a_{i,j}x_{i+1,j} - b_{i,j}x_{i-1,j} - c_{i,j}x_{i,j+1} - d_{i,j}x_{i,j-1}). \tag{4.81}
$$

Then $x_{i,j}^{new}$ is a weighted average

$$
x_{i,j}^{new} = x_{i,j}^{old} + \omega_{opt}(x_{i,j}^{*} - x_{i,j}^{old}). \tag{4.82}
$$

The residual at any stage is

$$\xi_{i,j} = a_{i,j}x_{i+1,j} + b_{i,j}x_{i-1,j} + c_{i,j}x_{i,j+1} + d_{i,j}x_{i,j-1} + e_{i,j}x_{i,j} - f_{i,j} \qquad (4.83)$$

and the SOR algorithm (4.82) is

$$x^{new}_{i,j} = x^{old}_{i,j} - w_{opt}\frac{\xi_{i,j}}{e_{i,j}} . \qquad (4.84)$$

This formulation is easy to program and the norm of the residual vector is used as a criterion for terminating the iteration. The flow chart for the problem is shown in Fig. 4.7.

4.9 Results

Potential distribution and electric fields are calculated for a detector with L = 100 μm, S = W = G = 5 μm, W_p = 100 μm, and N = 10. For these dimensions the length and the thickness of the domain are 10 μm and 2.5 μm, respectively. A uniform grid of size 400×100 is chosen which corresponds to h = Δx = Δy = 0.025 μm.

From the solution of Laplace's equation, the potential distribution is known at the grid points. The equipotential lines inside the domain are shown in Fig. 4.8. The potential plot is shown in Fig. 4.9. From the known potentials at the grid points, E_x and E_y are calculated and are plotted in Figs. 4.10 and 4.11, respectively. The electric field lines are perpendicular to the equipotential lines everywhere. The electric field at the surface is minimum at the center of the gap and increases at the electrode corners. In practice, the finite thickness and the specific geometry of the electrodes will tend to suppress this singularity in the

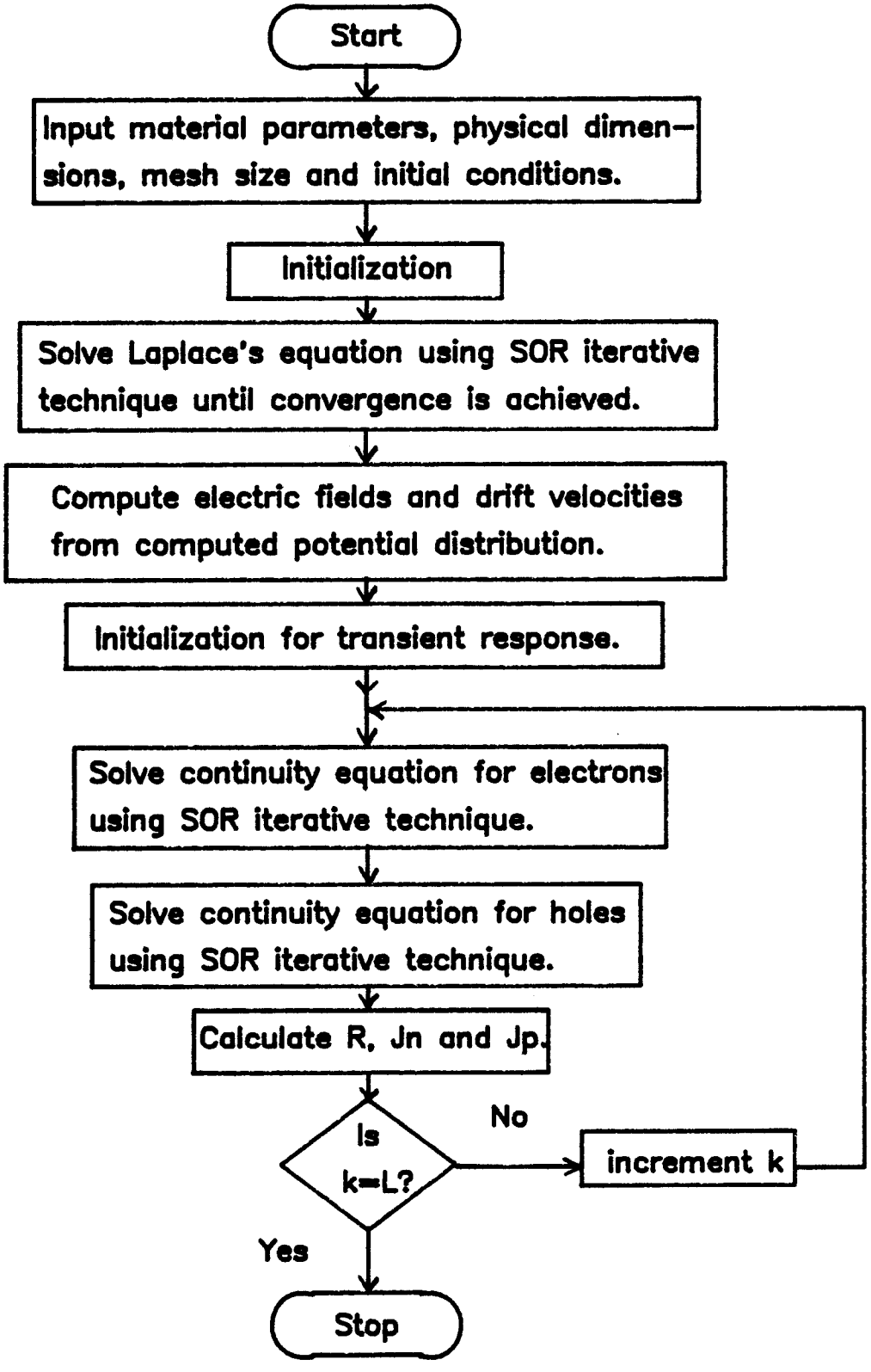

Fig. 4.7 Flow chart for the program.

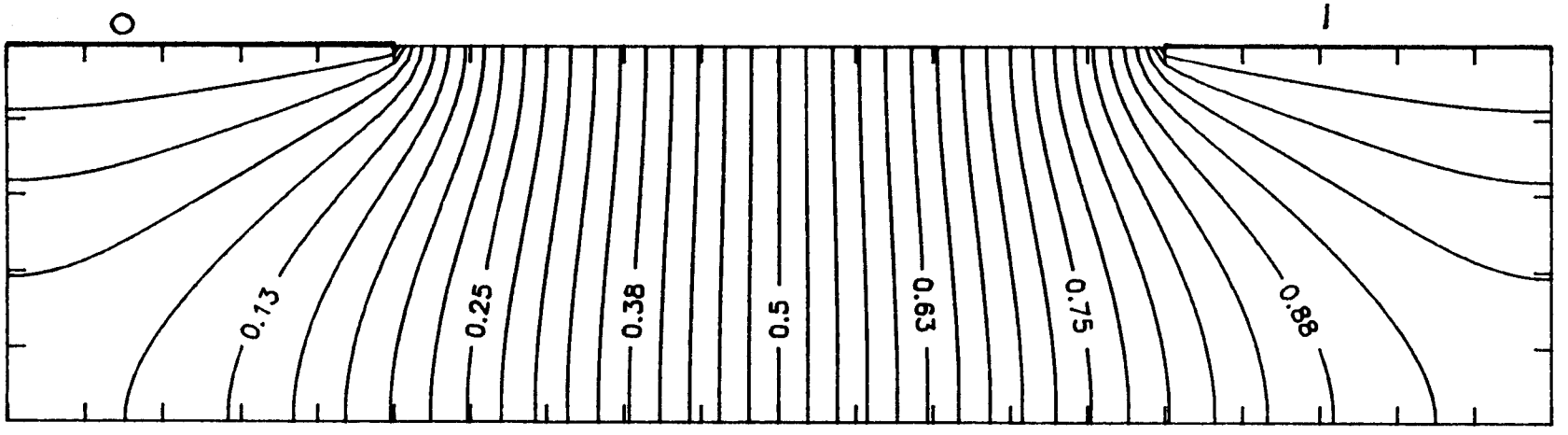

Fig. 4.8 Plot of equipotential lines.

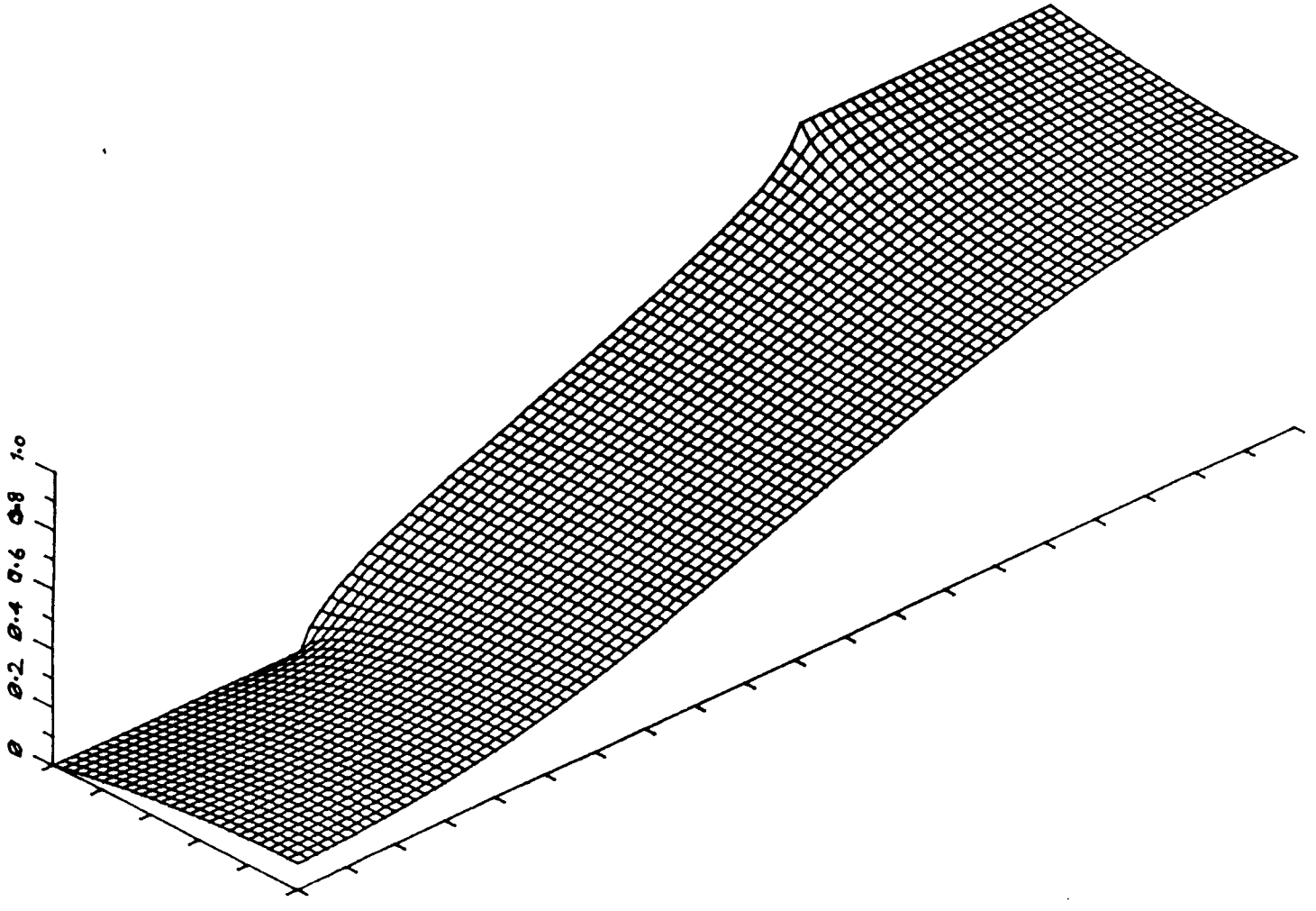

Fig. 4.9 Potential plot.

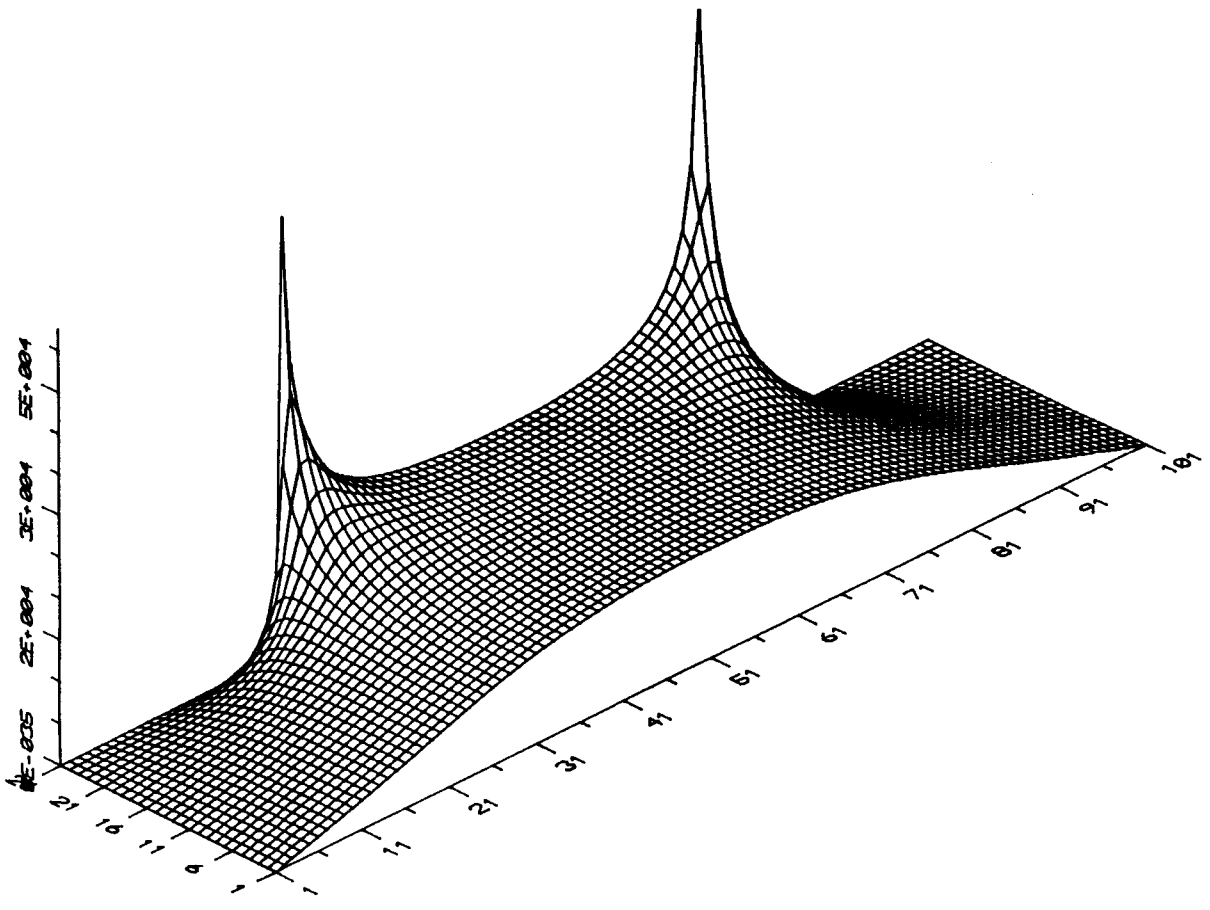

Fig. 4.10 Plot of electric field in the X—direction.

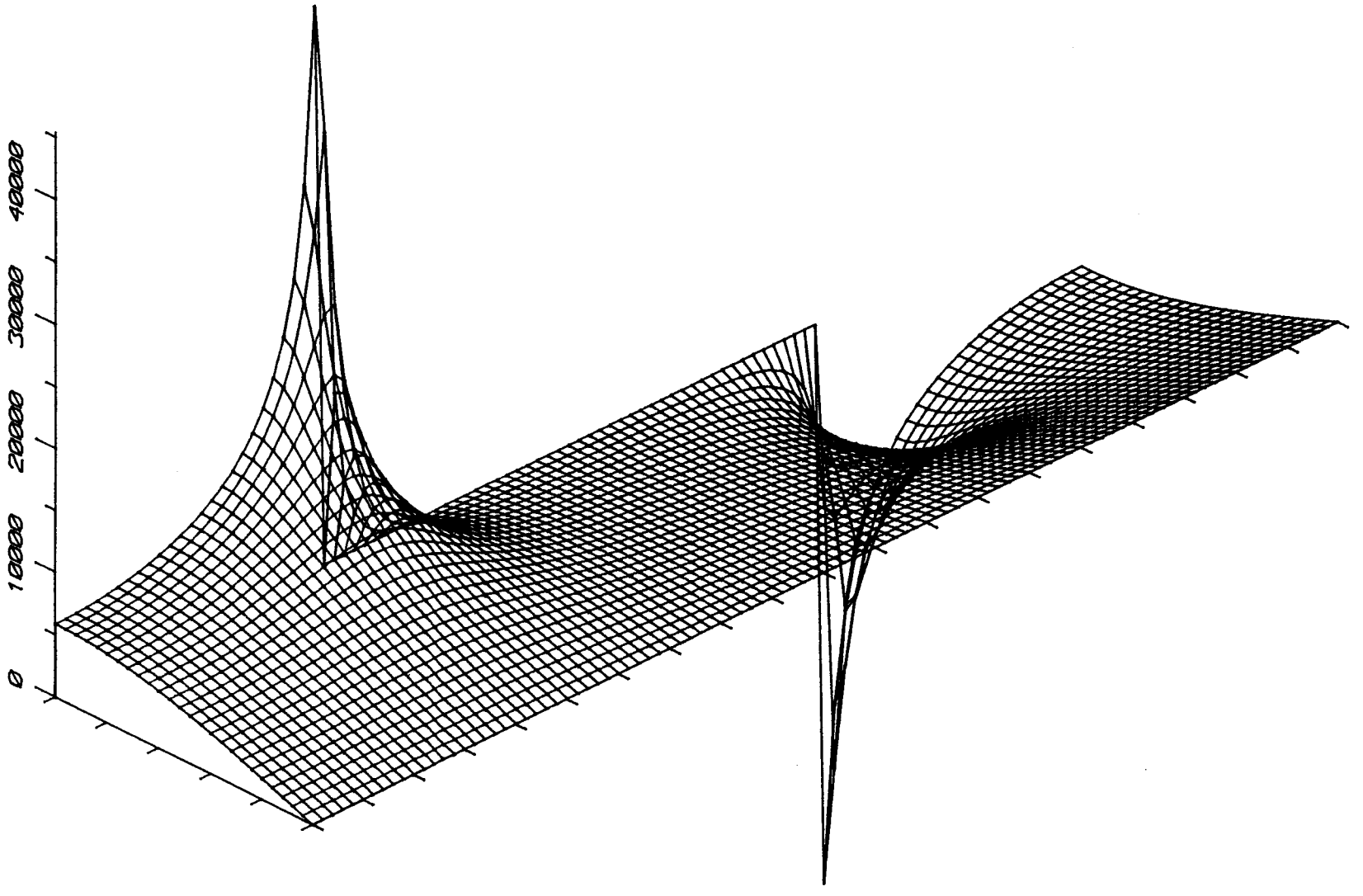

Fig. 4.11 Plot of electric field in the Y–direction.

field but a strong peak remains near the electrodes [1]. The constant field plot is shown in Fig. 4.12.

The current is spatially localized along the electric field lines. In the lateral direction, spatial confinement of the channel is achieved by the extent of the illumination itself or by the area of the interdigitated fingers. In the vertical direction, carrier confinement is achieved by the finite absorption depth of the illumination. Although some diffusion occurs transverse to the electric field lines (which is taken into account), the primary effects are caused by longitudinal carrier flow which is collinear with the field lines [32].

An optical impulse of uniform illumination is assumed to be incident on the surface of the interdigitated structure. Electron-hole pairs are generated within the domain due to photoabsorption and the resulting distribution of electrons and holes is calculated from equation (4.12) at $t=0^+$. Initial values for the electron and hole densities for subsequent times are furnished by the previous run. In general, the functions R, μ_n, and μ_p vary at each point in the device according to the values n, p, and E at that point if their dift velocities are not equal.

All of the carriers generated at $t=0^+$ contribute to the output current. As time progresses, the contribution to the current due to the carriers that reach the contacts or that are lost due to recombination is subtracted out. The impulse response of an ideal detector with the electric field perpendicular to the direction of incident light is shown in Fig. 4.13. Uniform electric field intensity, uniform light intensity, zero recombination, and blocking contacts are assumed. The shape of the impulse response is independent of the absorption coefficient. The areas under the curves

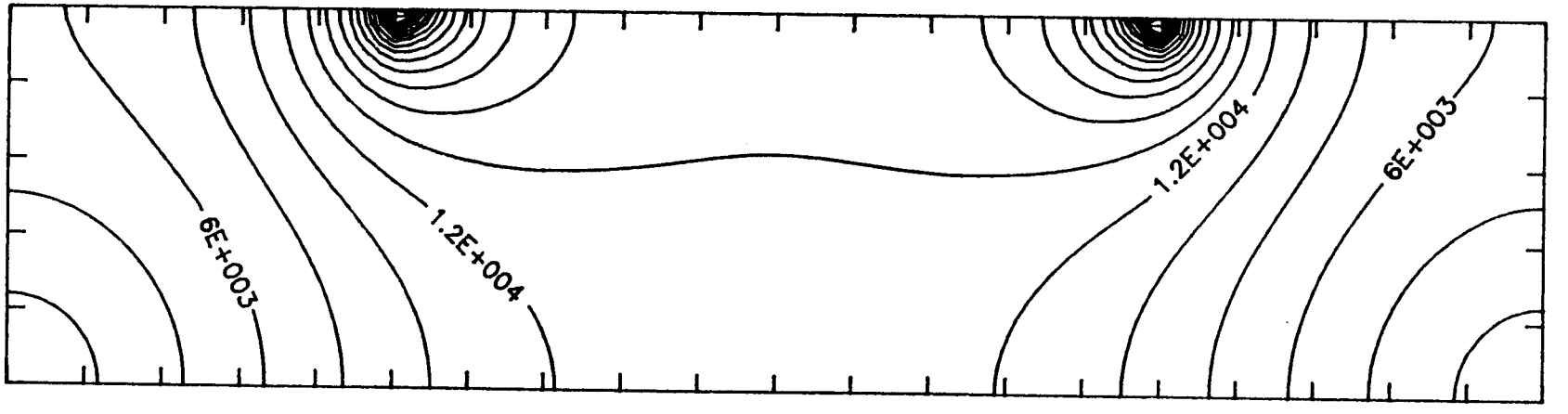

Fig. 4.12 Plot of constant electric field lines.

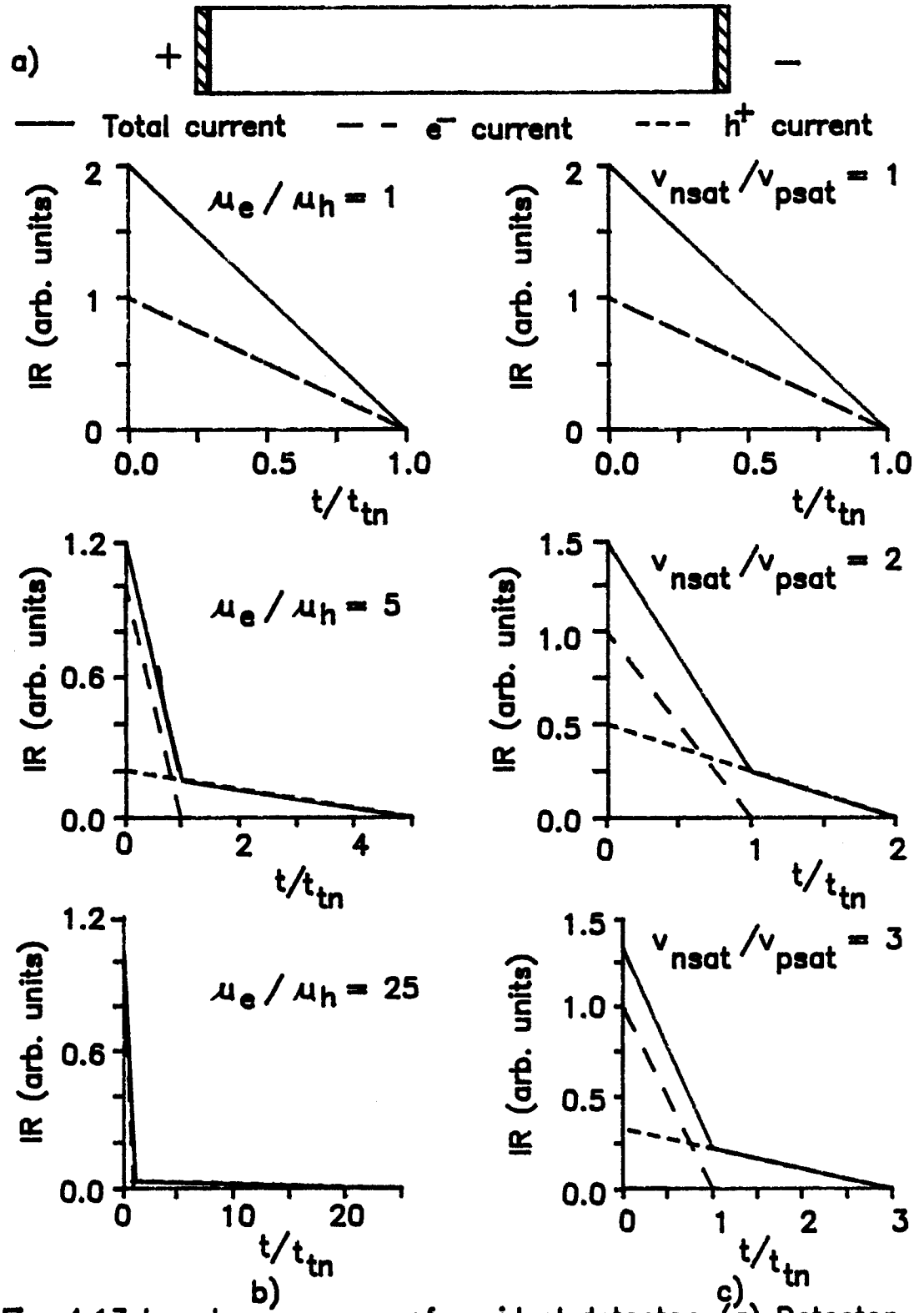

Fig. 4.13 Impulse response of an ideal detector. (a) Detector structure. b) IR for the linear region of the velocity–field curve. c) IR for the saturation region of the velocity–field curve.

for electrons and holes are equal. The influence of different mobilities and saturation velocities for electrons and holes is also shown in the figure.

The response shown in Fig. 4.13 is the particle or the intrinsic current. This current acts as the driving current for the external circuit which determines the current flowing through the load resistor. The impulse response of a simple photodetector is shown in Fig. 4.14. For the particle current shown in Fig. 4.14a, electron and hole drift velocities are assumed to be equal. The most simple equivalent circuit possible for a photodetector is shown in Fig. 4.14b. It consists of the detector capacitance, which is non-zero for any size detector, and the load resistance. The output voltage in terms of transit time and R_LC time constants is

$$v_o(t) = \begin{cases} i(t=0)*R_L[(1+R_LC/t_t)(1-\exp(-t/R_LC))-t/t_t] & 0\le t\le t_t \\ i(t=0)*R_L[R_LC/t_t-(1+R_LC/t_t)\exp(-t/R_LC)]* \\ \quad \exp[-(t-t_t)/R_LC] & t_t\le t\le \infty \end{cases} \quad (4.85)$$

The overall impulse response, shown in Fig. 4.16c, depends on both the transit time of the carriers and on the RC time constant of the detector.

Several authors have stressed the influence of parasitic circuit elements and the slow moving holes on the response time of the detector [11,45,47,48,100]. A typical equivalent circuit with parasitics which approximates a practical detector is shown in Fig. 4.15. R_D is the detector dark resistance, R_S is the series resistance due to the finite conductance of the fingers, pads and the connecting cables, C_{pack} is the capacitance of the package, L_S is the

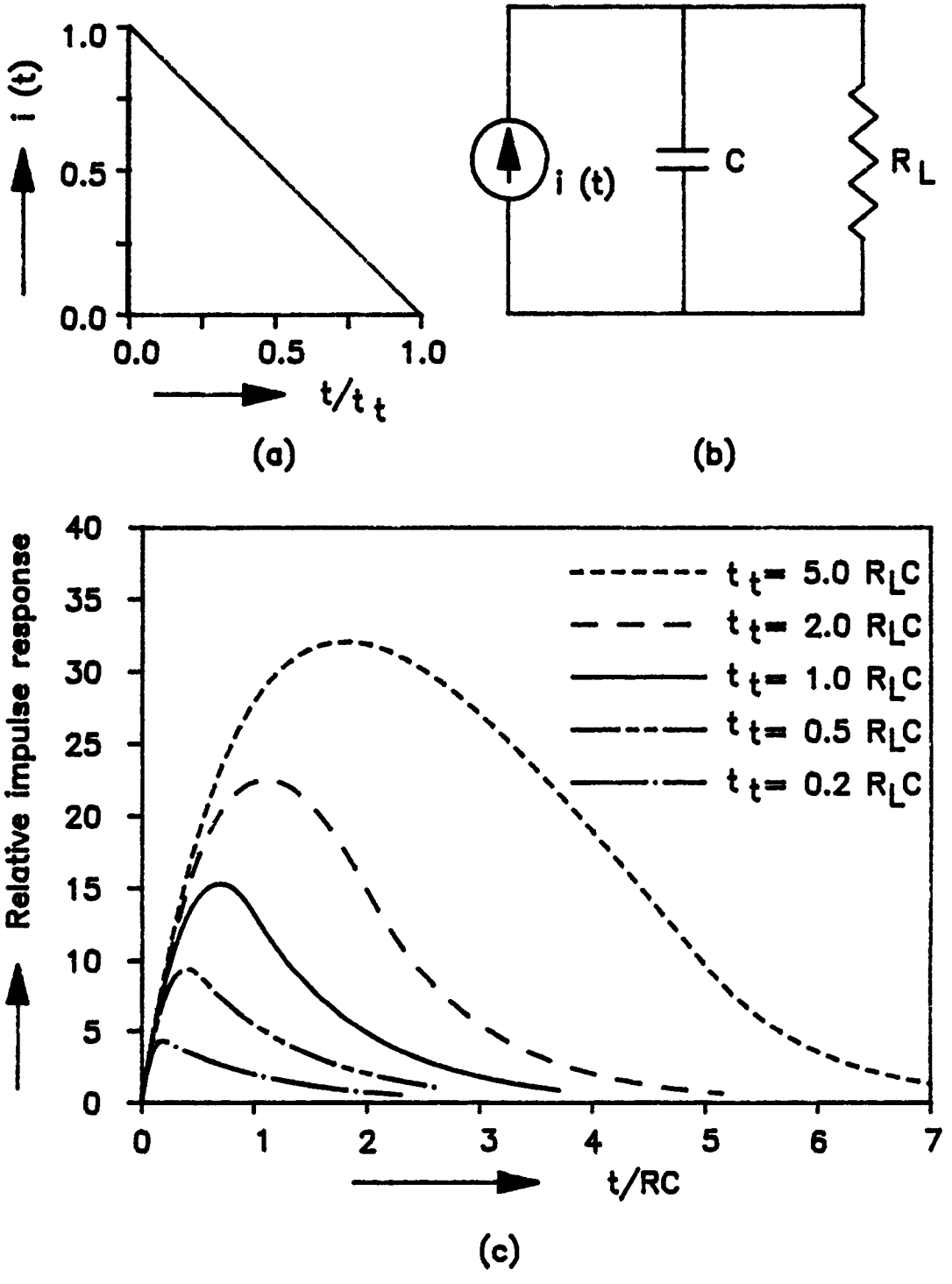

Fig. 4.14 Impulse response of a photodetector with a simple equivalent circuit. a) Particle current. b) External circuit. c) Overall response.

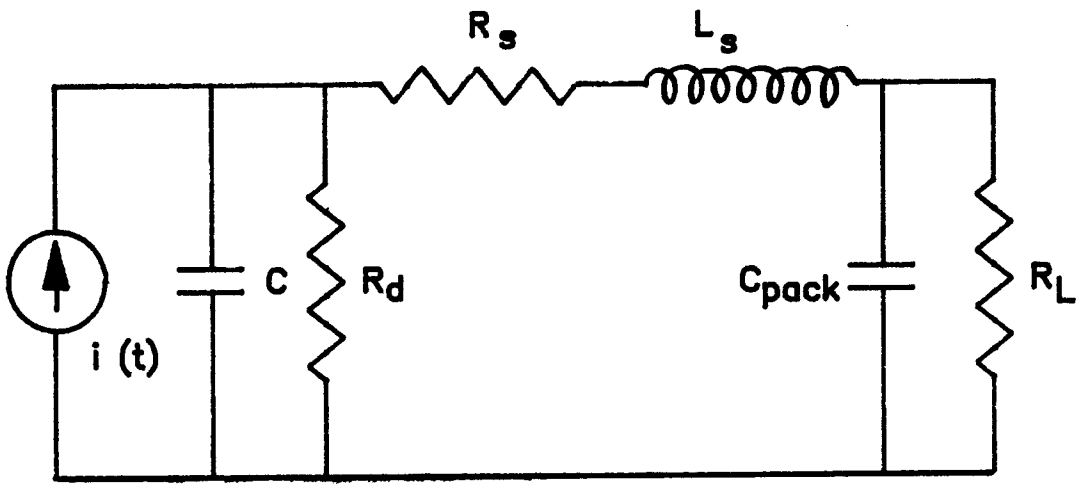

Fig. 4.15 Typical equivalent circuit of a photodetector.

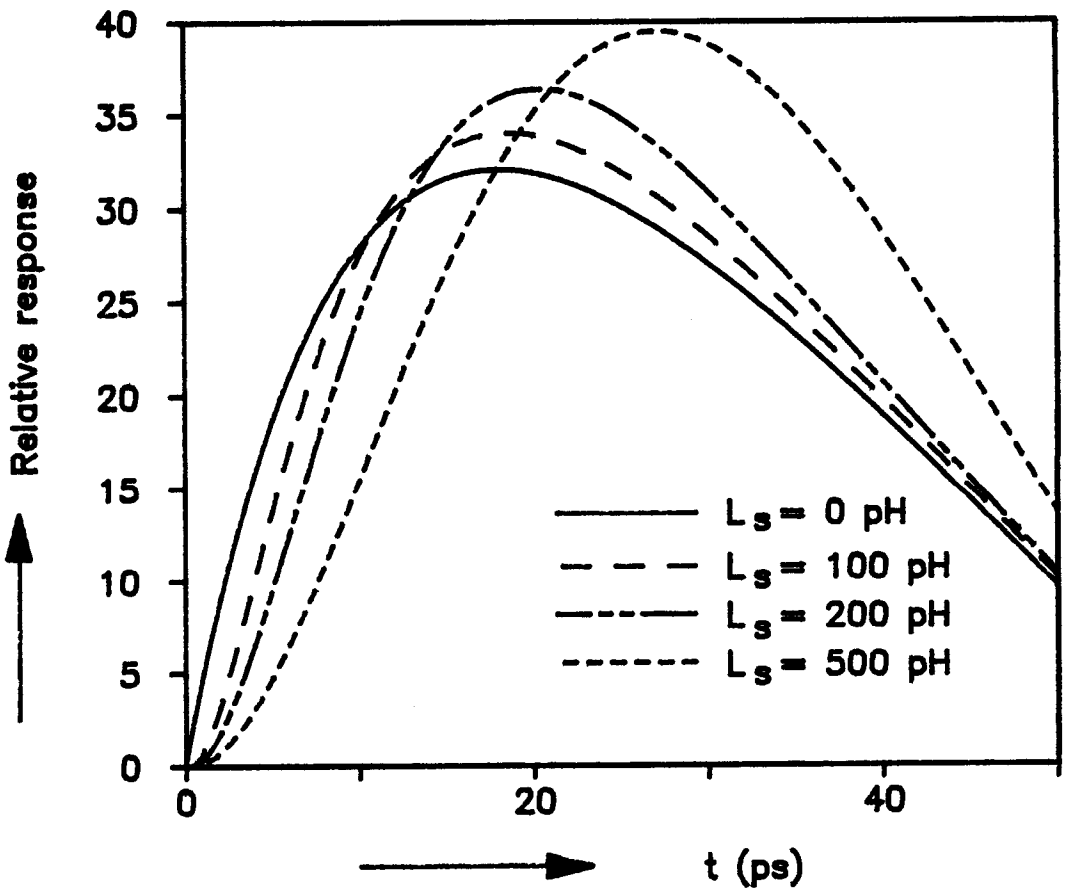

Fig. 4.16 Influence of Ls on the detector time response.

total inductance of the interdigital fingers and the bond wires. The dark resistance for the SI-GaAs MSM detector is in megaohms and its influence on the detector response can be neglected. The output voltage and the input current are related by the following 3rd-order differential equation.

$$\frac{d^3v_o}{dt^3} + C_1\frac{d^2v_o}{dt^2} + C_2\frac{dv_o}{dt} + C_3v_o = C_4i(t) \tag{4.86}$$

where

$$C_4 = 1/(L_sCC_{pack}) \tag{4.87}$$

$$C_3 = C_4/R_L \tag{4.88}$$

$$C_2 = C_3*(R_sC + R_LC + R_LC_{pack}) \tag{4.89}$$

$$C_1 = R_s/L_s + 1/(R_LC_{pack}) \tag{4.90}$$

This equation is solved using the fourth-order Runge Kutta numerical method. The influence of the parasitic circuit elements on the response of the detector is shown in Figs. 4.16-4.18 for a detector with N_f=13, S=5 μm, W=10 μm, l=200 μm, $v_n=v_p=10^7$ cm.sec^{-1}.

An analysis of an SI-GaAs MSM photodetector with the above mentioned dimensions was done by Nakajima et al. [64]. The measured capacitance of the detector is 0.2 pF which is the same as the one calculated from the interdigital structure model. Nakajima et al. [64] calculated the shape of the impulse response assuming the equivalent circuit shown in Fig. 4.14b. They have assumed that the electrons are traveling at a saturated drift velocity of 10^7 cm.sec^{-1} for an applied bias of 10 volts and the contribution to the impulse response from the holes was neglected. Then t_t = 50

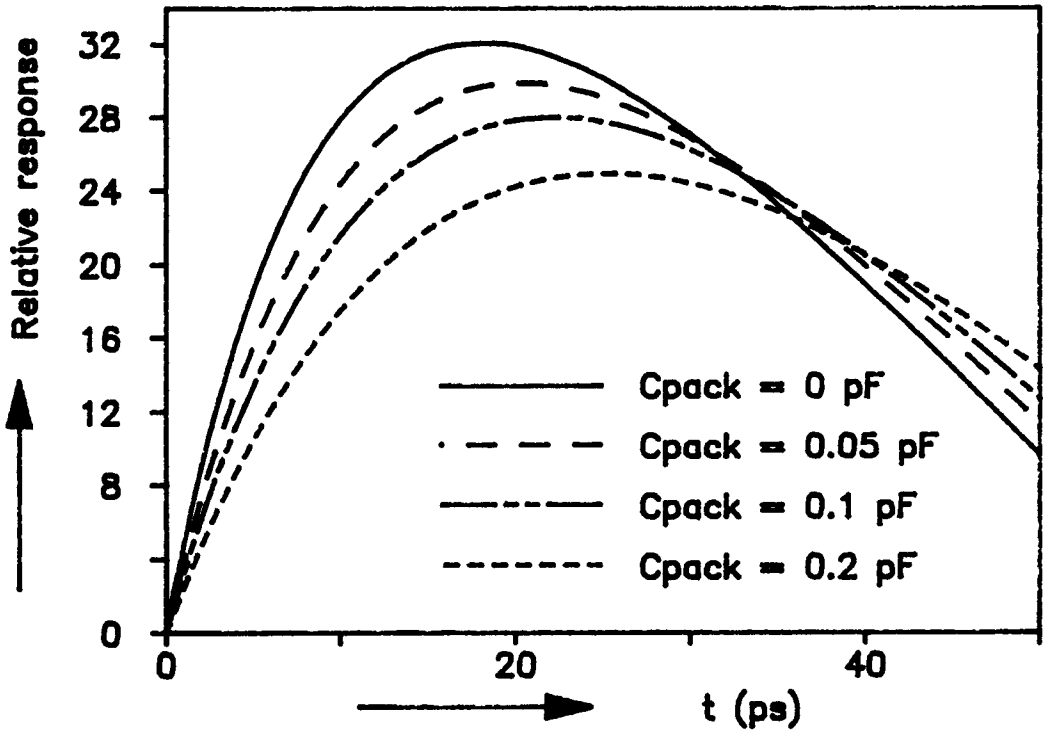

Fig. 4.17 Influence of Cpack on the detector time response.

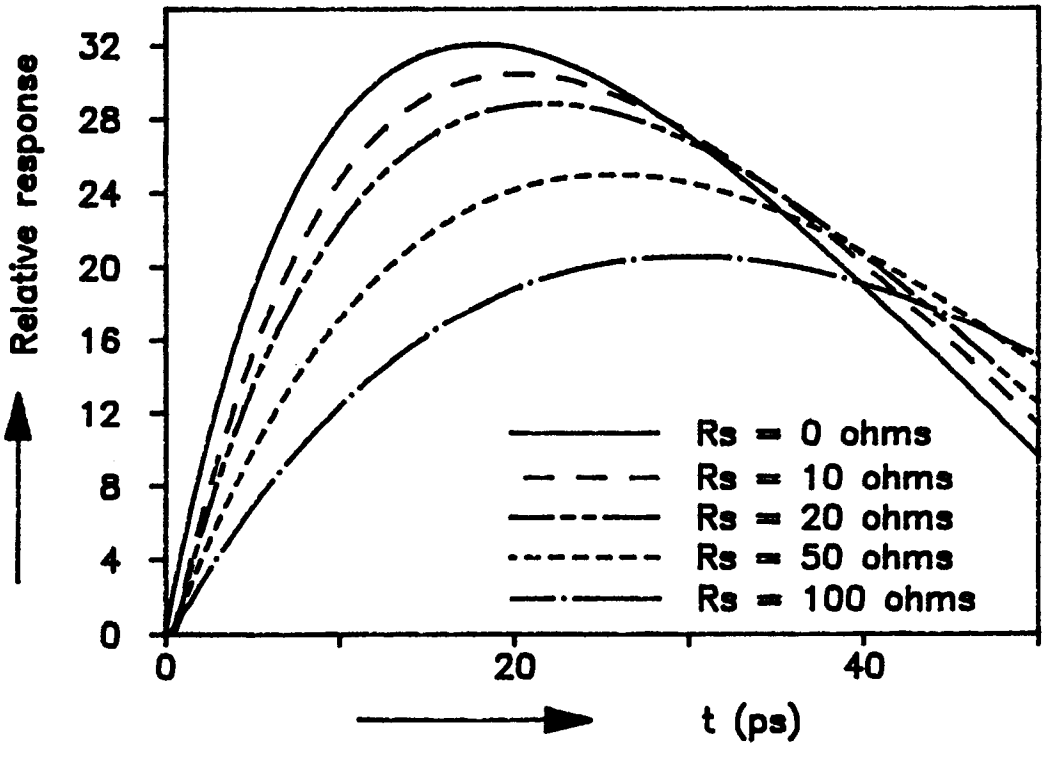

Fig. 4.18 Influence of Rs on the detector time response.

ps corresponding to the $t_t = 5R_LC$ case shown in Fig. 4.14c. This response is the same as the one calculated by Nakajima et al.

The calculated rise and fall times are 10 ps and 34 ps while the measured ones are 23 ps and 55 ps, respectively. The discrepancy is attributed by Nakajima et al. to the inductance of the bonding wires and to the finite rise time of the connecting cables. The simulated impulse response for the same detector with R_s=0 ohms, C=0.2 pF, C_{pack}=10 fF, R_L=50 ohms and L_s =50 pH is shown in Fig. 4.19. The rise and fall times are 12 ps and 50 ps, respectively.

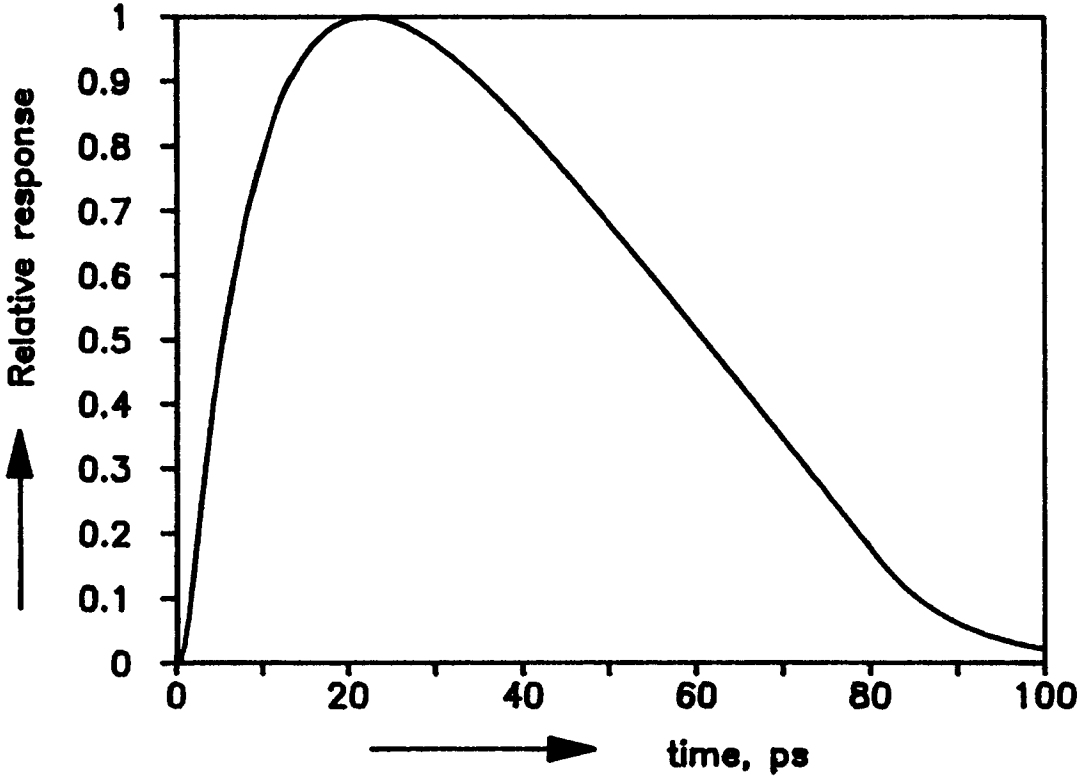

Fig. 4.19 Simulated impulse response of an MSM photodetector.

5. EXPERIMENTAL RESULTS AND DISCUSSION

5.1 Introduction:

In this chapter the fabrication process used for both ohmic and Schottky contact photodetectors made on SI-GaAs material is described. The packaging techniques used to test the pulse response are also described. The observed dark I-V and high speed pulse measurement results are reported and discussed. The modeled impulse response of the MSM photodetector is compared with the measured pulse response.

5.2 Detector fabrication:

A two-level photomask is made on ultraflat, high resolution photosensitive glass plates. The first level is used to define the interdigitated pattern on the GaAs surface and the second level is used to remove the anti-reflection (AR) coating material from the contact pads for bonding the device. The AR coating increases the amount of light coupled into the photodetector. It also acts as a surface passivation layer tying up the surface states to minimize the surface leakage current and protect the detector surface from humidity and scratches. The GaAs material has a refractive index of ~ 3.5. Without the AR coating, the Fresnel reflection, R_{surf} from the detector surface would be

$$R_{surf} = \left[\frac{n_{GaAs} - n_{air}}{n_{GaAs} + n_{air}} \right]^2 \qquad (5.1)$$

where n_{air} is the refractive index of air which is ~ 1.0. To reduce the 30% reflection loss to zero, a dielectric layer with a refractive index of

$$n_{dielectric} = \sqrt{n_{GaAs} \cdot n_{air}} \qquad (5.2)$$

and thickness $\lambda_o/4n_{dielectric}$ should be deposited on the detector surface. λ_o is the operating wavelength in free space. Usually silicon dioxide (SiO_2) or silicon nitride (Si_3N_4) are used as the passivating layers with refractive indices of ~ 2.0 and ~ 1.45, respectively. Then at an operating wavelength of 800 nm, the SiO_2 and Si_3N_4 layer thicknesses should be 1400 A and 1000 A, respectively. The processing steps for both ohmic and Schottky contact detectors are detailed in table 5.1.

5.3 Detector packaging:

Once a high speed photodetector is designed, packaging it properly is the next most important step. In many cases designing a good high speed package can be more difficult than making the high speed detector itself [11]. The influence of the parasitic elements introduced by the packaging on the time response of the detector is shown in chapter 4. The goal is to minimize these parasitic effects introduced by the package. Integration with an amplifier right next to the detector would eliminate the bond wire inductance and the package capacitance. However, the detector response should be known before it is integrated.

Three types of packages are used. In the first type, the detector is placed in a small gap in a microstrip (MS) line or in the center conductor of a coplanar waveguide (CPW). Since the load resistance is 50 ohms, the characteristic impedance of the MS and CPW lines should also be 50 ohms to avoid reflections from the load. The dielectric constant and the thickness of the microwave substrate employed are 10.2 and 1.25 mm, respectively. The

Table 5.1 Detector fabrication steps.

Step 1: Sample cleaning: Boil in TCA, acetone and IPA for 10 min. in each.

Step 2: Liftoff photolithographic step: Spin HMDS and then AZ1350J photoresist at 4500 RPM for 20 sec.
Softbake at 85 C for 20 min.
Chlorobenzene soak for 3 min. to harden surface.
Expose to 1st level mask at 16 $mW.cm^{-2}$ for 20 sec.
Develop in 3.5:1 DI H_2O:AZ1400 for 30-40 sec.

Step 3: Evaporation and annealing for ohmic contact detectors: HCl dip for 2 min. to remove native oxide.
Evaporate 0.2 g of Au:Ge, 0.015 g of Ni and 0.2 g of Au at $1.0E^{-6}$ Torr in succession.
Anneal at 420 C for 3 min.

Step 4: Evaporation for Schottky barrier detectors: HCl dip for 2 min.
Evaporate 0.015 g of Ti, 0.02 g of Pd and 0.2 g of Au at $1.0E^{-6}$ Torr in succession.

Step 5: AR coating: Clean the sample with acetone, methanol and DI H_2O.
Deposit 1400 A of SiO_2 by PECVD technique.

Step 6: Bond pad opening: Spin HMDS and then AZ1350J photoresist at 4500 RPM for 20 sec.
Softbake at 60 C for 5 min.
Expose to 2nd level mask at 16 $mW.cm^{-2}$ for 20 sec.
Develop in 3.5:1 DI H_2O:AZ1400 for 30-40 sec.
Hardbake at 120 C for 5 min.
Buffered HF dip to remove SiO_2 (etch rate ~ 1000 A/min.)
Remove photoresist with acetone.

dielectric is covered with 70 μm thick copper strips on both sides. The dimensions of the 50 ohm line are patterned onto the substrate using photolithographic process. The detectors are bonded to the microwave substrate by silver epoxy and wire bonded to the copper strip with multiple 1-mil Au wires to decrease bond inductance. No bias-T was required for this package.

In the second type, the detector is placed at the end of a 50 ohm SMA connector. A bias-T is used with this package to isolate the pulse output from the DC bias voltage. The two types of packages are shown in Fig. 5.1. The third package used was designed at Tektronix, Inc., Beaverton, OR, for high speed device testing.

5.4 I-V characteristics of the detectors:

The dimensions of the fabricated detectors are shown in table 5.2. DET1-DET4 are ohmic contact detectors and DET5 is an MSM detector. DET6 is an MSM detector with a simple gap. The gap length is 5 μm and gap width is 50 μm. DET7 is again a simple gap detector with ohmic contacts. The gap length is 8 μm and width is 50 μm. DET1-DET5 are made at Oregon State University and DET6-DET7 are made at Tektronix, Inc.

The measured I-V characteristics of detectors DET1 and DET5 are shown in Fig. 5.2 and Fig. 5.3, respectively. The current is plotted both on linear and logarithmic scales. The I-V characteristics of DET2-DET4 are similar to the one shown in Fig. 5.2. The interdigitated ohmic contact detectors have an SiO_2 passivating/AR coating layer whereas the MSM interdigitated detector has no passivating layer at all. The detectors fabricated at Tektronix have an Si_3N_4 passivating layer. The I-V characteristics of these detectors are given in [61,62].

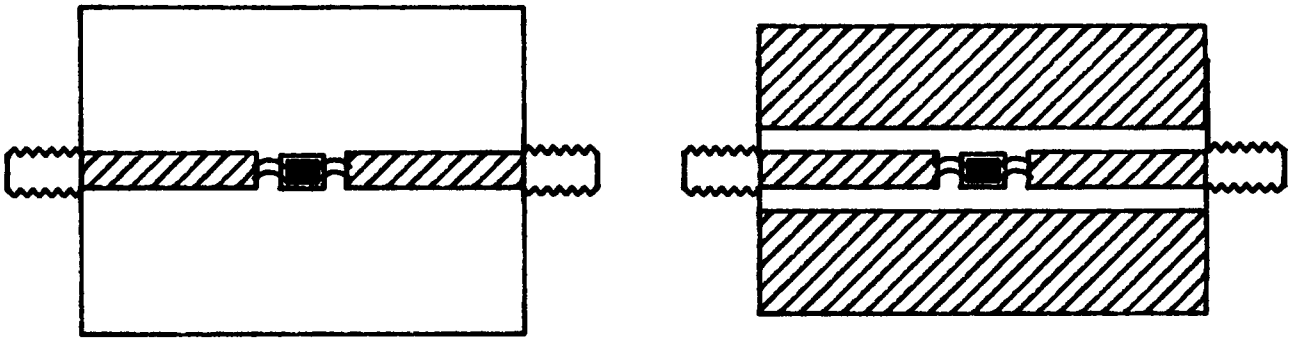

(a)

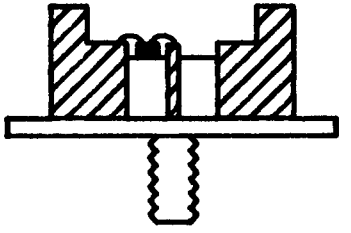

(b)

Fig. 5.1 Two types of packaging techniques. a) Microstrip and coplanar packaging. b) SMA connector end packaging.

Table 5.2 Detector dimensions.

Detector ID	l (mm)	S (μm)	W (μm)	W_p (μm)	G (μm)	N
DET1 (ohmic)	4	80	10	100	160	44
DET2 (ohmic)	2	32	8	100	64	50
DET3 (ohmic)	1.5	25	5	100	50	50
DET4 (ohmic)	1	16	4	100	32	50
DET5 (MSM)	1.5	25	5	100	50	50
DET6 (MSM)	Simple gap with S=5 μm and width W=50 μm.					
DET7 (ohmic)	Simple gap with S=8 μm and width W=50 μm.					

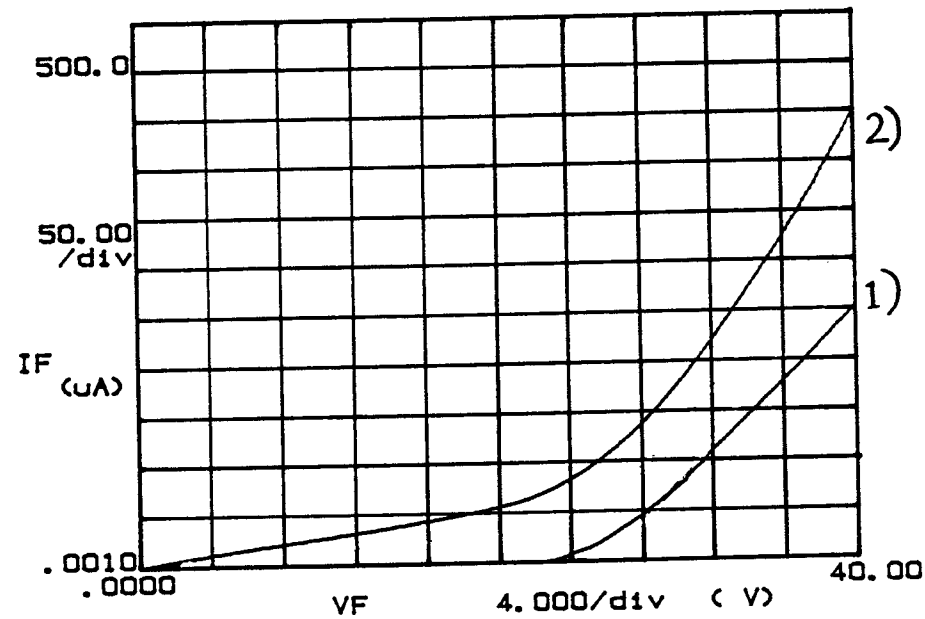

a)

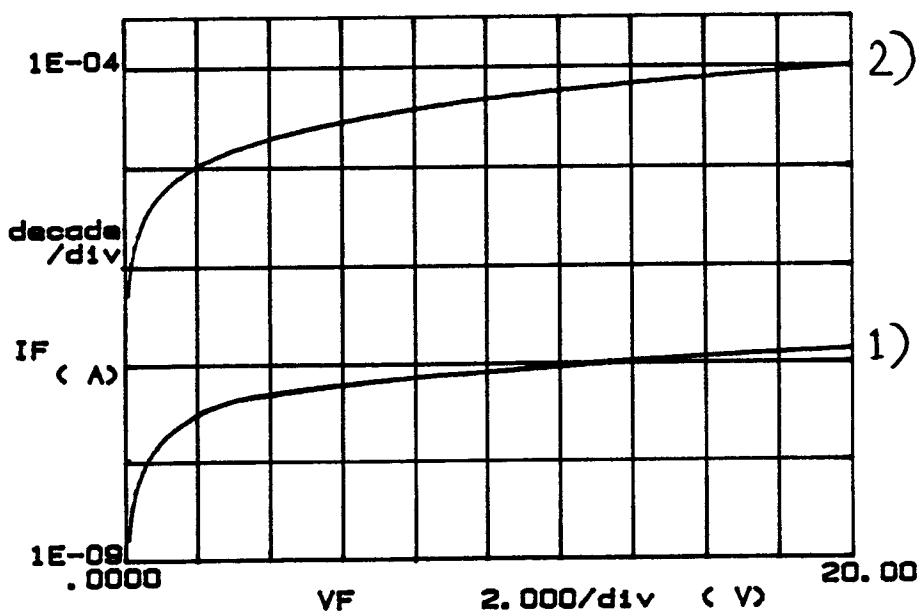

b)

Fig. 5.2 Typical plot of observed I–V curves for ohmic contact detectors: a) linear plot, and b) semilog plot. (1–dark current, 2–current under microscope light illumination).

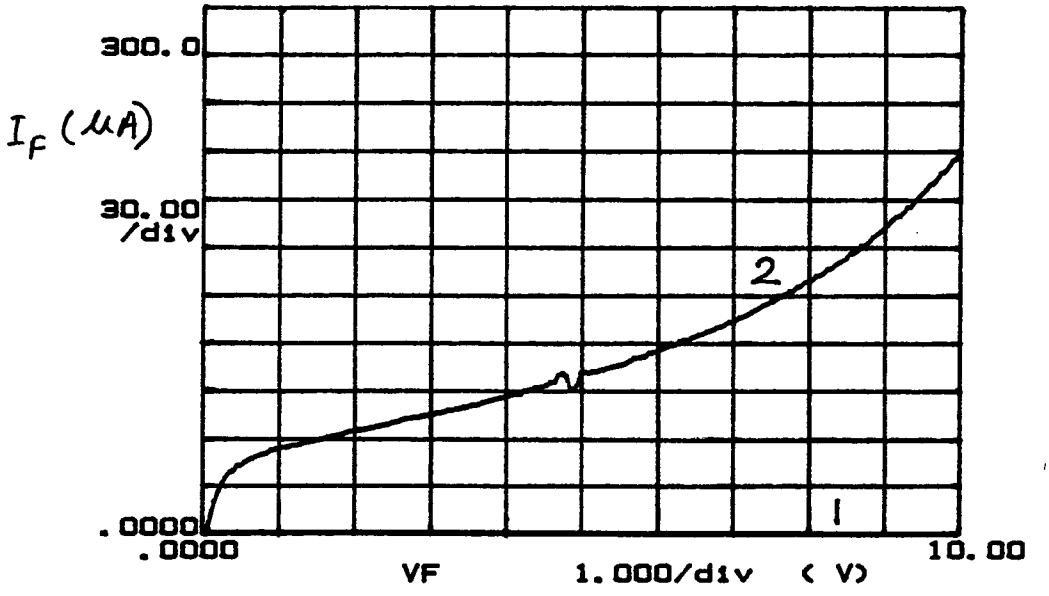

a)

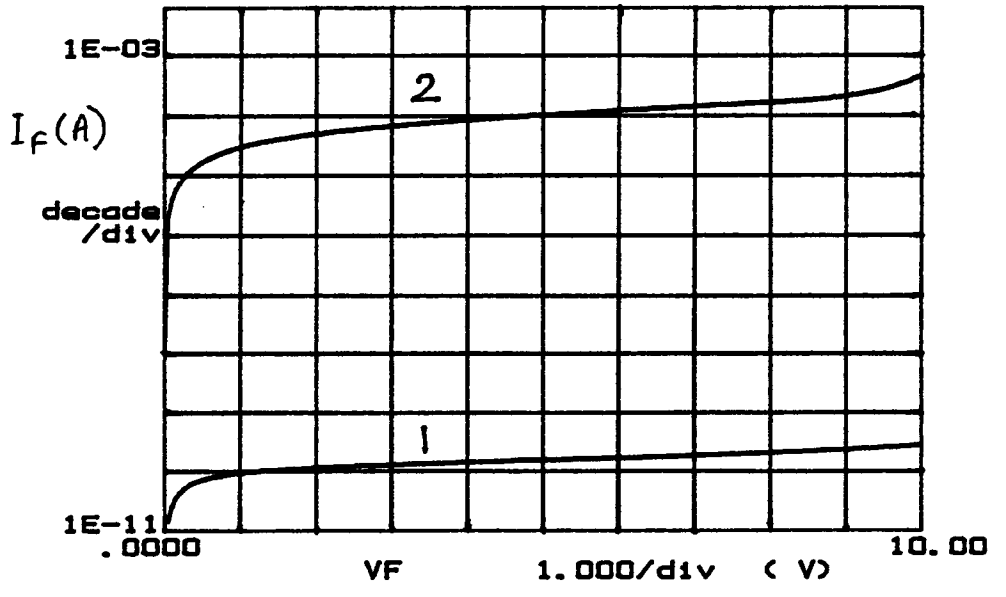

b)

Fig. 5.3 Typical plot of observed I–V curves for MSM detectors: a) linear plot, and b) semilog plot. (1–dark current, 2–current under microscope light illumination).

5.5 Pulse measurements:

The packaged detectors are tested with a Tektronix Optical Impulse Generator (OIG 501) and with a mode-locked dye laser. The OIG 501 operates at 850 nm with two pulse modes. In the "low energy" mode, the optical output pulse width (FWHM) is < 35 ps with an output power of > 10 mW. In the "high energy" mode, the optical pulse width is < 300 ps with an output power of > 25 mW. The pulse repetition frequency can be set to 10 kHz, 100 kHz or 1 MHz. A block diagram of the system used for making pulse measurements with the dye laser is shown in Fig. 5.4. The pulse repetition frequency can be varied between 20 kHz and 800 kHz.

The typical observed shape of the pulse measurements made on the interdigitated ohmic contact detectors using the dye laser is shown in Fig. 5.5. The bias conditions and the observed rise and fall times are shown in table 5.3. The pulse responses of DET2 and DET4 to OIG 501 in the high energy mode are shown in Fig. 5.6. The pulse response of the simple ohmic gap to the dye laser pulse is shown in Fig. 5.7.

The pulse responses of the MSM interdigitated photodetector to both the OIG 501 and the dye laser are shown in Fig. 5.8. The pulse responses of the interdigitated MSM detector (DET5) and the interdigitated ohmic contact detector (DET3) which have the same dimensions are compared in Fig. 5.9. Finally, the measured pulse responses of the MSM gap detector are compared in Fig. 5.10 for the Tektronix package and the SMA package.

5.6 Discussion:

The measured dark current is almost three orders of

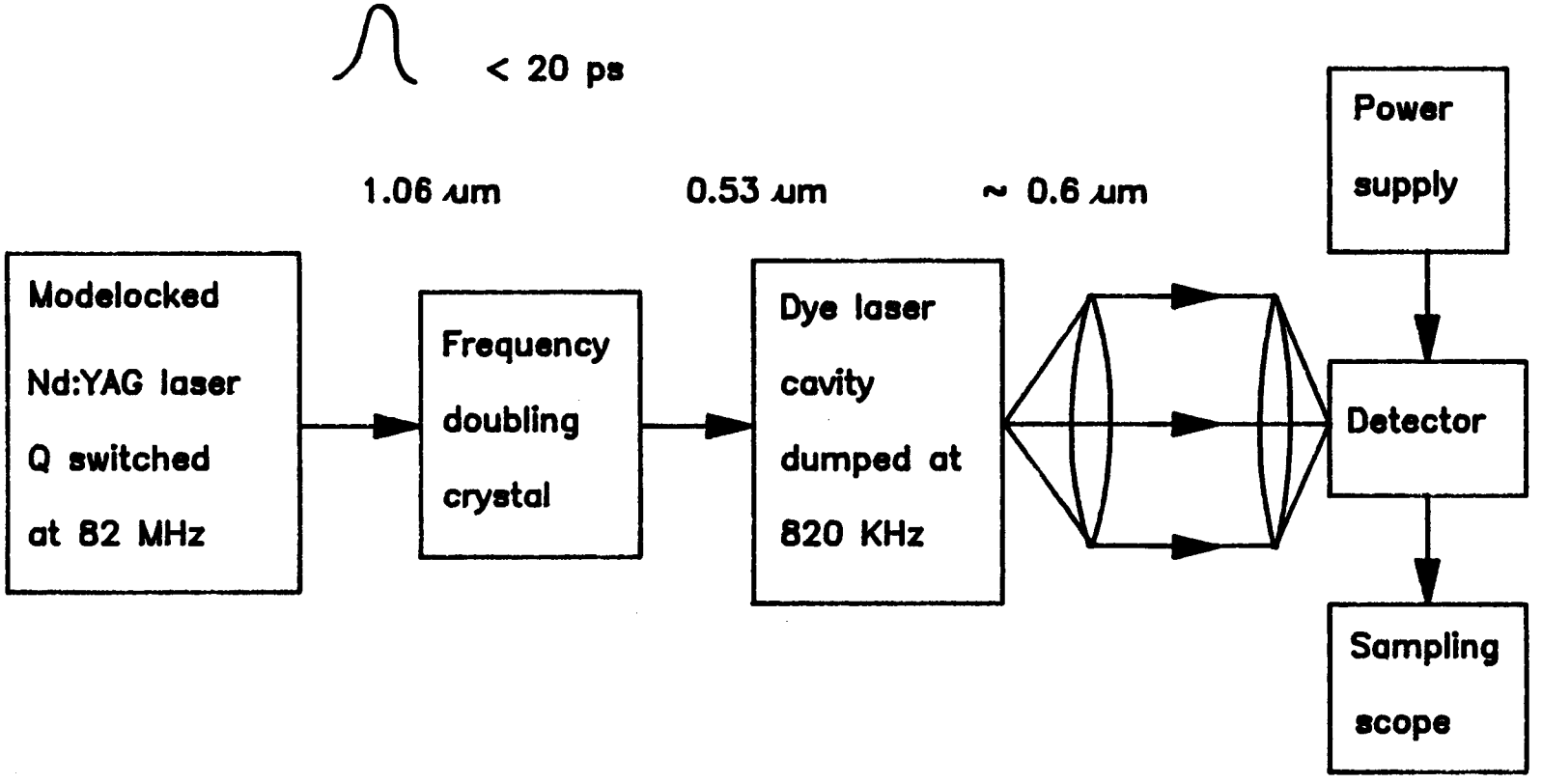

Fig. 5.4 Block diagram for pulse measurements.

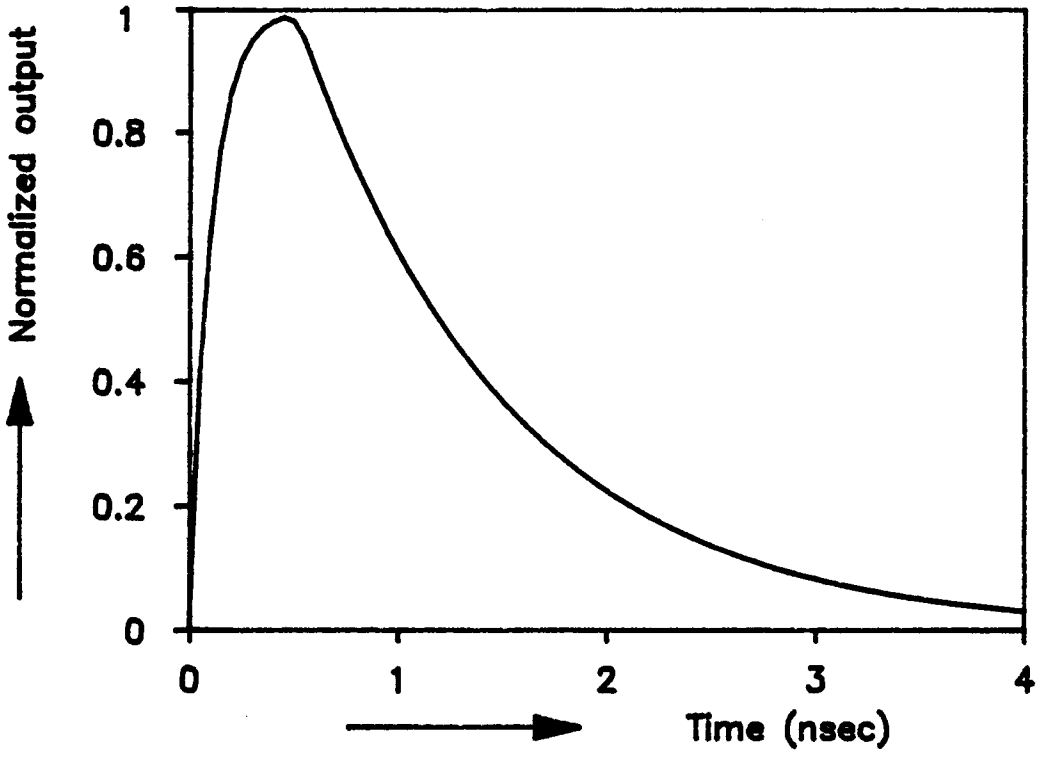

Fig. 5.5 Observed shape of the pulse response for omhic contact detectors.

Table 5.3 Bias conditions for pulse measurements and the observed rise and fall times.

Det. ID	Bias, v	Det. current, mA	Risetime, ps	Falltime, ns
DET1	40	2	200	3.5
DET2	15	1	140	2.5
DET3	10	0.47	120	2.5
DET4	15	0.4	100	3.5

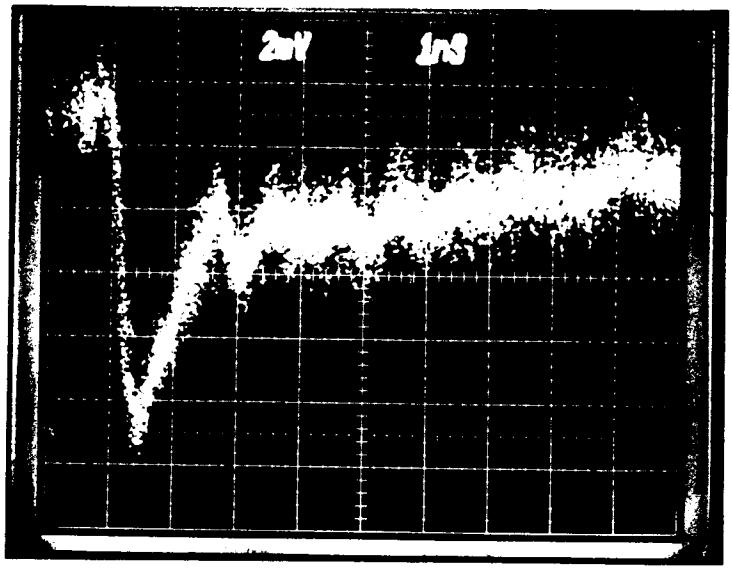

a)

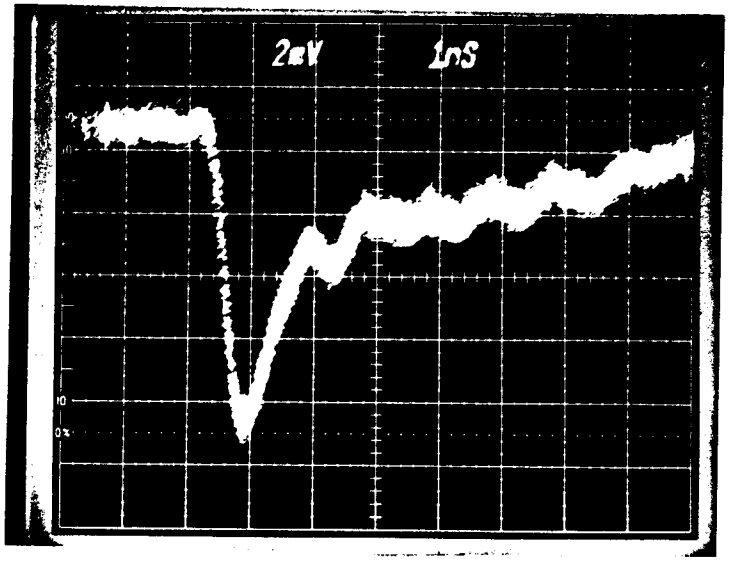

b)

Fig. 5.6 Pulse response of interdigital ohmic detectors: a) DET2, bias = 11 v, and b) DET4, bias = 5.5 v.

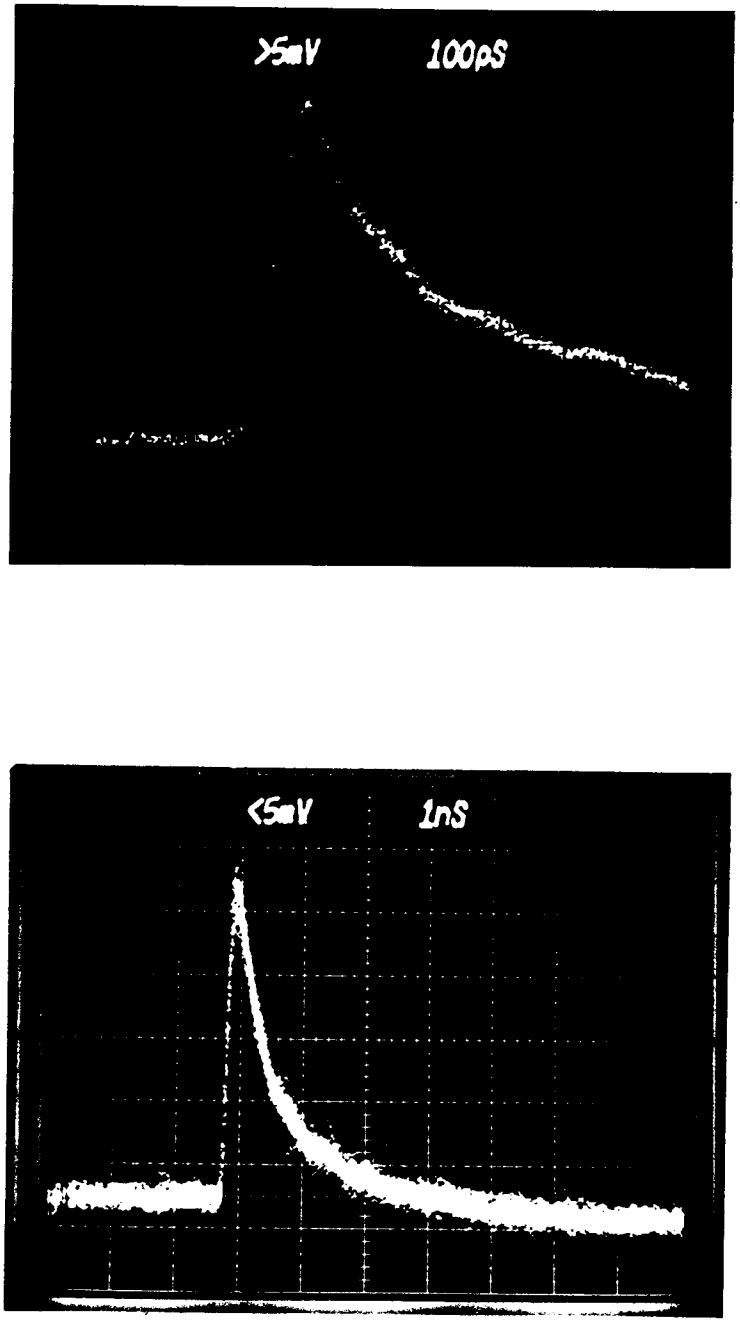

Fig. 5.7 Pulse response of an 8– um gap with ohmic contacts (bias = 10 v).

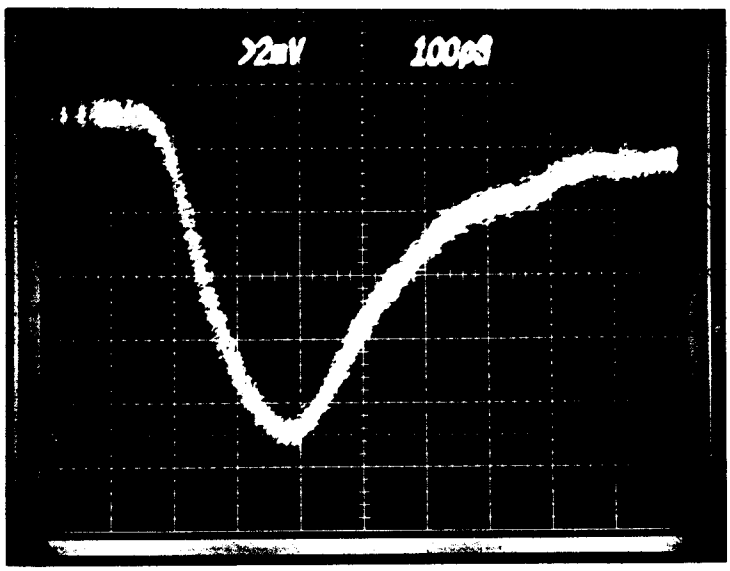

a)

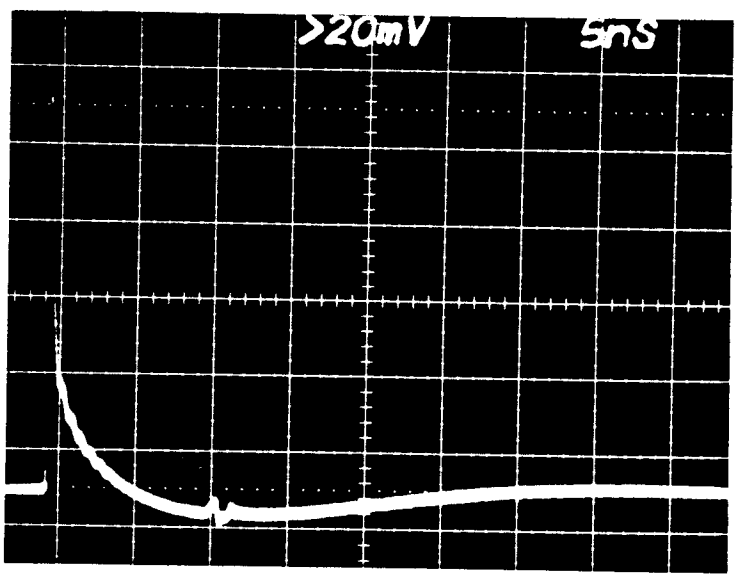

b)

Fig. 5.8 Pulse response of interdigital MSM detector: a) OIG response, and b) Dye laser response (bias = 16 v).

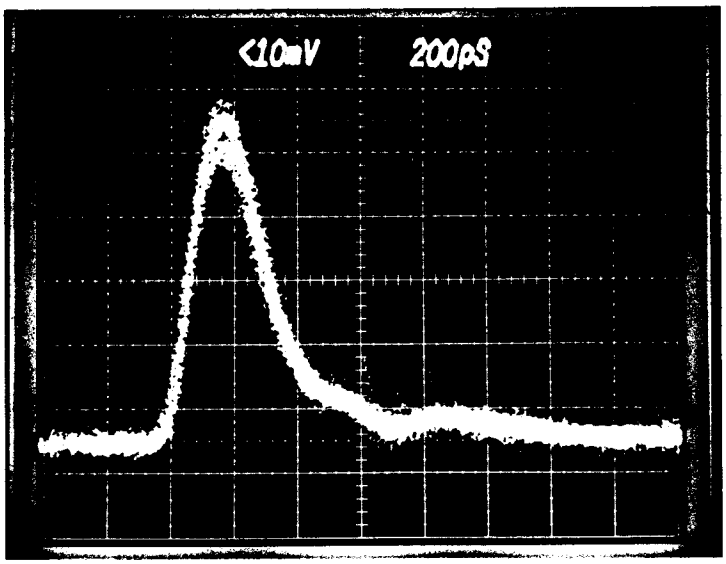

a)

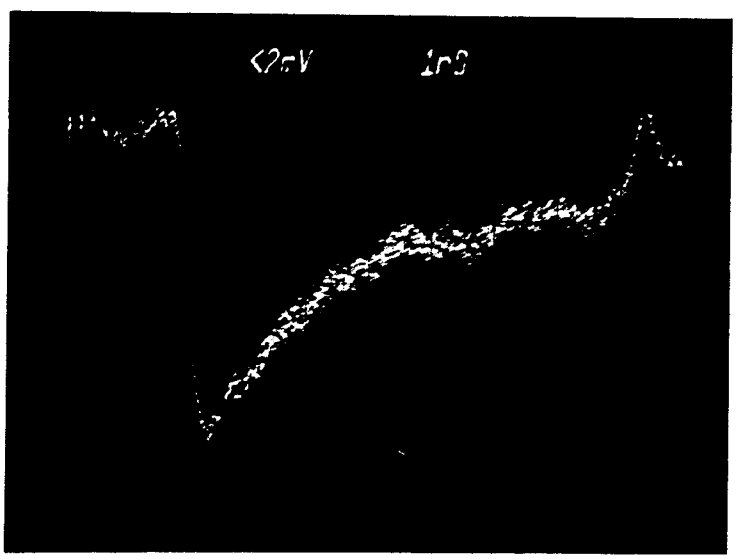

b)

Fig. 5.9 Pulse response comparison of ohmic and Schottky contact detectors: a) MSM detector, and b) Ohmic detector.

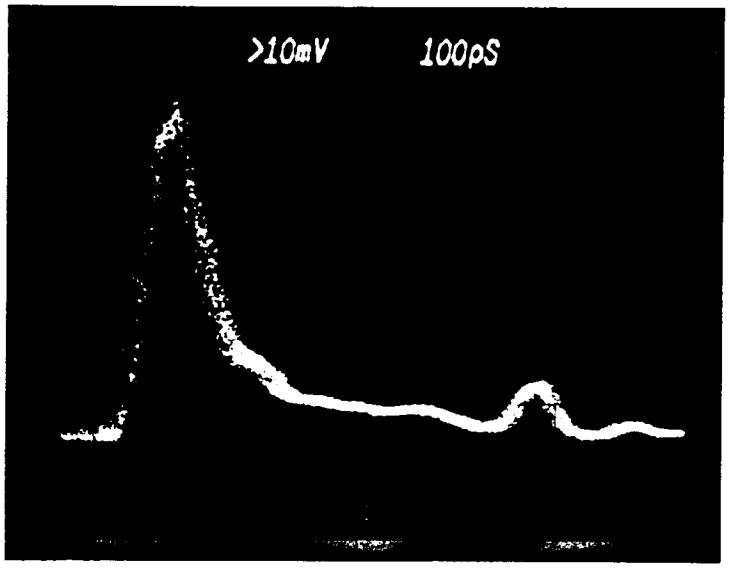

a)

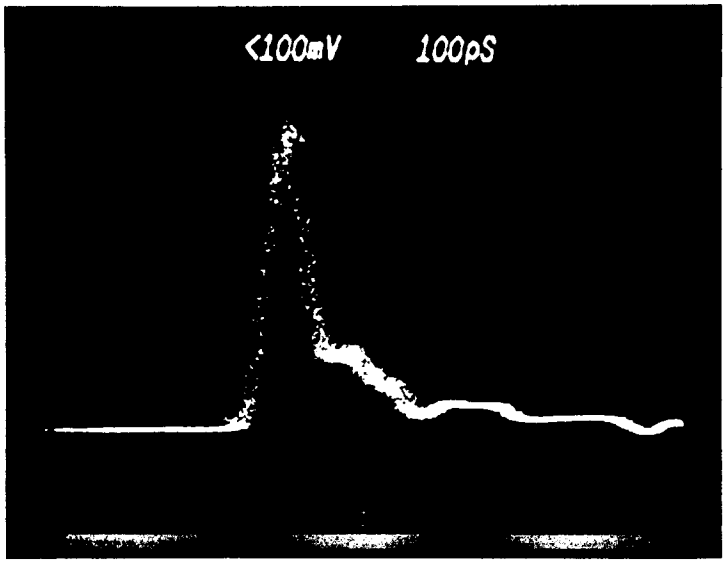

b)

Fig. 5.10 Influence of packaging on the detector response: a) Tektronix package, and b) SMA connector package.

magnitude lower than the microscope-illuminated current. The ohmic contact detectors have linear I-V characteristics at lower electric fields but start rising nonlinearly at fields greater than about 5 $kV.cm^{-1}$. This can be explained by the space charge injection phenomenon which causes a space charge limited current to flow through the semi-insulating substrate at high fields [101]. However, the observed fields at which the exponential rise in dark current occurs are lower for the ohmic contact interdigitated detectors here than the ones observed in the literature [5,61,62].

Lee et al. [102] have shown that SiO_2 passivation on GaAs is inferior to Si_3N_4 and inferior to even a bare GaAs surface. So the surface leakage current might be causing the nonlinear rise in the dark current at fields > 5 $kV.cm^{-1}$. The leakage current can be reduced further by employing Si_3N_4 as the passivation layer instead of SiO_2. The linear portion of the I-V curve can be extended to higher fields with Si_3N_4 passivation layer if the surface leakage current is causing the nonlinear rise in dark current.

The observed rise times of all the ohmic detectors are in the hundreds of picoseconds range and are limited by the RC time constant. The fall times, however, are not proportional to either the transit time or the RC limited decay time. The fall time is almost independent of the detector dimensions. A similar observation was made by Boudebous [5]. The capture time of the photogenerated electrons by the EL2 traps is much longer than the input pulse width and the transit time of the electrons across the gap under moderate excitation conditions. So the effect of EL2 traps on the pulse response of the detector is negligible. The fall times of the detectors made on n-epi

layers of GaAs also have longer fall times than predicted. Vilcot et al. [26] and Matsuo et al. [27] made the observation that the photogenerated holes are trapped at the surface because of the surface band bending caused by Fermi level pinning at the surface.

The energy-band diagram of the photoconductive SI-GaAs detector in thermal equilibrium and under bias in the dark and under illumination is shown in Fig. 5.11. The equilibrium Fermi level is at 0.6 eV below the conduction band for an electron concentration of $5X10^{7}$ cm^{-3}. The metal-n^{+} barrier at the "ohmic" contacts is so thin that the electrons can easily tunnel through the barrier in both directions. The depletion layer width at the n^{+}-SI GaAs interface is approximately 1.7 μm assuming a net (N_{SA}-N_{SD}) shallow acceptor concentration of $3X10^{14}$ cm^{-3} [19]. The band bending (E_c-E_f) at the surface of SI-GaAs is ~ 0.2 eV whereas the band bending at the surface of an n-epilayer (N_D=$1X10^{15}$ cm^{-3}) ~ 0.6 eV. So the hole trapping effect due to band bending at the surface of SI-GaAs is not as severe as at an n-epi layer surface.

The applied voltage is dropped across three regions: 1) across the n^{+}/SI-GaAs interface near the cathode which reduces the barrier height at the interface; 2) across the quasi-neutral bulk region and 3) across the n^{+}/SI-GaAs interface near the anode which increases the barrier height. Of these three voltage drops, that across region (1) is the smallest and hence the barrier height reduction would be very small. The electrons generated in the photoabsorption process in regions (2) and (3) are easily collected while only a fraction of the electrons generated in region (1) are collected due to the strong internal field present in that region. The photogenerated holes in regions (2) and (3)

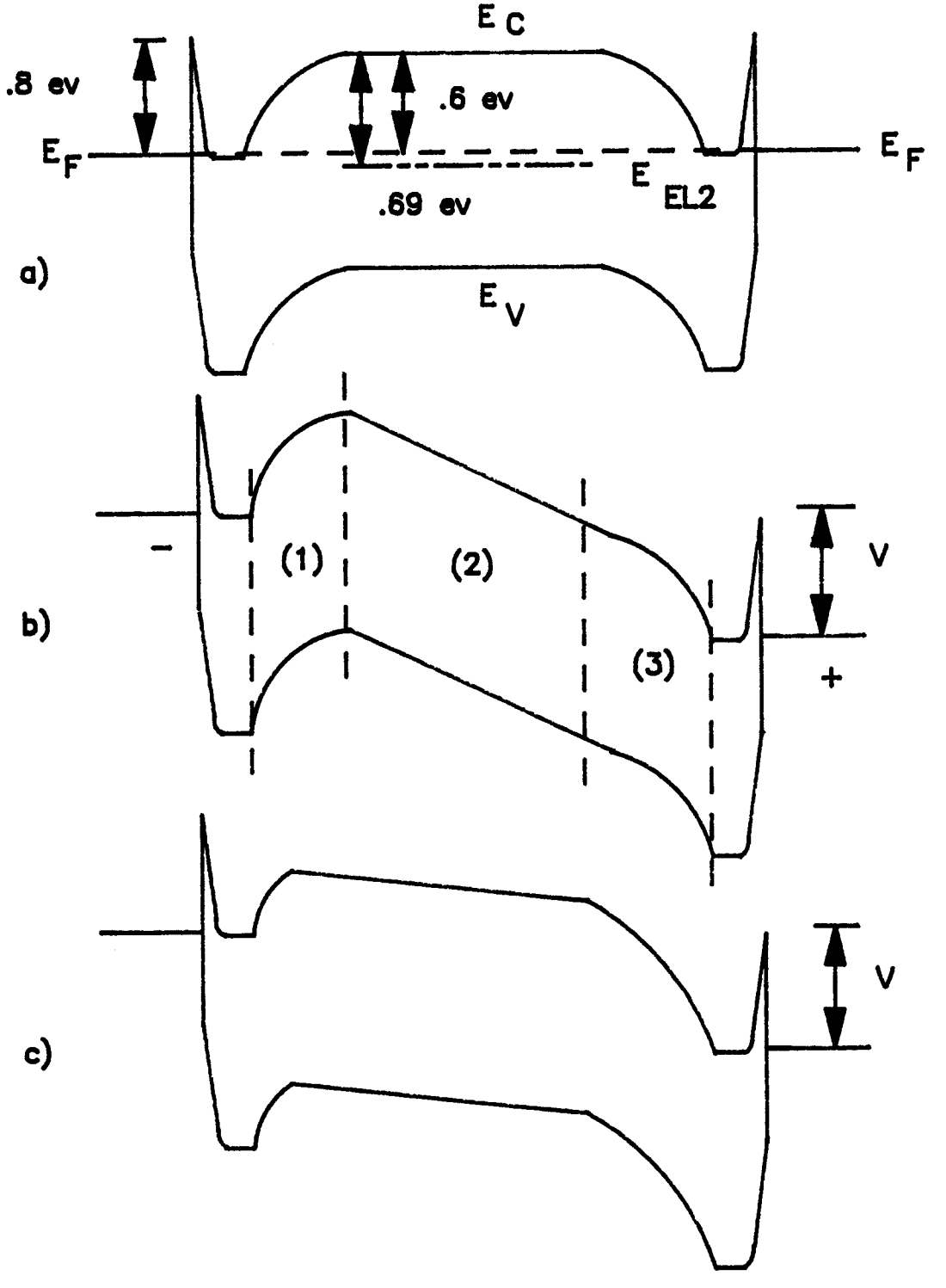

Fig. 5.11 Energy–band diagram of SI–GaAs with ohmic contacts: a) in equilibrium, b) under bias in dark, and c) under bias with illumination.

easily reach the region (1) and (2) boundary, but they can not reach the cathode contact or recombine easily with the electrons in the n^+ region because the hole barrier at the contact is ~ 0.8 eV. A similar effect was predicted in HgCdTe infrared detectors [103]. This barrier would be lowered with high intensities of illumination due to photovoltaic effect. Since most photodetector applications require both sensitive and high speed detectors, the barrier for holes poses a serious limitation as far as speed is concerned. Large photoconductive gains can be observed at low light intensities if electrons can enter region (2) easily to satisfy the charge neutrality in region (2). Very large detectivities were indeed observed in epi-layer GaAs photoconductive detectors at low light intensities and at small frequencies [26-29]. The gains of the ohmic contact detectors were measured by Yang [62] and Schumm [61] to be 2-100.

The hole trapping near the cathode contact is independent of the detector dimensions and hence explains the observed non-correlation of fall time with either hole transit time or RC-limited decay time. The holes would eventually recombine in the bulk due to excess carrier lifetime. Evidence of trapping could also be seen in the detectors tested by the OIG pulse. These trapping effects go away at high intensities of illumination as can be seen from Fig. 5.5 which shows the pulse response to the intense dye laser.

A small tail is observed in the pulse response of the interdigitated MSM photodetector response. This is believed to be caused by traps or the slow moving holes. The tail is shortened with increasing bias. The response drops below the 0% level of the pulse due to inductance effects in the

bias-T. No such dip is seen in the response of the simple MSM gap which is tested without a bias-T.

The predicted response curve for the interdigitated MSM detector is plotted in Fig. 5.12. The predicted risetime and FWHM are 100 ps and 323 ps, respectively when only electron current is considered and 106 ps and 366 ps, respectively when both electron and hole currents are considered. The measured risetime and FWHM are 130 ps and 320 ps, respectively. The measured risetime is the overall risetime. It includes the combined effects of the finite risetime of the input optical pulse, the risetime of the sampling scope, the risetime of the bias-T and the risetime of the detector itself. This is why the measured risetime is slightly higher than the predicted risetime. The measured and predicted FWHMs agree well. The falltimes are difficult to compare because of the reflections due to packaging. The hole current is significant only at high electric fields where hole drift velocitiy approaches saturation velocity. The hole current can be neglected at low electric fields.

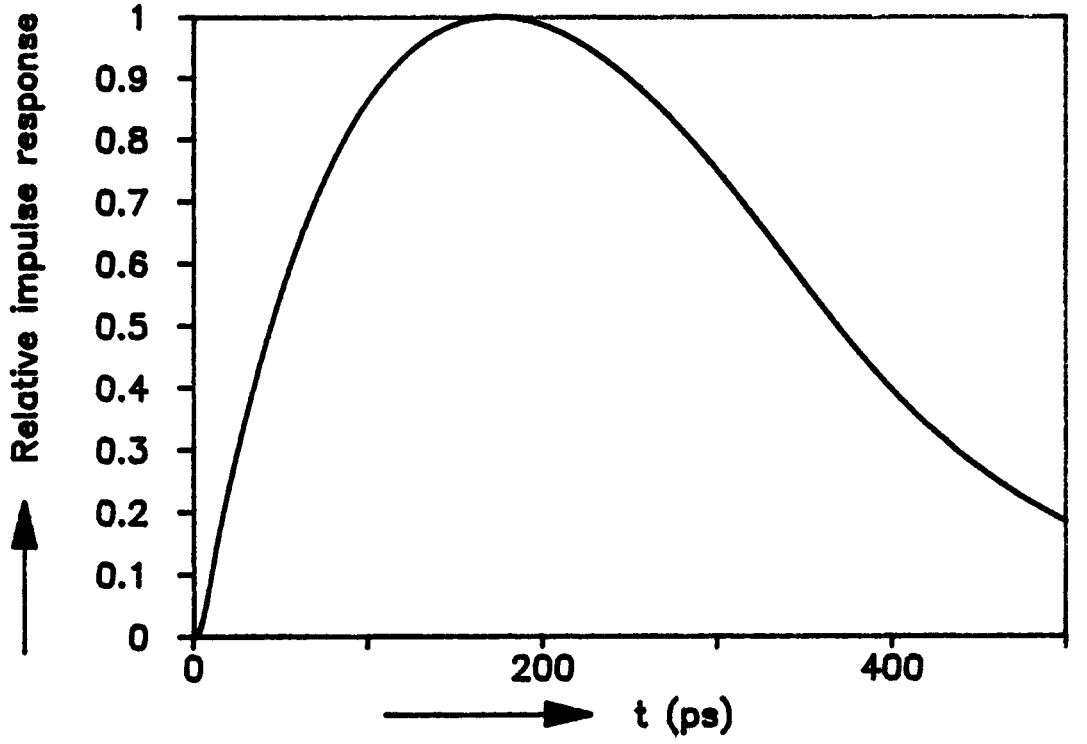

a)

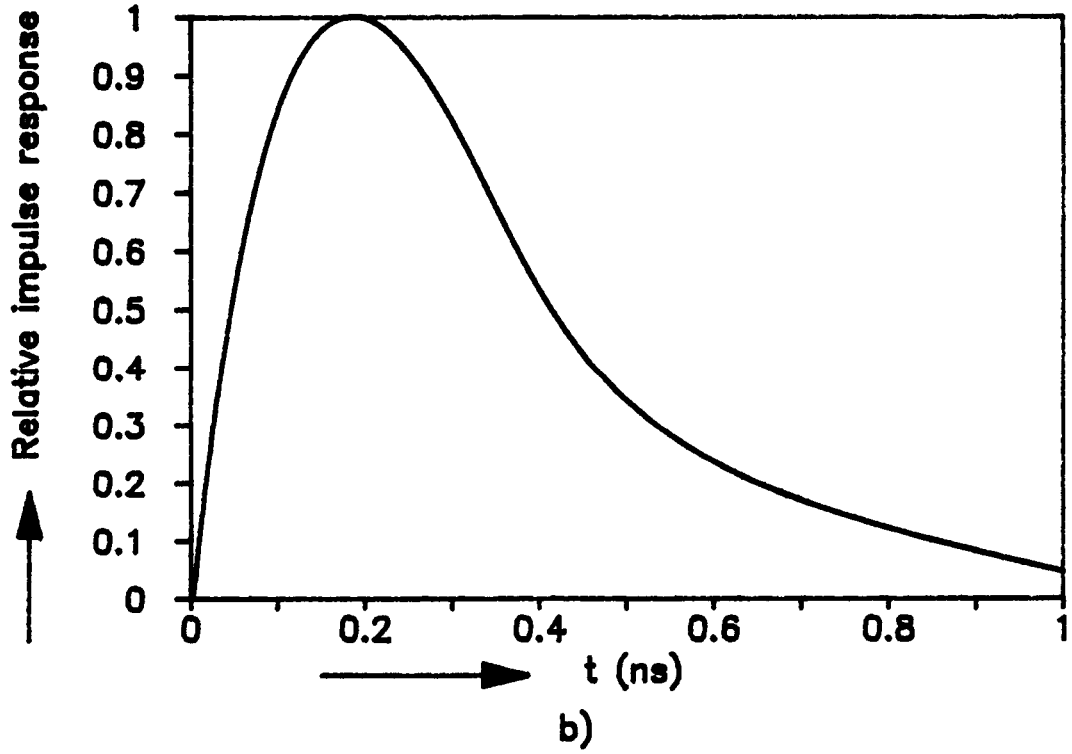

b)

Fig. 5.12 Predicted impulse response of the MSM interdigital photodetector. a) Impulse response of electrons. b) Impulse response of electrons and holes

6. CONCLUSIONS AND RECOMMENDATIONS FOR FUTURE WORK

6.1 Summary and conclusions

In this thesis the time response characteristics of ohmic and Schottky contact photodetectors fabricated on SI-GaAs material have been discussed. In chapter 2 the theory of photodetectors is discussed and the parameters that describe a photodetector are given. The literature with respect to GaAs photodetectors is reviewed.

In chapter 3, a computer-aided-design compatible model of the interdigitated structure is presented which takes into account the discontinuities in the pattern. The model is shown to be valid well into the GHz range as long as the quasistatic assumption is valid. The series resistance due to conductor losses for moderate finger lengths and metal thickness is small when compared to the contact resistance and spreading resistance of the interdigitated contacts. The parasitics influence the time response of the detector, so if the parasitic elements are known, the time response could be modeled.

In chapter 4 an impulse response simulation of SI-GaAs MSM photodetectors is carried out. The finite difference numerical technique is employed. The potential and field distribution inside the detector are calculated. Diffusion and recombination effects are included. Dynamic simulation is performed after applying an ideal optical impulse. The influence of the parasitic elements on the time response of the detector is shown. The simulated intrinsic current acts as the current source for the detector equivalent circuit and the output voltage across the load resistor is computed. The simulated results are compared with published analytical and experimental results. The model helps in the

understanding of the detector response including the 2-D effects and should be useful in the design of SI-GaAs MSM photodetectors.

In chapter 5, the fabrication process of the ohmic and Schottky detectors and the packaging techniques utilized are described. The I-V and pulse measurements made on the fabricated detectors are shown and discussed. The long fall time observed for the ohmic contact detector is a problem in high speed applications and requires equalization. Schottky contact detectors have a fall time limited by the transit time or the parasitic elements of the detector circuit. The MSM detectors could be used in high speed applications.

The parasitics associated with the packaging depend on the type of packaging employed. Even if the same package is used to compare different detectors, there could still be variations in the parasitic element values. The parasitics modeled in chapter 3 are intrinsic to the detector's interdigitated structure and do not depend on the type of packaging used. The particle current modeled in chapter 4 also does not depend on the parasitics. However, the output voltage across the load resistor is influenced by the particle current, the detector's intrinsic parasitics and the parasitics associated with the packaging. For this reason, it is difficult to compare the predicted results directly against the measured results. However, the model could be fitted to the experimental results by varying the parasitic elements associated with the packaging.

In conclusion, the equivalent circuit elements of the IDS are modeled and are included in the impulse response simulation of SI-GaAs MSM photodetectors. The SI-GaAs MSM photodetectors are promising for high speed applications whereas SI-GaAs ohmic contact detectors require equaliztion

for high speed applications. The dark current of both MSM and ohmic contact detectors is in the nanoamperes range at operating voltages. Both detectors can be easily integrated with a GaAs MESFET amplifier.

6.2 Suggestions for future work

The simulation of ohmic contact detectors is quite involved and must include the effects of electron and hole trapping. The voltage drops across various regions of the detector need to be computed. Barrier lowering and space charge injection must also be considered. The simulation of impulse response should include the modeled circuit elements of the IDS. The model could be used to calculate the DC or low frequency gain which can be compared with the experimentally observed values.

The finite difference method is implemented on a uniform grid for calculating the impulse response of MSM photodetector. Implementation of a nonuniform grid would allow a higher density of node points near the conductor corners where the field changes rapidly. An exponentially decreasing grid spacing as a function of depth would make the grid spacing to be proportional to the carrier density at $t=o^{+}$. Simulation depth could also be increased beyond 2.5 μm to account for more of the photogenerated carriers.

One possible investigation is the the study of gain in MSM photodetectors which is not well understood. The various theories proposed by some were ruled out by others. Large scale testing might be needed to find out what is causing the gain.

Another area of possible investigation is to study the dark current and noise properties of the MSM and ohmic contact photodetectors made on SI-GaAs. Especially the

mechanism causing the increase in dark current with aging needs to be understood before it can be eliminated. The noise properties help determine the NEP and the specific detectivity of these detectors.

Finally detectors with both p- and n-ohmic contacts could be studied. These are expected to behave like p-i-n photodiode and will have short response times. These can also be integrated with MESFETs if the MESFET processing includes a p-well implant step.

All of these studies depend critically on the package parasitics. Another whole study of packaging effects on overall detector response is necessary but will be very difficult to quantify and achieve definitive results.

BIBLIOGRAPHY

[1] D.H. Auston, "Impulse Response of Photoconductors in Transmission Lines," IEEE J. Quantum Electron., vol. 19, pp. 639-648, Apri 1983.

[2] R.A. Lawton and A. Scavannec, "Photoconductive Detector of Fast Transition Optical Waveforms," Electron. Lett., vol. 11, pp. 74-75, February 1975.

[3] C.Y. Chen et al., "Bias-free Selectively Doped $Al_xGa_{1-x}As$-GaAs Picosecond Photodetectors," Appl. Phys. Lett., vol. 41, pp. 282-284, August 1982.

[4] C.Y. Chen et al., "New Minority Hole Sinked Photoconductive Detector," Appl. Phys. Lett., vol. 43, pp. 1115-1117, December 1983.

[5] F.H. Boudebous et al., "A Comparison of Interdigital and Straight Structures for a Photoconductive Detector," IEEE Trans. Electron Dev., vol. 32, pp. 836-837, April 1985.

[6] S.M. Sze, Physics of Semiconductor Devices, Wiley, N.Y. (1981).

[7] R.H. Bube, Photoconductivity of Solids, Wiley, N.Y. (1960).

[8] A. Rose, Concepts in Photoconductivity and Allied Problems, Wiley-Interscience, N.Y. (1963).

[9] H. Beneking, "Gain and Bandwidth of Fast Near-Infrared Photodetectors: A Comparison of Diodes, Phototransis-Phototransistors, and Photoconductive Devices," IEEE Trans. on Electron Dev., vol. 29, pp. 1420-1431, September 1982.

[10] S.J. Wojtczuk et al., "Comparative Study of Easily Integrable Photodetectors," J. Lightwave Technol., vol. 5, pp. 1365-1370, October 1987.

[11] J.E. Bowers and C.A. Burrus, "Ultrawide-Band Long-Wavelength p-i-n Photodetectors," J. Lightwave Technol., vol. 5, pp. 1339-1350, October 1987.

[12] S. Miura et al., "A Monolithically Integrated AlGaAs/GaAs p-i-n/FET photoreceiver by MOCVD," IEEE Electron Device Lett., vol. 4, pp. 375-376, October 1983.

[13] B.L Kasper et al., "An APD/FET Optical Receiver Operating at 8 Gbit/s," J. Lightwave Technol., vol. 5,

pp. 344-347, March 1987.

[14] S.Y. Wang and D.M. Bloom, "100 GHz Bandwidth Planar GaAs Schottky Photodiode," Electron. Lett., vol. 19, pp. 554-555, July 1983.

[15] D.G. Parker et al., "110 GHz High-Efficiency Photodiodes Fabricated from Indium Tin Oxide/GaAs," Electron. Lett., vol. 23, pp. 527-528, May 1987.

[16] Z. Rav-Noy et al., "High-Speed Schottky Photodiode on Semi-Insulating GaAs," Electron. Lett., vol. 19, pp. 753-754, September 1983.

[17] C.Y. Chen et al., "An Ultrahigh Speed Modulated Barrier Photodiode Made on P-Type Gallium Arsenide Substrates," IEEE Electron Device Lett., vol. 2, pp. 290-292, November 1981.

[18] Y.M. Pang et al., "1.5 GHz Operation of an $Al_xGa_{1-x}As$/GaAs Modulation-Doped Photoconductive Detector," Electron. Lett., vol. 19, pp. 716-717, Sep. 1983.

[19] C. Baack et al., "GaAs M.E.S.F.E.T.: A High Speed Optical Detector, Electron. Lett., vol., 13, pp. 193, March 1987.

[20] W.D. Edwards, "Two and Three Terminal Gallium Arsenide FET Optical Detectors," IEEE Electron Device Lett., vol. 1, pp. 149-150, August 1980.

[21] J.C. Gammel, "Short Transit Time Photoconductive Detectors for High Speed Optical Communication," Ph.D. Thesis, Cornell University, 1980.

[22] R.B. Darling, "Transit-Time Photoconductivity in High-Field FET Channels," IEEE Trans. Electron Dev., vol. 34, pp. 433-443, February 1987.

[23] R.B. Darling, "Optical Gain and Large-Signal Characteristics of Illuminated GaAs MESFET's," IEEE J. Quantum Electron., vol. 23, pp. 1160-1171, July 1987.

[24] S.R.Forrest, "The Sensitivity of Photoconductive Receivers for Long-Wavelength Optical Communications," J. Lightwve Technol., vol. LT-3, pp. 347-360, April 1985.

[25] S.R. Forrest, "Photoconductor Receiver Sensitivity," IEEE Electron Device Lett. vol. 5, pp. 536-539, December 1984.

[26] J.P. Vilcot et al., "Temperature Effects on High-Gain

photoconductive Detectors," Electron. Lett., vol. 20, pp. 86-87, January 1984.

[27] N. Matsuo et al., "Mechanism of High Gain in GaAs Photoconductive Detectors under Low Excitation," Japanese J. Appl. Phys., vol. 23, pp. L299-L301, May 1984.

[28] J.P. Vilcot et al., "Noise and Dynamical Gain Studies of GaAs Photoconductive Detectors," Electron. Lett., vol. 20, pp. 274-275, March 1984.

[29] M. Constant et al., "Detectivity of High-Gain Photoconductive Detectors," Electron. Lett., vol. 24, pp. 1019-1021, August 1988.

[30] S.J. Wojtczuk and J.M. Ballantyne, "Impedance Properties and Broad-Band Operation of GaAs Photoconductive Detectors," J. Lightwave Technol., vol. 5, pp. 320-324, March 1987.

[31] C.J. Wei et al., "A study on the Photoresponses in GaAs n-channel Optical Detectors," IEEE Trans. Electron Devices, vol. 29, no. 9, pp. 1442-1448, September 1982.

[32] R.B.Darling, "Analysis of Microwave Characteristics of Photoconductive IC Structures," J. Lightwave Technol., vol. 5, no. 3, pp. 325-339, March 1987.

[33] R.B. Darling et al., "Epitaxial n+ Layer GaAs Mesa-Finger Interdigital Surface Photodetectyors," IEEE Electron Device Lett., vol. 10, pp. 461-463, October 1989.

[34] D.K.W. Lam et al., "Surface-Depleted Photoconductors," IEEE Trans. Electron Dev., vol. 34, pp. 1057-1059, May 1987.

[35] D.K.W. Lam et al., "Monolithic Integration of GaAs Photoconductors With a Field-Effect Transistor," Electron. Lett., vol. 22, pp. 753-755, July 1986.

[36] D. Decoster et al., "Planar Monolithic Integration of a GaAs Photoconductor and a GaAs Field-Effect Transistor," Electron. Lett., vol. 22, pp. 193-195, February 1986.

[37] N.G. Paulter et al., "Fabrication of High Speed GaAs Photoconductive Pulse Generators and Sampling Gates by Ion Implantation," IEEE Trans. Electron Devices, vol. 35, pp. 2343-2348, December 1988.

[38] A.M. Johnson et al., "Picosecond OMVPE GaAs/SiO_2

Photoconductive Devices and Applications in Materials Characterization," IEEE J. Quantum Electron., vol. 23, pp. 1180-1184, July 1987.

[39] W. Roth et al., "Fast Photoconductive GaAs Detectors Made by Laser Stimulated MOCVD," Electron Lett., vol. 19., pp. 142-143, February 1983.

[40] C.Y. Chen et al., "High-Sensitivity $Ga_{0.47}In_{0.53}As$ Photoconductive Detectors Prepared by Vapor Phase Epitaxy," Appl. Phys. Lett., vol. 44, pp. 1142-1144, June 1984.

[41] C.Y. Chen et al., "Interdigitated $Al_{0.48}In_{0.52}As$/ $Ga_{0.47}In_{0.53}As$ Photoconductive Detectors," Appl. Phys. Lett., vol. 44, pp. 99-101, January 1984.

[42] C.J Wei et al., "Symmetrical Mott Marrier as a fast Photodetector," Electron Lett., vol. 17, pp. 688-671, September 1981.

[43] W. Roth et al., "The DSI Diode- A Fast Large-Area Optoelectronic Detector," IEEE Trans. Electron Dev., vol. 32, pp. 1034-1036, June 1985.

[44] M. Ito and O. Wada, "Low Dark Current GaAs Meatal-Semiconductor-Metal (MSM) Photodiodes Using WSi_x Contacts," IEEE J. Quantum Electron., vol. 22, no. 7, pp. 1073-1077, July 1986.

[45] B.J. Van Zeghbroeck et al., "105-GHz Bandwidth Metal-Semiconductor-Metal Photodiode," IEEE Electron Device Lett., vol. 9, pp. 527-529, October 1988.

[46] B.J. Van Zeghbroeck, "Analysis of Picosecond and Subpicosecond MSM Photodiodes with Very Low Bias Voltage," IEEE Trans. Electron Dev., vol. 35, pp. 2433-2433, December 1988.

[47] W.C. Koscielniak et al., "Analysis of a GaAs Metal-Semiconductor-Metal (MSM) Photodetector with 0.1-um Finger Spacing," IEEE Electron Device Lett., vol. 10, no. 5, pp. 209-211, May 1989.

[48] W.C. Koscielniak et al., "Dynamic Behavior of Photo-carriers in a GaAs Metal-Semiconductor-Metal Photo-detector with Sub-Half Micron Electrode Pattern," Appl. Phys. Lett., vol. 54, pp. 567-569, Feb. 1989.

[49] O. Wada et al., "Noise Characteristics of GaAs Metal-Semiconductor-Metal Photodiodes," Electron. Lett., vol. 24, pp. 1574-1575, December 1988.

[50] H. Schumacher et al., "A Low Dark Current, Large Bandwidth Mott-Barrier Photodetector Fabricated by Quasi-Ternary Growth of GaAs," IEEE Electron Device Lett., vol. 7, pp. 26-27, January 1986.

[51] M. Ito et al., "Monolithic Integration of a Metal-Semiconductor-Metal Photodiode and a GaAs Preamplifier," IEEE Electron Device Lett., vol. 5, pp. 531-532, December 1984.

[52] M. Ito et al., "High-Speed Monolithically Integrated GaAs Photoreceiver Using Metal-Semiconductor-Metal Photodiode," Appl. Phys. Lett., vol. 47, pp. 1129-1131, December 1985.

[53] D.L. Rogers, "Monolithic Integration of a 3-GHz Detector/Preamplifier Using a Refractory-Gate, Ion-Implanted MESFET process," IEEE Electron Device Lett., vol. 7, pp. 600-602, November 1986.

[54] C.S. Harder et al., "5.2-GHz Bandwidth Monolithic GaAs Optoelectronic Receiver," IEEE Electron Device Lett. vol. 9, pp. 171-173, April 1988.

[55] T. Sugeta et al., "Metal-Semiconductor-Metal Photodetector for High Speed Optoelectronic Circuits," Japanese J. Appl. Phys., vol. 19, pp. 459-464, 1980.

[56] C.W. Slayman and L. Figueroa, "Frequency and Pulse Response of a Novel High Speed Interdigital Surface Photodetector (IDPC)," IEEE Electron Device Lett., vol. 2, pp. 112-114, May 1981.

[57] W.S. Lee et al., "Monolithic GaAs Photoreceiver for High Speed Signal Processing Applications," Electron. Lett., vol. 22, pp.147-148, January 1986.

[58] D.J. Jackson and D.L. Persechini, "Large Area High Speed PIN Detectors in GaAs," Electron Lett., vol. 22, pp. 202-203, February 1986.

[59] D.J. Jackson and D.L. Persechini, "Monolithically Integrated High Speed Photodetectors," SPIE, vol. 716, pp. 104-108, 1987.

[60] G. Schumm and T.K. Plant, "Undoped and Chromium-Doped Semi-Insulating GaAs Photoconductive Detectors," Solid-State Electronics, vol. 30, pp. 109-112, 1987.

[61] G. Schumm, "A Study of The Photoresponse of Semi-Insulating Gallium Arsenide," M.S. Thesis, Oregon State University, 1985.

[62] H.C. Yang, "Characteristics of SI GaAs Photoconductive Detectors Under Steady State Illumination," M.S. Thesis, Oregon State University, 1986.

[63] W.C. Koscielniak et al., "Performance of a Near-Infrared GaAs Metal-Semiconductor-Metal (MSM) Photodetector with Islands," IEEE Electron Device Lett. vol. 9, pp. 485-487, September 1988.

[64] K. Nakajima et al. "Properties and Design Theory of Ultrafast GaAs Metal-Semiconductor-Metal Photodetector with Symmetrical Schottky Contacts," IEEE Trans. Electron Dev. vol. 37, pp. 31-35, January 1990.

[65] R.B Hammond et al., "InP:Fe Photoconductors as Photodetectors," IEEE Trans. Electron Dev. vol. 30, pp. 412-415, April 1983.

[66] K. Wilson, "Other Circuit Elements for MMICs," GEC Journal of Research, vol. 4, pp. 126-133, 1986.

[67] Z.Y. Cheng and C.S. Tsai, "A Novel Integrated Acousto-optic Frequency Shifter," J. Lightwave Technol. vol. 7, pp. 1575-1580, October 1989.

[68] P.M. Asbeck, "Heterojunction Bipolar Transistors for Microwave and Millimeter-Wave Integrated Circuits," IEEE Trans. Electron Dev., vol. 34, pp. 2571-2579, December 1987.

[69] G.L. Matthaei, "Interdigital Band-Pass Filters", IRE Trans. Microwave Theory Tech., vol. MTT-10, pp. 479-491, Nov. 1962.

[70] C.L. Ren, "On the Analysis of General Parallel Coupled TEM Structures Including Nonadjacent Couplings", IEEE Trans. Microwave Theory Tech., vol. MTT-17, pp. 242-249, May 1969.

[71] D.F. Williams and S.E. Schwarz, "Design and Performance of Coplanar Waveguide Bandpass Filters", IEEE Trans. Microwave Theory Tech, vol. MTT-31, pp. 558-566, July 1983.

[72] W.P. Ou, "Design Equations for an Interdigitated Direc tional Coupler", IEEE Trans. Micowave Theory Tech., vol. MTT-23, pp. 253-255, Feb. 1975.

[73] Y.K. Chin, "Analysis and Applications of Multiple Coupled Line Structures in an Inhomogeneous Medium", Ph.D. Thesis, Oregon State University, 1982.

[74] G.D. Alley, "Interdigital Capacitors and Their Appli-

cation to Lumped-Element Microwave Integrated Circuits", IEEE Trans. Microwave Theory Tech.,vol. MTT-18, pp. 1028-1033, Dec. 1970.

[75] J.L. Hobdell, "Optimization of Interdigital Capacitors", IEEE Trans. Micowave Theory Tech., vol. MTT-27, pp. 788-791, Sept. 1979.

[76] R. Esfandiari et al., "Design of Interdigitated capacitors and Their Application to Gallium Arssenide Monolithic Filters", IEEE Trans. Microwave Theory Tech., vol. MTT-31, pp. 57-64, Jan. 1983.

[77] E. Pettenpaul, et. al., "CAD Models of Lumped Elements on GaAs up to 18 GHz", IEEE Trans. Microwave Theory Tech., vol. MTT-36, pp. 294-304, Feb. 1988.

[78] K.C. Gupta et al, Computer Aided Design of Microwave Circuits, Artech, Dedham, Mass. (1981).

[79] V.K.Tripathi, "Asymmetric Coupled Transmission Lines in an Inhomogeneous Medium," IEEE Trans. Microwave Theory Tech., vol. MTT-23, pp. 734-739, September 1975.

[80] M. Kirschning et al., "Measurement and Computer Aided Modeling of Microstrip Discontinuties by an Improved Resonator Method," IEEE MTT-S International Microwave Symposium Digest, pp. 495-497, 1983.

[81] M. Kirschning and R.H. Jansen, "Accurate, Wide Range Design Equations for the Frequency Dependent Characteristics of Parallel Coupled Microstrip Lines", IEEE Trans. Microwave Theory Tech.,vol. MTT-32, pp. 83-90, January 1984. (Corrections in March 1985, p288).

[82] I.J. Bahl and P. Bhartia, Microwave Solid State Circuit Design, Wiley, N.Y. (1988).

[83] C.M. Snowden, Introduction to Semiconductor Device Modeling, World Scientific Publishing Co., Singapore, (1986).

[84] M. Kurata, Numerical Analysis for Semiconductor Devices, Lexington Books, D.C.Heath and Co., Lexington, USA, (1982).

[85] S. Selberherr, Analysis and Simulation of Semiconductor Devices, Springer-Verlag, Wien-New York, (1984).

[86] R.L. Peterson, "Numerical Study of Currents and Fields

in a photoconductive Detector," IEEE J. Quantum Electron., vol. QE-23, no. 7, pp. 1185-1192, July 1987.

[87] A.E. Iverson and D.L. Smith, "Mathematical Modeling of Photoconductor Transient Response," IEEE Trans, Electron Devices, vol.ED-14, no. 10, pp. 2098-2107, October 1987.

[88] A. Kolodny and I. Kidron, "Two-Dimensional Effects in Intrinsic photoconductive Infrared Detectors," Infrared Physics, vol. 22, pp. 9-22, 1982.

[89] P.F. Lindquist and W.M. Ford, "Semi-Insulating GaAs Substrates," in GaAs FET Principles and Technology, J.Di Lorenzo and D.Khandelwal, Eds., Dedham, MA., Artech (1982).

[90] R.N. Thomas et al., "Status of Device-Qualified GaAs Substrate Technology for GaAs Integrated Circuits," Proc. IEEE, vol. 76, no.7, pp. 778-791, July 1988.

[91] J.F. Wager and A.J. McCamant, "GaAs MESFET Interface Considerations," IEEE Trans. Electron Devices, vol. ED-34, no. 5, pp. 1001-1007, May 1987.

[92] S.P. Yu and W. Tantraporn, "A Computer Simulation Scheme for Various Solid-State Devices," IEEE Trans. Electron Devices, vol. ED-22, no. 8, pp. 515-522, August 1975.

[93] A. Gopinath and H. Atwater, "Simulation of GaAs p-i-n Diodes," IEEE Trans. Electron Devices, vol. 35, no. 4, pp. 414-417, April 1988.

[94] G.M. Martin et al., "Electron Traps in Bulk and Epitaxial GaAs Crystals," Electron. Lett., vol. 13, pp. 191-192, March 1977.

[95] R.E. Kremer et al., "Transient Photoconductivity Measurements in Semi-Insulating GaAs. I. An Analog Approach," J. Appl. Phys., vol.62, no. 6, pp. 2424-2438, 1987.

[96] J. Xu and M. Shur, "Velocity-Field Dependence in GaAs," IEEE Trans. Electron Devices, vol. ED-34, No. 8, pp. 1831-1832, August 1977.

[97] K.H. Hellwege, Ed., Landolt-Bornstein Numerical Data and Functional Relationships in Science and Technology, vol. III, pt. 17a, Physics of Group IV Elements and III-V Compounds, O. Madelung, Ed. New York:

Springer-Verlag, 1987, pp. 319.

[98] D.L. Scharfetter and H.K. Gummel, "Large-Signal Analysis of a Silicon Read Diode Oscillator," IEEE Trans. Electron Devices, vol. ED-16, no. 1, pp. 64-77, January 1977.

[99] W.H. Press et al., Numerical Recipies, Cambridge University Press, Cambridge, 1989.

[100] J.E. Bowers et al., "InGaAs PIN Photodetectors with Modulation Response to Millimeter Wavelengths," Electron. Lett., vol. 21, pp. 812-814, August 1985.

[101] D.H.Lee et al., "A Study of Surface Passivation on GaAs and $In_{0.53}Ga_{0.47}As$ Schottky-Barrier Photodiodes Using SiO_2, Si_3N_4 and Polymide," IEEE Trans. Electron evices, vol. ED-35, pp.1695-1696, October 1988.

[102] M.Shur, GaAs Devices and Circuits, New York, Plenum Press, 1987, pp. 383-387.

[103] Y.J.Shacham-Diamand and I.Kidron, "Contacts and Bulk Effects in Intrinsic Infrared Detectors," Infrared Physics, vol. 21, pp.105-115, 1981.